A NEW STOCHASTIC PORE-SCALE SIMULATION AND MACHINE LEARNING APPROACH TO PREDICTING PERMEABILITY AND TORTUOSITY OF HETEROGENEOUS POROUS MEDIA

By

OLUBUKOLA ADEDOTUN ISHOLA

Bachelor of Science (Honours) in Geophysics
Adekunle Ajasin University
Ondo, Nigeria
2013

Master of Science in Petroleum Geoscience
University College Dublin
Dublin, Republic of Ireland
2018

Submitted to the Faculty of the
Graduate College of the
Oklahoma State University
in partial fulfillment of
the requirements for
the Degree of
DOCTOR OF PHILOSOPHY
May, 2023

A NEW STOCHASTIC PORE-SCALE SIMULATION AND MACHINE LEARNING APPROACH TO PREDICTING PERMEABILITY AND TORTUOSITY OF HETEROGENEOUS POROUS MEDIA

Dissertation Approved:

Dr. Javier Vilcaez

Dissertation Adviser

Dr. Todd Halihan

Dr. Jaiswal Priyank

Dr. Aaron Alexander

ACKNOWLEDGEMENTS

I want to thank Dr. Javier Vilcaez, who is my primary advisor and the chair of my PhD supervisory committee, for his support, motivation, and advice throughout my PhD program. As a PhD candidate, I was able to reach my full potential because to the advice I got from Dr. Vilcaez. It made it possible for me to frequently publish and go to conferences in addition to acquiring the new skills required to be successful in my field in my area of specialty. Also, I would like to express my deep gratitude to members of my PhD committee in Drs. Todd Halihan, Jaiswal Priyank, and Aaron Alexander, for their technical expertise, leadership, and helpful criticism at various stages along the course of my PhD. I also want to thank Dr. Ali Tinni from the University of Oklahoma and Ryan Antle at Baker Hughes for helping me with data gathering and educating me on technologies that were crucial to my research. Notably, I want to appreciate the efforts of Dr. Camelia Knapp for all the opportunities provided to me through recommendation letters that lead to several scholarships and internships.

Importantly, I've been fortunate to get support during my entire doctorate, which I genuinely appreciate. This includes support from the National Science Foundation, the Boone Pickens School of Geology, the AAPG Foundation, the Society of Exploration Geophysicists, the American Geophysical Union, Dr. Homer & Mrs. May Tang, the Society of Petrophysicists and Well Log Analysts, the National Association of Black Geoscientists, the West Texas Geological Society, the Geoscience Foundation of Tulsa, the Oklahoma Geological Foundation, and the Society of Petroleum Engineers, among others.

Special thanks go out to the Boone Pickens School of Geoscience faculty, staff, and colleagues for their support. I also want to express my gratitude to Dr. Vitalii Starchenko at Oak Ridge National Laboratory, who gave me my first chance to work outside of OSU (during an internship) and taught me several technical skills that have helped me improve on my projects. Finally, I want to express how appreciative I am to my parents and siblings for all the assistance I have had throughout my education.

Name: OLUBUKOLA ADEDOTUN ISHOLA

Date of Degree: MAY, 2023

Title of Study: A NEW STOCHASTIC PORE-SCALE SIMULATION AND MACHINE LEARNING APPROACH TO PREDICTING PERMEABILITY AND TORTUOSITY OF HETEROGENEOUS POROUS MEDIA

Major Field: GEOLOGY

Abstract: A new 3D stochastic pore-scale simulation approach was introduced in this study to investigate how stochastic pore connectivity impacts the permeability and hydraulic tortuosity of heterogeneous porous media. Multiple three-dimensional pore microstructures with the same porosity, pore size distribution, and number of pores were created to examine the role that pore connectivity plays in permeability and hydraulic tortuosity of rocks. According to the findings of this study, stochastic pore connectivity has a sizeable influence on permeability but a comparatively insignificant influence on hydraulic tortuosity. In addition, there is a negative correlation between the amount of heterogeneity and the predictability of permeability based on hydraulic tortuosity. The study used four carbonate and five siliciclastic rock cores to validate the findings, and the predicted permeability was generally closer to the measured permeability than five popular empirical model equations. In addition, machine learning was utilized to optimize the workflow, which resulted in a reduction in the necessary number of pore-scale simulations by a factor of 157 and the reproduction of pore-scale permeability estimates was with a mean absolute percentage error of 10%. The conventional use of SEM and micro-CT technologies in generating pore microstructures was augmented through the addition of MICP data to capture high-resolution information in rocks at a representative scale. Pore microstructures generated through the approach were validated via a comparable permeability of the pore microstructure with the measured permeability of the rock sample modelled. The findings of this study has a broad range of geoscience applications including, petroleum exploration and production, carbon storage, environmental protection, and groundwater exploration.

TABLE OF CONTENTS

LIST OF TABLES

Table Page

LIST OF FIGURES

Figure Page

CHAPTER I

INTRODUCTION

1.1 Background and Summary of Problem

Carbonate sedimentary rocks are notoriously difficult to predict when it comes to their fluid-flow characteristics (Hulea & Nicholls, 2012; Sun et al., 2017; Westphal et al., 2005). This is a product of intense diagenetic changes in carbonate rocks throughout their formation and history resulting in pore sizes and flow properties varying over orders of magnitude (Knackstedt et al., 2006; Regnet et al., 2019; Westphal et al., 2005). In general, these measured properties rock properties are relied on to develop models and workflow for making predictions of fluid-flow. This is because the pore microstructural configuration of rocks imposes the flow path for fluid passage which defines key properties like permeability and hydraulic tortuosity (Regnet et al., 2019; Sun et al., 2017; Y. Wu et al., 2018). Permeability can be defined as the ease at which fluid moves through a rock. In numerous cases, an estimation of permeability is derived from deterministic empirical correlations between measurable pore microstructural features to permeability (Civan, 2002; Westphal et al., 2005) or a more complex relationships between a combination of pore microstructural features to estimates permeability, like the Carman-Kozeny equation (Bernabé et al., 2010; Starnoni et al., 2017). It is well known that permeability values derived from systematic correlations and empirical model equations

have the potential to reliably anticipate fluid flow in siliciclastic rocks; however, these is rarely true for prediction of flow in carbonate sedimentary rocks. When compared to siliciclastic rocks, carbonate sedimentary rocks have a high degree of heterogeneity and a complex pore microstructure (Devarapalli et al., 2017; Hulea & Nicholls, 2012; Westphal et al., 2005). The validity of the flow predictions derived based on deterministic correlations and empirical models is called into question because of this. For example, it has been shown that the range of permeability can be up to five orders of magnitude different when porosity is the main factor used to predict permeability (Comisky et al., 2007; Hulea & Nicholls, 2012).

Tortuosity is another essential petrophysical property of porous media. Tortuosity can be defined as the degree of twist in the flow path present in a rock. Like permeability, tortuosity is commonly modeled using deterministic model equations that employ porosity as the controlling pore microstructure factor(Ghanbarian et al., 2013; Lala, 2020). Since permeability and hydraulic tortuosity are generally correlated (Cai et al., 2019), using porosity might also lead to inaccurate estimates of hydraulic tortuosity, which would have negative effects on simulations of solute and reactive transport. The challenge of using the measured characteristics of rocks to predict fluid flow stems from the fact that even though there could be some association between these two sets of properties, it doesn't necessarily imply a cause-and-effect relationship. It is well known that a combination of pore connectivity and pore-throat size distribution is largely responsible for flow properties in rocks (Bernabé et al., 2010; Hulea & Nicholls, 2012). Unfortunately, these two pore microstructural parameters cannot be measured directly in rocks at representative scale that is sufficient to characterize heterogenous rocks which includes most carbonate

rocks(Bazaikin et al., 2017; Blunt et al., 2013; Mees et al., 2003; Saxena et al., 2019; Saxena et al., 2018; Xiong et al., 2016). Pore connectivity in carbonate rocks is typically complex and this is attributed to the heterogeneity resulting from diagenesis and substantial facies variations (Choquette & Pray, 1970). The impact of the overall pore microstructural features of a rock on fluid flow is not fully understood, especially in carbonate rocks (Bijeljic et al., 2013; Zhang & Cai, 2021). Developing this understanding is important to make better improved inferences that depend on transport properties of rock materials.

1.2 Previous Work

Numerous studies have been conducted to establish predictive methods of flow and transport properties for rocks. These methods can be broadly categorized into empirical correlation, numerical simulation, and data-driven methods.

a. Empirical correlation methods: This category comprise of all methods that uses statistical approaches to find possible relationship between measurable pore microstructural feature(s) in rocks and their transport properties. Measurable properties can be reliably obtained from imaging data such as thin section, Scanning Electron Microscope (SEM), Focused Ion Beam Scanning Electron Microscope (FIB-SEM), and X-ray microtomography (micro-CT) image of rocks. This approach was used by (Peng et al., 2016) and (Coskun & Wardlaw, 1993) to predict permeability in rocks where important pore microstructures like pore-throats and porosity are obtained from thin sections and SEM images of siliciclastics (Coskun & Wardlaw, 1993) and carbonate rocks

(Peng et al., 2016). It is evident from comparing the result presented in both studies that empirical correlations tend to work very well with siliciclastics. While we can say these methods are predictive for siliciclastics, it can only be confidently said to be correlative for carbonate rocks because of the low predictive power of the model.

Other non-imaging methods such as Mercury Injection Capillary Pressure (MICP) and Nuclear Magnetic Resonance (NMR) T2 measurements have been more traditionally employed to generate empirical correlations to estimate permeability. The estimation of permeability through MICP analysis is typically reliant on an empirical correlation established between the critical ore representative pore-throat size (and porosity), at which mercury infiltration is considered to connect the entire pore system of a rock sample, and the sample's permeability. This includes Winland (S. Kolodzie, 1980), Swanson (B. Swanson, 1981), Wells-Amaefule (Wells & Amaefule, 1985), Kamath (Jairam Kamath, 1992), and Dastidar models (Rahul Dastidar, Carl H Sondergeld, et al., 2007) in Eqs. (1.1) - (1.5) respectively.

$$k_{\text{Winland}} = 49.4 * R_{35}^{1.7} * \emptyset^{1.47} \quad (1.1)$$

$$k_{\text{Swanson-brine}} = 355 * \left[\frac{s_b}{P_C}\right]_A^{2.005} \quad (1.2)$$

$$k_{\text{Wells-Amaefule}} = 30.5 * \left[\frac{s_b}{P_C}\right]_A^{1.56} \quad (1.3)$$

$$k_{\text{Kamath}} = 347 * \left[\frac{s_b}{P_C}\right]_A^{1.60} \quad (1.4)$$

$$k_{\text{Dastidar}} = 4073 * R_{wgm}^{1.64} * \emptyset^{3.06} \quad (1.5)$$

where s_b is the percent bulk volume occupied by mercury, P_C is the mercury capillary pressure (Psia), A is the maximum amplitude, R_{35} is 35% mercury saturation of pore volume, $\emptyset$ is porosity (fraction), and R_{wgm} is the geometric mean of pore sizes.

On the other hand, NMR employs the uses a combination of porosity along with T_2 distribution and the ratio BVI (bulk volume of irreducible fluid) to BVM (bulk volume of movable fluid) in predicting permeability (Westphal et al., 2005). The two prominent equations for deducing permeability from NMR data are the Timur-Coates (TC) equation (Coates & Denoo, 1981; Timur, 1968) and the Schlumberger-Doll-Research (SDR) equation (Kenyon et al., 1988) given by Eq. 1.6 and 1.7 respectively.

$$k_{TC} = a \times \left(\frac{\emptyset NMR}{100}\right)^4 \times \left(\frac{BVM}{BVI}\right)^2 \tag{1.6}$$

$$k_{SDR} = b \times \left(\frac{\emptyset NMR}{100}\right)^4 \times \left(T_{2,\log mean}\right)^2 \tag{1.7}$$

where $\emptyset NMR$ is porosity from NMR measurement in [pu], BVM is bulk volume movable in [pu], BVI is bulk volume irreducible in [pu], $T_{2,\log mean}$ is logarithmic mean of T_2 distribution in [ms], a is empirical proportionality constant in [ms^2], and b is empirical proportionality constant in [m^2/ms^2].

While empirical correlations derived from NMR T2 measurements have been proven to be accurate in predicting the permeability of sandstone rocks, these correlations are known to be very inaccurate in predicting the permeability of carbonate rocks (Westphal et al., 2005). Another popular approach that falls within empirical correlation methods is the direct measurement from routine core analysis where porosity and permeability of rocks

could be measured and used to establish poroperm measurements (Bhatti et al., 2020; Ghadami et al., 2015). Like other empirical models, this approach doesn't usually work well with heterogeneous rocks. The main reason they all work well with siliciclastics is because they are usually uniform in nature while they tend to fail in carbonates because they are significantly complex due to heterogeneity.

b. Direct pore-scale simulation methods: One way to consider heterogeneity that is present is porous media is through direct pore -scale simulations. The ability of direct pore-scale simulations of flow and transport properties of porous media depends on the fidelity of the approach used acquire the pore microstructural feature of the rocks. SEM, FIB-SEM, and micro-CT technologies are the most tools used in capturing pore microstructural data of rocks (Blunt et al., 2013; Xiong et al., 2016). This could be done by directly simulating fluid flow through the resultant data since they are images that represent pore microstructural configuration of rocks. More advanced approaches use statistical approaches in lieu of direct images. For instance, 2D images from thin section images has been successfully used constructing 3D representation of rock data (Hajizadeh et al., 2011; Okabe & Blunt, 2004) using two-point and multipoint statistics, which does a good job at producing realistic pore microstructures of homogeneous rocks, mainly siliciclastics. The heterogeneity of carbonate rocks often results in unreliable reconstructions of 3D pore microstructures from 2D images. This is due to the unpredictability along the third dimension of the microstructure that is being reconstructed. 3D reconstructions of heterogeneous porous media can be achieved with greater reliability using 3D image data, such as micro-CT and FIB-SEM images. This involves extracting simplified pore

networks with geometries such as spheres and tubes (Blunt et al., 2013; Xiong et al., 2016). Notwithstanding the advancements made in porous media modeling through 3D imaging technologies, it still faces challenges in simulating the flow properties of highly heterogeneous porous media. This is because obtaining the pore microstructural information of a representative rock volume is crucial for accurate simulation (Bernabé et al., 2010; Civan, 2002; Dasgupta & Mukherjee, 2020; Zhao et al., 2022) , however, it is a daunting task to acquire representative 3D images of heterogeneous rock with sufficient resolution to identify the key features that control fluid flow in pore-throats and pore connectivity. This difficulty arises from the inverse relationship between the resolution of imaging technologies and the size of samples that can be analyzed (Bazaikin et al., 2017; Blunt et al., 2013; Devarapalli et al., 2017; Mees et al., 2003; Saxena et al., 2019; Saxena et al., 2018; Wang & Miller, 2020; Xiong et al., 2016). Furthermore, FIB-SEM, the most effective imaging technique at the required scale, is a costly and destructive procedure (Blunt et al., 2013; Xiong et al., 2016). Conversely, the degree of homogeneity in siliciclastic rocks implies that smaller rock sizes can be imaged (Adeleye & Akanji, 2017; Bear, 1972), which allows for higher resolution 3D images that generally facilitate the direct acquisition of pore-throat and pore connectivity information from siliciclastic rocks. Hence, these approaches are generally not suitable for the modelling and simulation of transport properties through carbonate sedimentary rocks.

c. Data-driven methods: With the continuous growth of computational power and increasing efficiency of computational methods, the use of machine learning methods to predict flow properties of subsurface porous media is becoming increasingly popular

(Tahmasebi et al., 2020). The popular approach in this area largely depends on variation of convolutional neural network (CNN) methodologies to predict flow properties of pore microstructures. While there is a lot of studies published in this area, a short review on three recent papers is used to explain recent advances. To demonstrate the efficacy of CNN on the prediction of flow properties, Graczyk and Matyka (2020) designed a two-dimensional experiment where overlapping quad solids were used to generate controllable pore microstructures and used 2D CNN to predict their porosity, permeability, and tortuosity within 6% of the true value (Graczyk & Matyka, 2020). A novel 3D CNN model was developed by Elmorsy et al. (2022) for end-to-end prediction of permeability. Elmorsy and others were able to extract 3D subvolumes of from micro-CT scans of rocks compared the performance of the 3D CNN model on the 3D data with direct numerical simulations with OpenFoam® where the simulated permeability of the ranging from 0 to 20,000 mD. The developed novel 3D CNN had an R^2 of 0.95 (Elmorsy et al., 2022). In another approach, Zhang and others (2022) used an autoencoder based convolutional neural network (AE-CNN) to improve accuracy of 2D permeability prediction obtained from traditional CNN workflows with R^2 improving from 0.869 to 0.896 when compared with traditional approaches (H. Zhang et al., 2022). The introduced AE-CNN was used to resolve possible challenges associated with poor image resolution. It is not worthy that poor resolution images in the paper by Zhang and other implies that the images are blurry and does not relate to the degree of detail obtained from data acquisition. The autoencoder portion of the AE-CNN was used to create a model that helps learn the relationship between low resolution and high-resolution images, hence, including it as a backbone when making prediction of permeability from low resolution images better replicates what

would have been obtained from higher resolution images than using a conventional CNN model (H. Zhang et al., 2022). While data driven methods are state of the art approaches which look for hidden relationships between rock data and its flow properties, it inherits the pitfalls associated with the data acquisition method itself. As established earlier, acquisition of image data of carbonate rocks is lacking in terms of good resolution and/or not representative for pore microstructural properties they ought to capture (Bazaikin et al., 2017; Blunt et al., 2013; Devarapalli et al., 2017; Mees et al., 2003; Saxena et al., 2019; Saxena et al., 2018; Wang & Miller, 2020; Xiong et al., 2016). This makes it difficult for machine learning models to better capture causal relationships between fluid flow and what we know to be its main controls in pore-throats and pore connectivity since super high resolution needed to capture these controls of fluid flow in rock images is not available. This also implies that the weights learnt by CNN models are more correlative than causative, making it very difficult to have generalized models that can be applied to make predictions from data acquired from locations outside the area where the training data is collected. Another limitation in the use of CNN architectures is that it requires computational resource that you are not easily accessible for people to implement this approach for daily use due to the associated financial cost to access these resources. This includes the memory requirement to store the of image data required to adequately train CNN models and the CPU/GPU requirement required to execute complex calculations that occur deep in CNN model. It is noteworthy that these computational costs are associated with the development and training of machine learning models, the application of these trained models to substitute for traditional approaches is not computationally intensive and

returns result very fast. Furthermore, acquisition of image data of rocks is non-routine and expensive.

1.3 Hypothesis

A significant obstacle to precise prediction of the flow properties of heterogeneous rocks is the inability to replicate connectivity in rocks. This is because imaging rocks with enough resolution to see the spatial relationships between pore throats at a representative scale is technologically impossible. In order to achieve this, the main hypothesis of this study is that we can predict the most likely flow properties of rocks by accounting for pore connectivity through the stochastic reconstruction of pore microstructures with the same porosity and pore size distribution. To accomplish this, a statistically significant number of pore microstructures that take into account the likely flow paths that may have formed in each rock volume and the resulting flow properties must be created.

1.4 Study Objectives

The following goals were set for the dissertation:

i. To quantitatively evaluate the impact of pore connectivity on the permeability and hydraulic tortuosity of rocks, particularly how it changes as the level of heterogeneity varies in rocks. Additionally, to determine whether neural network technologies can accurately capture the stochastic nature of pore connectivity without explicitly including it in the training data.

ii. To improve the accuracy of predicting permeability of heterogenous rocks, particularly carbonate sedimentary rocks through a stochastic pore scale simulation

approach while optimizing the computational demand of numerical simulation of fluid flow with machine learning models.

iii. To develop a novel integrated workflow that aids the creation of high-resolution pore microstructural models at representative scale to help narrow the gap between flow properties of geological models and the measured flow properties of the rocks been modelled.

1.5 Significance of Study

This dissertation has broad implications in very key areas. This includes enhanced oil recovery and geological carbon storage (Shabani et al., 2020; Shabani & Vilcaez, 2019; Shabani & Vilcáez, 2017, 2019), as well as hydrogeological and environmental applications (Ebrahimi & Vilcáez, 2018a, 2018b, 2019). These applications depend significantly in the ability to predict the flow of fluid in the subsurface, hence, development of understanding and tools to improve forecast flow properties of rocks advances these geological use cases. Importantly, it could serve as a more cost-effective and time-efficient alternative for laboratory measurements of permeability.

1.6 Intellectual Merit

Pore connectivity constitutes the main source of complexity in understanding the relationship between the flow and transport properties and pore microstructure of carbonate rocks (He et al., 2014; Rashid et al., 2017). This is exacerbated by the inability to image this feature in rocks at scale because of challenges associated with technological limitations related to imaging at sufficient resolution (Bernabé et al., 2010; Civan, 2002;

Dasgupta & Mukherjee, 2020; Zhao et al., 2022). In this study, we utilize MATLAB®'s statistical capabilities to stochastically construct numerous pore connectivity scenarios (3D pore microstructures). Additionally, we employ STAR-CCM+®'s CAD and CFD capabilities to create surface files of the generated pore microstructures and simulate the associated transport properties for each possible pore connectivity scenario. It is essential to note that this approach is less significant for homogeneous rocks because there is less variation in pore connectivity. Therefore, a deterministic approach, such as flow simulation on direct high-resolution images or simple empirical correlations, is more suitable for siliciclastic rocks.

This research involves constructing 3D pore microstructures that possess the same porosity and pore size distribution as real carbonate rocks, but with different stochastic pore microstructure (pore connectivity). It is not necessary to obtain information on pore size distribution and porosity from images, as routine measurements such as MICP and NMR data can provide high-resolution data that is representative either individually or in combination with other acquisition methods. Constraining the generated pore microstructure with same pore size distribution and porosity helps to focus on pore connectivity, which is the primary source of uncertainty in developing a causal and predictive understanding between pore microstructure and transport properties of carbonate rocks.

Furthermore, this study utilizes machine learning techniques to optimize the implementation of the suggested workflow for general use. The novelty of the machine learning approach lies in its implementation, where machine learning technologies focus on a quantitative description of pore microstructural properties as input features, rather

than relying on images as inputs and using CNN as the machine learning architecture, as is typically done in predicting flow properties of digital rock images using machine learning. The approach employed in this study reduces the computational cost by using equivalent tabular data that capture the key information controlling flow instead of images. Additionally, it employs lighter algorithms such as gradient boosting, random forest, and simple artificial neural networks instead of CNN.

1.7 Dissertation Layout

The dissertation consists of three separate chapters, which are preceded by an introductory chapter (chapter I) and followed by a chapter containing conclusions and future work (chapter V). Chapters II, III, and IV covers different aspects of the research project and is written as an independent manuscript. Chapters II and III are already published while chapter IV is currently being reviewed by a peer-review journal.

Chapter II is published in Journal of Natural Gas Science and Engineering (2022 impact factor – 5.285):

Ishola, O., Alexander, A., & Vilcáez, J. (2022). Statistical and neural network analysis of the relationship between the stochastic nature of pore connectivity and flow properties of heterogeneous rocks. Journal of Natural Gas Science and Engineering, 105, 104719–. https://doi.org/10.1016/j.jngse.2022.104719

Summary of paper: The study employs a novel stochastic 3D pore-scale simulation approach to investigate the impact of stochastic pore connectivity on permeability and hydraulic tortuosity of heterogeneous porous media. The study generates multiple 3D pore

microstructures with the same porosity, pore size distribution, and number of pores, allowing for the isolated study of pore connectivity's role in permeability and hydraulic tortuosity. The approach suppresses the need for hundreds of experimental measurements and permits the training of neural network models to predict permeability and hydraulic tortuosity. The study reveals that the stochastic connectivity of pores significantly affects permeability but has only minimal effect on hydraulic tortuosity, while the predictability of permeability from hydraulic tortuosity decreases with increasing heterogeneity. This study also shows that NN algorithms can capture the effect of stochastic pore connectivity on permeability.

Chapter III is published in Fuel (2022 impact factor – 8.035):

Ishola, O., & Vilcáez, J. (2022). Machine learning modeling of permeability in 3D heterogeneous porous media using a novel stochastic pore-scale simulation approach. Fuel, 321, 124044–. https://doi.org/10.1016/j.fuel.2022.124044

Summary of paper: This study utilized a stochastic pore-scale simulation approach for improved permeability prediction. Porosity and pore size distribution were obtained from mercury injection capillary pressure measurements for four carbonate and five siliciclastic rock cores. The approach involved generating hundreds of 3D pore microstructures with different stochastic pore connectivity scenarios but the same porosity and PSD. Permeability was calculated by averaging the permeability distribution obtained from pore-scale flow simulations. This approach produced permeability estimations closer to measured permeability than five deterministic empirical model equations. Machine

learning reduced the required number of pore-scale simulations by 157 times and reproduced permeability estimates with a mean absolute percentage error of 10%.

Chapter IV is submitted to Fuel (2022 impact factor - 8.035):

Ishola, O., & Vilcáez, J. (2023). Augmenting Xray micro-CT data with MICP data for high resolution pore-microstructural and flow modelling of carbonate rocks (*Submitted*).

Summary of paper: Pore microstructural modeling typically relies on imaging technologies like SEM and micro-CT to obtain data on rock pore microstructures. However, these techniques often have limited ability to provide high-resolution data at a representative scale due to technological constraints. This study presents a new workflow that uses statistically representative data to generate pore microstructures with high resolution. The workflow incorporates MICP data for pore throat size distribution, micro-CT images for pore body size distribution, and stochastic modeling for pore connectivity.

CHAPTER II

STATISTICAL AND NEURAL NETWORK ANALYSIS OF THE RELATIONSHIP BETWEEN THE STOCHASTIC NATURE OF PORE CONNECTIVITY AND FLOW PROPERTIES OF HETEROGENEOUS ROCKS

2.1 Abstract

We used a stochastic 3D pore-scale simulation approach to statistically elucidate the effect of stochastic pore connectivity on permeability and hydraulic tortuosity of highly heterogeneous porous media such as carbonate rocks. The novel nature of our workflow lies in the generation of multiple 3D pore microstructures of the same effective porosity, pore size distribution, number of pores, but different stochastic pore connectivity where the only pore microstructural feature changing is pore connectivity. This workflow allows the explicit study of the role pore connectivity plays in permeability and hydraulic tortuosity without the interference of other pore microstructural factors or noise. Permeability and hydraulic tortuosity of the 3D pore microstructures of the aforementioned characteristics was obtained from direct pore-scale simulations using STAR CCM+. Our approach suppresses the necessity of conducting hundreds of experimental measurements and allows the training of neural network models to predict permeability and hydraulic tortuosity. We show that an approximate twofold increase in heterogeneity (pore size standard deviation), results in a two orders of magnitude reduction

in permeability, and that an increase in heterogeneity results in a systematic shift of permeability from normal distribution to lognormal distribution. While the stochastic connectivity of pores has a significant impact on permeability, it has only minimal effect on hydraulic tortuosity. Furthermore, the predictability of permeability from hydraulic tortuosity decreases with an increasing heterogeneity. The high coefficient of determination obtained in permeability prediction with a feedforward neural network (NN) model trained with of PTSD data along with pore surface area parameters indicates that NN algorithms can capture the effect of stochastic pore connectivity on permeability. Since PTSD data and surface parameters can be obtained from mercury injection capillary pressure (MICP) measurements, our findings have large implication toward the prediction of permeability and hydraulic tortuosity in highly heterogeneous porous media.

2.2 Introduction

Predictions of subsurface flow processes requires knowing the flow and transport properties of subsurface porous media, among which permeability and hydraulic tortuosity are the main flow and transport properties dictating flow of fluids and transport of solutes. Permeability is the ease of fluid flow through porous media (Friedman, 1976; Zhang, 2013) and hydraulic tortuosity is the ratio of actual flow path length to the straight-line distance between ends of the flow path (Carman, 1937; Clennell, 1997; Kozeny, 1927). Permeability of porous media is traditionally computed from deterministic model equations that relate permeability to other properties such as porosity, sphericity of grains, hydraulic tortuosity, and surface area (Carman, 1937; Kozeny, 1927). While permeability values obtained from deterministic equations are relatively effective to predict the flow of

fluids in homogeneous porous media such as siliciclastic rocks and soil materials, they do not always suit flow prediction in highly heterogeneous porous media such as carbonate rocks (He et al., 2014). The use of porosity as the key parameter in estimating permeability of carbonate rocks is known to be very erratic. It has been shown that a single porosity value can have a five-order of magnitude range in permeability (Westphal et al., 2005). This is due to the complex pore microstructure of carbonate sedimentary rocks. Fundamentally, flow and transport properties of porous media are a function of pore size distribution and random pore connectivity that can result in complex heterogeneous pore microstructures (Algive et al., 2012; Chen et al., 2015; Cheng et al., 2019). Pore connectivity describes the degree of connection between pores in a rock. The magnitude of pore connectivity is the sum of the effects of pore-throat sizes (Dutton & Loucks, 2010) and the average number of pores connected to a single pore in a rock (Bernabé et al., 2010; Dutton & Loucks, 2010). Capturing the complexity of pore connectivity in carbonate rocks requires stochastic models (Whitten, 1977). This has been shown to better represent flow behavior in complex heterogeneous systems compared to deterministic approaches (Apostolopoulou et al., 2019).

To consider the effect of pore size distribution, permeability can be estimated from Nuclear Magnetic Resonance (NMR) data using the Timur-Coates (TC) equation (Timur, 1968) and the Schlumberger-Doll-Research (SDR) equation (Kenyon, 1992). The use of pore size distributions has been shown to yield more accurate rock permeability values compared to the sole use of porosity (Westphal et al., 2005). That said, its application in carbonate sedimentary rocks is still problematic due to heterogeneity (Choquette & Pray, 1970) and pore connectivity (Westphal et al., 2005). This is because the TC and SDR

equations assume that pores are evenly distributed and evenly connected which is not true (Westphal et al., 2005). In fact, these model equations are known to over-estimate permeability due to the use of total porosity instead of effective porosity as the porosity parameter (Westphal et al., 2005). Mercury injection capillary pressure (MICP) is another tool employed to estimate permeability of rocks of complex pore microstructures through empirical model equations (Rahul Dastidar, Carl H Sondergeld, et al., 2007; Jairam Kamath, 1992; S. Kolodzie, 1980; Pittman, 1992; Purcell, 1949; B. Swanson, 1981; Wells & Amaefule, 1985). MICP provides pore-throat size distributions within a rock. The use of MICP data in predicting permeability usually relies on a percentage of mercury saturation in a rock sample (Jairam Kamath, 1992; S. Kolodzie, 1980; Pittman, 1992; Purcell, 1949; B. Swanson, 1981; Wells & Amaefule, 1985) or a weighted average of pore-throat sizes obtained from MICP (Rahul Dastidar, Carl H Sondergeld, et al., 2007)and do not fully account for pore connectivity. Other methods employed in obtaining pore size distribution of rocks includes the use of scanning electron microscope (SEM), focused ion beam-scanning electron microscope (FIB-SEM), micro-CT scanners, and gas adsorption techniques (Anovitz & Cole, 2015; Blunt et al., 2013; Xiong et al., 2016). Like permeability, hydraulic tortuosity is usually estimated from deterministic model equations that employs porosity as the key parameter (Kimura, 2018; Lala, 2020). Such estimates of hydraulic tortuosity might also mislead in reactive and/or solute transport simulations given that size of individual pores and their connectivity might play a significant role in the path through which solutes are transported in complex pore microstructures.

At present, a predictive understanding of the relationship between complex pore microstructure and flow properties of carbonate sedimentary rocks is not fully developed

(Bijeljic et al., 2013; Zhang & Cai, 2021), leading to the reliance on empirically derived permeability and hydraulic tortuosity properties obtained by analogy or statistical analysis of past data(England, 1994). This is associated with enhanced oil recovery, geological carbon storage (Shabani et al., 2020; Shabani & Vilcaez, 2019; Shabani & Vilcáez, 2017, 2019; Vilcáez, 2020), and petroleum produced water disposal (Ebrahimi & Vilcáez, 2018a, 2018b, 2019; Vilcáez, 2020), for instance. To improve this understanding, this study employs a stochastic pore-scale simulation approach. The approach consists of constructing hundreds of 3D pore microstructures of the same effective porosity, pore size distribution, number of pores, but different stochastic pore connectivity, just like it happens in rock samples. Permeability and hydraulic tortuosity of the constructed 3D pore microstructures of the aforementioned characteristics are obtained from direct pore-scale simulations. The use of direct pore-scale simulations to obtain permeability and hydraulic tortuosity is a standard practice in pore-scale modeling (Soete et al., 2017; Vilcáez et al., 2017).

Our hypothesis is that enough pore microstructures where the only pore microstructural feature changing is pore connectivity allows improved investigation into the role of pore connectivity in fluid flow without the interference of other factors. Furthermore, it will help assess the predictability of pore-scale permeability and hydraulic tortuosity without explicit inclusion of pore connectivity in feedforward neural network (NN) models. Feedforward NN is a type of artificial neural network architecture where neurons are grouped by layers and connections which only move in the direction of the output (Al Khalifah et al., 2020; Erofeev et al., 2019; Mendes et al., 2002). NN is chosen as the machine learning algorithm for this study because of its ability to deduce the best

set of weights that map a set of input features to the desired target. This ability is useful in this study because pore connectivity is random, and it is the only pore microstructural parameter varying. Hence, the random nature of pore connectivity is captured by NN if accuracy of prediction on test dataset is high. Other popular NN approaches in geosciences includes convolutional neural network (CNN) which is often used for making predictions from image data (Graczyk & Matyka, 2020; Tembely et al., 2021) and recurrent neural networks (RNN) which was developed for sequential or time series data (Jiang et al., 2021; Song et al., 2020). More recently, bayesian neural networks (BNN) are being used to take uncertainty into account and overcome overfitting which is one of the principal challenges of neural networks (R. Feng et al., 2021; Runhai Feng et al., 2021). The novel nature of our workflow lies in the generation of multiple pore microstructures where the only pore microstructural feature changing is pore connectivity. This workflow allows elucidation of the role pore connectivity on permeability and hydraulic tortuosity without the interference of other pore microstructural factors, noise, and/or assumptions. Hence, we can determine the degree of influence of pore connectivity on pore microstructures with respect to set levels of heterogeneity and evaluate if NN models capture the stochastic nature of pore connectivity.

2.3 Methods

2.3.1 Stochastic construction of 3D pore microstructures

To elucidate the effect of random pore connectivity on permeability and hydraulic tortuosity of highly heterogeneous porous media, three groups of 3D pore microstructures were generated. The 3D pore microstructures in each group had the same pore size

distribution and effective porosity but different stochastic connectivity between the pores (Fig. 2.1). The input data used to generate each group of the 3D pore microstructures are pore geometry, effective porosity, and pore size distribution (PSD). Spheres were used as the pore geometry in this study because the focus is on pore connectivity, thus, we needed to constrain pore geometry. It is noteworthy that the use of spherical pores is routine in pore network modelling (Baychev et al., 2019; Huang et al., 2020; Yang et al., 2018; Zheng et al., 2022). The effective porosity of all the generated 3D pore microstructures is consistent with an average of 19% and a coefficient of variation of 1%. Coefficient of variation (CV) reflects the degree of variation in data from the mean. CV is mathematically expressed as:

$$CV = \frac{Standard\ deviation}{m} * 100 \tag{2.1}$$

$$Standard\ deviation = \sqrt{\frac{1}{n}\sum_{i=1}^{n}(D_i - m)^2} \tag{2.2}$$

where n is the number of pores, D_i is the diameter of pore i, and m is the mean diameter of the pores.

Lognormal distribution curves were used to represent PSD because of their frequent use to describe PSD of rocks (Ding et al., 2015; Huang et al., 2019; Li et al., 2019; Munawar et al., 2021; Naraghi & Javadpour, 2015; Niu & Zhang, 2018). For this study, the mean pore size of all generated 3D pore-microstructures is 10 μm with a pore size standard deviation of 0, 5, and 11 μm for groups I, II, and III, respectively (Fig. 2.2). While the average pore size in rocks can vary widely, a dominant pore size of about 10 μm has been reported for different diagenetic stages of carbonate (van der Land et al., 2013). The

increase in standard deviation in each group is to mimic different levels of heterogeneity in real rock samples. By implication, group I with a standard deviation of 0 is comprised of pores of the same sizes but stochastic pore connectivity (Fig. 2.1.A) and a higher pore size standard deviation corresponds to an increased degree of heterogeneity in PSD (Fig. 2.1.B and 2.1 C). Groups I, II, and III comprises of 991, 990, and 805 3D pore-microstructures respectively. The average number of pores in each 3D pore microstructures was 973 with a CV of 3% across all the generated 3D pore microstructures. The number of pores in all three groups of 3D pore microstructures are practically the same to suppress the effect of number of pore-throats on permeability and hydraulic tortuosity.

The generation of 3D pore microstructures of stochastic pore connectivity was done using statistical tools on MATLAB together with the CAD capabilities of STAR CCM+® (a computational fluid dynamics software by Siemens). The procedure consisted of the generation of random sizes of pores based on a given mean pore size and standard deviation of the PSD curve. The coordinates of pores and thus the stochastic connectivity between pores in the 3D pore microstructure was decided using a uniform distribution function. This ensured an equal probability of selecting the location of the pore in the 3D pore micro-structure and an equal probability in the degree of overlap between the pores. Two controls were then applied. The first control was to ensure that the first pore is centered in the 3D pore microstructure. This guarantees that the pores are not concentrated in certain regions of the 3D pore microstructures, allowing the pore networks to spread out inside the respective rock domains. The second control was to ensure that all the pores were connected; hence porosity is equivalent to effective porosity in this study. The generation of the 3D pore microstructures was automated and run on Oklahoma State

University's Pete Supercomputer, which provided 32 cores and 96 GB of RAM for each run. It took 5–35 min to generate each 3D pore microstructure.

The rock domain within which the 3D pore microstructures are generated is a cube (Fig. 2.1) with varied length scale across the three groups. This is due to the need to have a relatively fixed effective porosity, PSD, and number of pores in each group. To verify that the varying length scales do not impact the study, a representative elementary volume (REV) analysis was conducted (Bear, 1972). This analysis has been used in several studies to justify that macroscopic properties (e.g., porosity, organic matter content, and specific surface area) are not controlled by sample volume (Mostaghimi et al., 2013; Peng et al., 2012; Saraji & Piri, 2015; Wu et al., 2017). For this study, the REV analysis was conducted based on average pore size to guarantee that the pore size distribution and porosity is consistent for pore-microstructures in each group. Here, the number of pores in the 3D pore microstructures is sufficient when the difference between the averages of the pores sizes is insignificant as the number of pores is increased further. Furthermore, the mean of the PSD used to generate the data set is known (10 μm); therefore, the mean pore size at REV must be closer to this number. The REV analysis was conducted for group III of 3D pore microstructures since this group constitutes the most severe scenario of heterogeneity; hence, it requires the largest number of pores to reach a representative value. Fig. 2.3 shows 700 pores to be representative for the range of pore sizes used in this study. By contrast, the average number of pores in this study is 973, resulting in a length scale of 133 μm for group I, 169 μm for group II, and 302 μm for group III of 3D pore microstructures.

2.3.2 Pore-scale simulations of flow

Simulation of incompressible flow through the generated 3D pore microstructures of stochastic pore connectivity was conducted with STAR-CCM+® which uses the finite volume methodology to solve the mass continuity equation:

$$\vec{\nabla} \cdot \rho\vec{V} + \frac{\partial \rho}{\partial t} = 0 \tag{2.3}$$

and Navier-Stokes momentum equation:

$$\frac{\partial \vec{V}}{\partial t} + \left(\vec{V} \cdot \vec{\nabla}\right)\vec{V} = -\frac{1}{\rho}\vec{\nabla}P + v\vec{\nabla}^2\vec{V} \tag{2.4}$$

where ρ is density of the fluid, v is kinematic viscosity, P is pressure, t is time, and $\vec{V}$ is fluid velocity.

STAR-CCM+® has been shown in previous works to accurately replicate fundamental pore-scale flow (Yang et al., 2016; Yang et al., 2013) and solute transport processes (Oostrom et al., 2014; Yang et al., 2016). The first step in flow simulation was to conduct a mesh independence study to ensure that flow velocity profiles obtained from solving the governing equations (2.3) and (2.4) is independent of the mesh resolution. Twenty samples were randomly selected for this purpose. It involves steadily increasing the number of cells in a flow domain and computing the average velocity. A model is deemed mesh independent when the change in average velocity is insignificant for an increase in the minimum cell size (See Fig. 2.1S in the supplementary data). The final mesh was generated with a minimum cell size of 0.75 μm with other parameters at default. For this study, an unstructured polyhedral mesh type was used. This helped capture the complex nature of the 3D pore microstructures (Fig. 2.4).

The average number of cells per pore microstructure is 640,000 which ultimately results in an average computational time of 15 min per simulation. The governing equations (2.3) and (2.4) were solved for a steady state condition. For simplicity, the fluid used in the simulations was water with no chemical reaction between the fluid and the pore microstructures. The rock domain had closed boundaries except for two opposite sides through which flow was allowed. A stagnation inlet pressure condition was applied at the inlet with a fixed pressure of 1 Pa while an outlet pressure of 0 Pa is fixed at the outlet, maintaining a pressure drop of 1 Pa across the two open boundaries (Fig. 2.4). A no-slip wall condition was applied to the remainder of the computational domain. The Reynolds number of the flow simulations were less than 0.0001 in all 3D pore-microstructures in this study. This makes the calculation of permeability with Darcy's law valid in all the generated 3D pore-microstructures (Chen et al., 2015). Each pore-scale numerical simulation reached steady state conditions before 150 iterations (See Fig. 2.2S in the supplementary data). Simulations are stopped at the 200th iteration and solutions are deemed to converge when the mass flow at the inlet and the outlet are equal and within 0.1% of the respective mass flow in the prior iteration. A secondary condition was also added to ensure that the residuals (continuity, x momentum, y momentum, and z momentum) are all less than 10^{-6}. This process was automated and run on the same supercomputing cluster used in generating the 3D pore microstructures.

2.3.3 Permeability estimation

Permeability was calculated from Darcy's equation (Chen et al., 2015; Darcy, 1856; Vilcáez et al., 2017). Mathematically, Darcy's equation is expressed as:

$$K = \frac{V \times \mu \times L}{\Delta P} \tag{2.5}$$

where V is the Darcy flow velocity in the rock domain in m/s, K is the absolute permeability of the rock domain in m^2, ΔP is the pressure drop in the principal direction of the fluid in Pa, μ is the dynamic viscosity of the fluid in Pa-s, and L is the length along the direction of the pressure drop in meters. Calculated permeability was converted from m^2 to mD.

Darcy flow velocity can be rewritten as:

$$V = \frac{Q}{A} \tag{2.6}$$

where Q is the volumetric flowrate through the inlet or outlet in m^3/s and A is the cross-sectional area perpendicular to the flow at the respective boundary in m^2.

Volumetric flowrate can also be rewritten as:

$$Q = \frac{M}{\rho} \tag{2.7}$$

where M is the mass flowrate through the inlet or outlet in kg/s and ρ is the density of the fluid flowing through the medium in kg/m^3.

Combining (2.6) and (2.7):

$$V = \frac{M}{A * \rho} \tag{2.8}$$

Combining (2.5) and (2.8):

$$K = \frac{M \times \mu \times L}{\Delta P * A * \rho} \tag{2.9}$$

Since properties of the fluid (density and viscosity of water) and pressure drop are constant, permeability is calculated from mass flow rate and length scale (L^{-1}) of the digital rock domain.

2.3.4 Hydraulic tortuosity estimation

Hydraulic tortuosity can be calculated in terms of the flow velocity (Duda et al., 2011; Vilcáez et al., 2017):

$$\tau = \frac{V}{V_i} \tag{2.10}$$

where V is the average magnitude of the intrinsic velocity over the entire system volume in m/s, and V_i is the volumetric average of the component parallel to the macroscopic flow direction in m/s.

By implication, the smallest possible hydraulic tortuosity is 1, which indicates a straight-line flow path. An increase in the hydraulic tortuosity value translates into more tortuous and longer flow path.

2.3.5 Pore microstructural parameters

To elucidate the effect of stochastic pore connectivity on permeability and hydraulic tortuosity of complex heterogeneous rocks, the following parameters were obtained from the generated 3D pore microstructures.

2.3.5.1 Pore-throat sizes

The pore-throat size is the length at the intersection between two pores (Fig. 2.5). Pore-throats sizes are constrained by the sizes of the pore they connect since a pore-throat cannot be larger than the size of the pores they are connecting. The size of the pore-throats for each group of 3D pore microstructures were calculated, resulting in a relatively uniform pore-throat size distribution (PTSD) for 3D pore microstructures constructed from uniform PSD (Fig. 2.6A) and a lognormal PTSD for 3D pore microstructures constructed from lognormal PSD (Fig. 2.6B and C).

2.3.5.2 Surface area

The surface area (*S*) of each 3D pore microstructure was calculated. Although surface area is not a direct subject of this study, it plays a key role in the velocity distribution in porous media. This is because of the no-slip condition at the pore-fluid boundary resulting in zero velocity at the pore walls. Therefore, it has an inverse relationship with the average flow velocity through porous media which is consequential for permeability and hydraulic tortuosity. Two parameters were derived from the surface area, namely pore volume normalized surface area (*pS*) which is given by:

$$pS = \frac{S}{P} \tag{2.11}$$

and bulk volume normalized surface area (*bS*) which is given by:

$$bS = \frac{S}{B} \tag{2.12}$$

where *S*, *P*, and *B* are the surface area of pores (m^2), pore volume (m^3), and the bulk volume of the digital rock (m^3) respectively.

2.3.6. Neural network implementation

A feedforward neural network (NN) was applied to assess the predictability of permeability and hydraulic tortuosity using PTSD data and surface area parameters. Ten features were used for training the NN algorithm. This includes bulk volume normalized surface area (*bS*), pore volume normalized surface area (*pS*), standard deviation of the PTSD, 1st percentile of the PTSD, 10th percentile of the PTSD, 25th percentile of the PTSD, 50th percentile of the PTSD, 75th percentile of the PTSD, 90th percentile of the PTSD, and domain length scale. The domain length scale accounts for the different length scales of the three groups of 3D pore microstructures. The targets are permeability and hydraulic tortuosity. Correlation between all the features and targets were examined in each group to help evaluate the predictability of the targets from individual features and identify possible multicollinearity between features used in this study (See Table 2.1S, 2.2S and 2.3S in the supplementary data). The features and targets from the three groups were combined for use in the NN algorithm to maximize its performance. In the pre-processing stage of the NN algorithm deployment, the data was randomly split into training, validation, and test data in a 7:1:2 ratio, respectively. The data was randomly sampled to remove bias and the percentage of training data is deemed sufficient given the total size of our data (Verdhan, 2020). The training data was used to train the NN algorithm while the validation data were used to check the predictability of the target properties with the NN algorithm after each epoch to guard against overfitting. The test data was finally used to check the predictability of permeability and hydraulic tortuosity from the trained NN algorithm. Prior to training, the features were standardized using the z-scoring technique (Mohamad & Usman, 2013). The NN architecture of the permeability model

used in this study comprised of an input layer, two hidden layers with 64 neurons each, an output layer, and a 10% dropout before the output layer as a second measure to prevent overfitting. The two hidden layers in the permeability model were assigned sigmoid activation functions. For the hydraulic tortuosity model, the NN architecture is made up of an input layer, a single hidden layer with 64 neurons and tanh activation function, and an output layer. The loss function used in both models is the mean squared error which was minimized with the Adam optimizer (Kingma & Ba, 2014) at a learning rate of 0.001. The choices of activation function, number of neurons, and number of hidden layers were based on comparative performance when tuning the hyperparameters. A linear activation function was used as output since both target properties are continuous values. The epoch was set to 20,000 with a patience of 100. The best training weights was selected based on the mean squared error of the validation data.

2.4 Results and discussion

2.4.1 Heterogeneity and permeability

Table 2.1 summarizes mean permeability values estimated for groups I, II, and III of 3D pore microstructures of different degree of heterogeneity (pore size standard deviation). As expected, an increase in the degree of heterogeneity (pore size standard deviation) reduces permeability because effective porosity and the number of pores in all generated 3D pore microstructures is approximately the same. If effective porosity and the number of pores is the same, an increase in heterogeneity results in an increase of the number of smaller pore-throats as shown in Fig. 2.6. Since pore-throat sizes are generally smaller when heterogeneity is increased and pore-throats are always smaller than pore

bodies (Fig. 2.5), it is apparent that PTSD is a key control of permeability. An approximate twofold increase in heterogeneity (pore size standard deviation) from group I to group III results in decrease of the mean pore-throat size from 5.99 μm to 3.79 μm (Fig. 2.6) and a two orders of magnitude reduction in average permeability from 28.5 mD to 0.27 mD (Table 2.1).

The resulting lognormal permeability distribution (Fig. 2.7) has been reported for real rocks (Malin et al., 2020; Sahin et al., 2007) validating the stochastic pore-scale simulation approach used in this study. A key contribution of this study is that an increase in heterogeneity also results in an increase of the skewness and kurtosis of the permeability distribution curves (Fig. 2.7) which represents a systematic shift of permeability from normal distribution to lognormal distribution. This also results in an increase in the CV of permeability from 24% to 161% (Table 2.1). Fig. 2.8 shows that the average permeability for each group does not significantly change when the number of generated 3D pore microstructures is more than 300, indicating that representative nature of this analysis. By implication, the use of Gaussian techniques to obtain permeability realizations using geostatistics (e.g., Kriging) is not recommended in modelling and simulations of fluid flow. The larger the standard deviation of pore size in the PSD of a rock, the more skewed and long tailed the distribution of permeability that can be associated to the rock. Furthermore, variation in the permeability of group I with uniform PSD is an indication that PSD is not enough to accurately predict the permeability of rocks. This is because even if pore size is the same, pore-throat size is varying due to the stochastic nature of pore connectivity (Fig. 2.6A). Hence, it is more reliable to obtain permeability prediction from PTSD compared to the use of porosity and/or PSD. Heterogeneity also impacts the

relationship between permeability and hydraulic tortuosity. Fig. 2.9 shows the predictability of permeability from hydraulic tortuosity to decrease with an increase in heterogeneity. The deteriorating relationship is evident from the decreasing R^2 value. Therefore, equations that leverage on the relationship between permeability and hydraulic tortuosity such as the Kozeny (1927) and Kozeny-Carman models (Carman, 1937) might give misleading estimates of flow properties in heterogeneous porous media.

2.4.2 Heterogeneity and hydraulic tortuosity

Table 2.2 summarizes mean hydraulic tortuosity values estimated for groups I, II, and III of 3D pore microstructures of different degree of heterogeneity (pore size standard deviation). An increase in heterogeneity increases the average hydraulic tortuosity in each group. This is expected given the inverse relationship between heterogeneity and permeability (Table 2.1) and the inverse relationship between hydraulic tortuosity and permeability (Fig. 2.9). Fig. 2.8 shows that the average hydraulic tortuosity does not significantly change after 300 samples, indicating the representative nature of this study. Like the distribution of permeability, the distribution of hydraulic tortuosity is more skewed and long tailed (Table 2.2 and Fig. 2.10) as heterogeneity (standard deviation of PSD) increases from group I to group III (Fig. 2.1). However, it is still close to a normal distribution in the most severe case of heterogeneity (Fig. 2.10). Furthermore, there is only a small change in mean hydraulic tortuosity across the three groups, implying that PTSD resulting from the random connectivity of pores does not have a significant effect on hydraulic tortuosity. However, it is noteworthy the results in Table 2.2 indicates that hydraulic tortuosity of rocks will generally vary even if the porosity and PSD is the same.

2.4.3 Permeability and hydraulic tortuosity predictability with neural networks

Fig. 2.11 compares direct pore-scale simulations and NN predictions of permeability and hydraulic tortuosity. The coefficient of determination (R2) of permeability and hydraulic tortuosity are 0.94 (Fig. 2.11.A) and 0.23 (Fig. 2.11.C) respectively. The high coefficient of determination obtained with the use of the NN to predict permeability indicates NN algorithms trained using PTSD data and surface area parameters can significantly capture the stochastic nature of pore connectivity of real rocks. Furthermore, the addition of hydraulic tortuosity as a parameter in permeability prediction improves the R^2 metric from 0.94 to 0.98 (Fig. 2.11.A and 11.B). Hydraulic tortuosity prediction with the corresponding NN model is poor. However, the coefficient of determination for hydraulic tortuosity prediction increases from 0.24 to 0.50 when permeability is added to the training parameters (Fig. 2.11.C and 2.11.D). It is worth noting that the mean absolute error of the test data is only 0.23 without permeability as a parameter and 0.17 when permeability is added as a parameter. These errors are very small compared to the ranges of possible hydraulic tortuosity, up to 4.5 (Fig. 2.10) for a single porosity value that was used in this study, underlying the merits of using NN with parameters selected in this study compared to model equations that estimate hydraulic tortuosity directly from porosity. The use of NN model for prediction of permeability and hydraulic tortuosity as used in this study is practical since PTSD data, surface area parameters, and domain length can be obtained from MICP measurements and routine analysis. The inclusion of permeability-hydraulic tortuosity relationship in the respective NN models has been shown to be beneficial (Fig. 2.11); however, it might also have a

negative effect on performance if model is not properly trained (Fig. 2.12). At smaller epochs, the inclusion of permeability-hydraulic tortuosity relationships in both NN models could worsen performance (Fig. 2.12). Hence, establishing an optimal number of epoch is very vital.

2.5 Conclusions

This study has employed a stochastic pore-scale simulation approach to statistically elucidate the effect of stochastic pore connectivity on permeability and hydraulic tortuosity of highly heterogeneous porous media such as carbonate rocks. Furthermore, we assessed the capacity of NN to capture the stochastic nature of pore connectivity. The novelty of this study lies in the generation of multiple pore microstructures where the only pore microstructural feature changing is pore connectivity, allowing the explicit study of the role of pore connectivity on flow without the interference of other factors. The key findings from this novel approach are as follow:

1. An increase in heterogeneity (pore size distribution) drives the distribution of permeability farther from normal distribution towards lognormal distribution. This can be crucial when introducing permeability heterogeneity into reservoir scale models of permeability. Like permeability, hydraulic tortuosity also deviates from normal distribution; however, the degree of divergence from normal distribution is insignificant.
2. Pore-throat size distribution and pore surface area obtainable from rock MICP data can be leveraged in machine learning algorithms such as feedforward neural networks to make predictions of permeability with a high degree of accuracy. On the other hand, hydraulic

tortuosity is poorly predicted using the same approach which suggests that pore-throats or surface area are not the key controls of hydraulic tortuosity.

3. The use of NN could serve as an efficient alternative to direct pore-scale simulations of permeability which are computationally intensive.
4. In comparison to model equations that employ porosity and/or pore size distribution as the key predictive parameter for permeability and hydraulic tortuosity, the use of feedforward neural network provides a better prediction given the variability in permeability and hydraulic tortuosity obtained at a fixed porosity and pore size distribution particularly when heterogeneity is high.
5. The relationship between permeability and hydraulic tortuosity deteriorates with increase in heterogeneity. Therefore, deterministic equations that relate permeability and hydraulic tortuosity (for example, the Kozeny-Carman equation) might be less reliable at higher degrees of heterogeneity in rocks.

In general, the outcome of this statistical and neural network analysis helps improve our understanding about the effect of heterogeneity and pore connectivity on fluid flow and solutes transport. This insight has a broader significance in enhanced oil recovery, geological carbon storage, petroleum produced water disposal, resource exploration and production, as well as the management of subsurface environment. Furthermore, it introduces a way to leverage the use of MICP data to make relatively accurate predictions of permeability and hydraulic tortuosity. In a follow up study, the established pore-scale stochastic approach will be used to predict permeability of actual carbonate rocks at Darcy's scale.

Acknowledgements

This material is based upon work supported by the National Science Foundation under Grant HS-2041648. We appreciate the Association of Petroleum Geologist Foundation (AAPG), Oklahoma Geological Foundation (OGF), and the Oklahoma City Section of Society of Petroleum Engineers (SPE) for partial financial support of the Ph.D. research of the first author. This is Oklahoma State University Boone Pickens School of Geology contribution number 2022- 129. Some of the computing for this project was performed at the High- Performance Computing Center at Oklahoma State University (OSU).

Figures

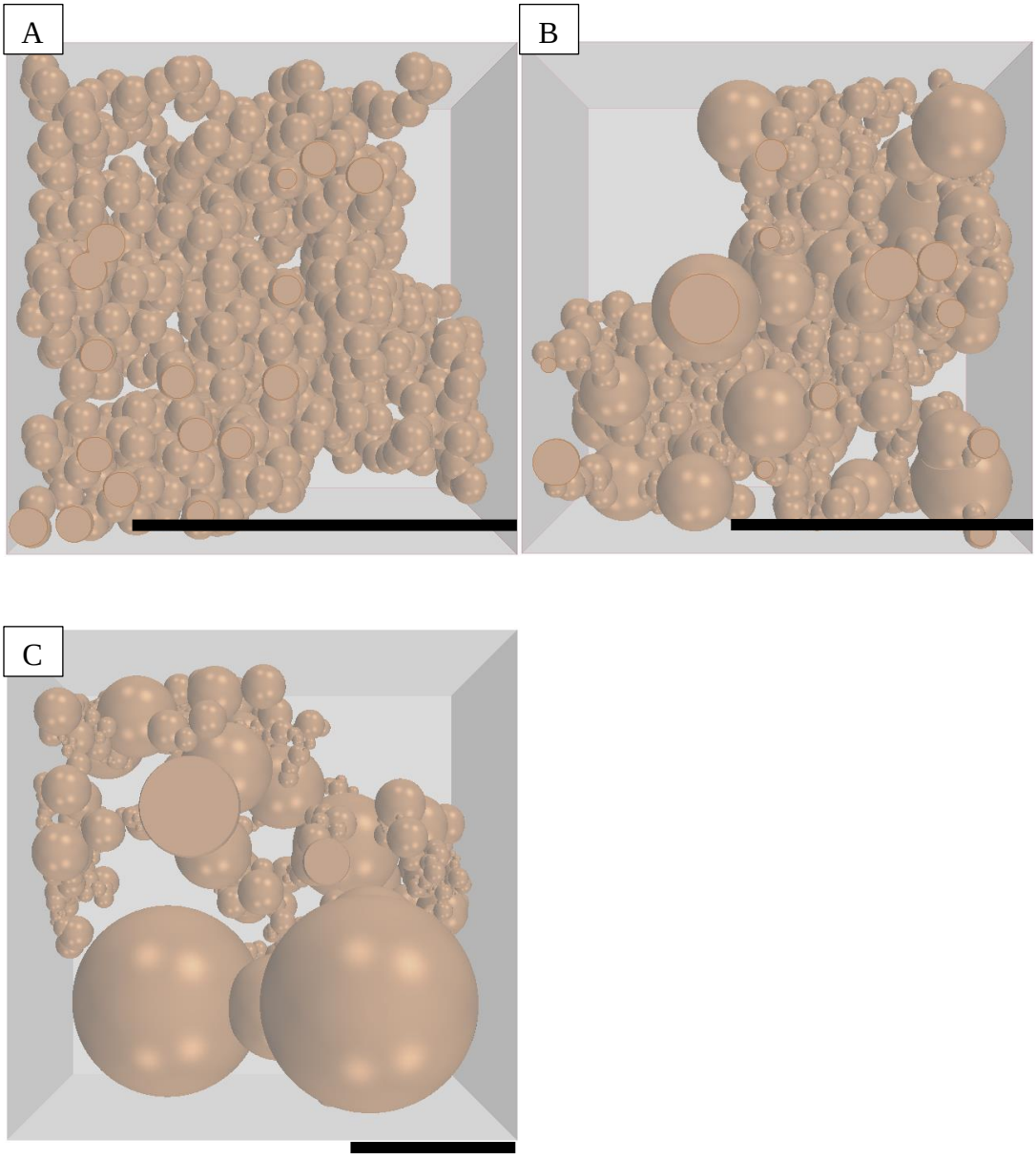

Fig. 2.1. Representative 3D pore-microstructures of stochastic pore connectivity. A) group I: 0 μm pore size standard deviation, B) group II: 5 μm pore size standard deviation, and C) group III: 11 μm pore size standard deviation. The mean pore size is 10 μm in all three groups. The brown spherical balls are the pores while the background is the solid matrix. The black bar represents 100 μm in the respective images.

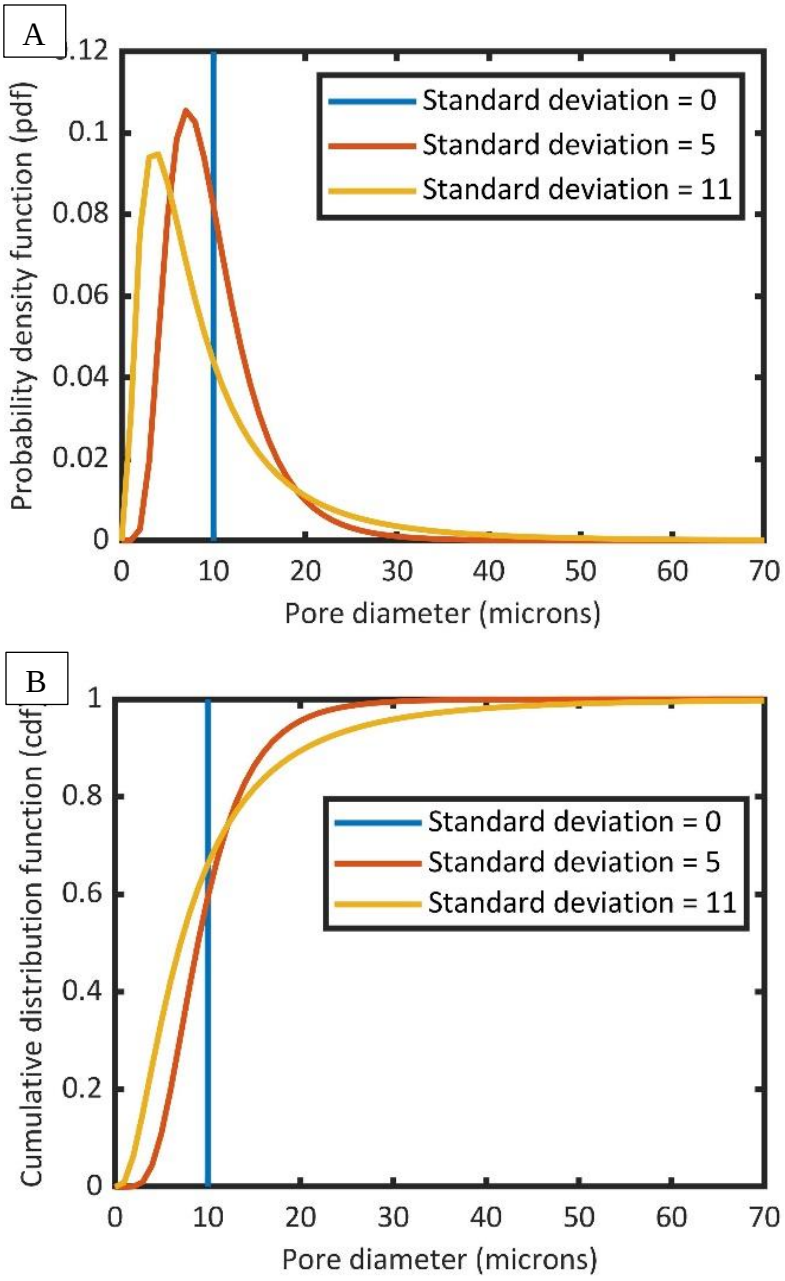

Fig. 2.2. Lognormal pore size distribution (PSD) curves employed to generate the 3D pore microstructures of stochastic pore connectivity. A) shows the probability density function (pdf) while B) is the corresponding cumulative distribution function (cdf). A pore size standard deviation of 0, 5, and 11 µm represents group I, II, and III respectively. The mean pores size is 10 µm in all three groups.

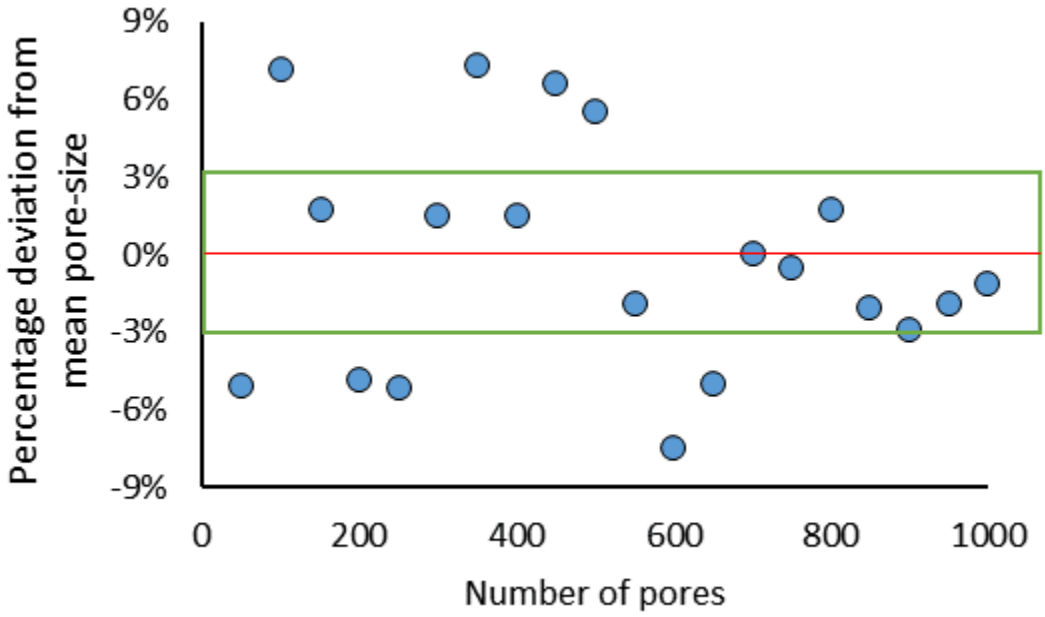

Fig. 2.3. Mean pore size REV analysis showing a minimum of 700 pores can be deemed representative because the percentage deviation from mean (red line) is within 3% (green box) when the number of pores is increased further.

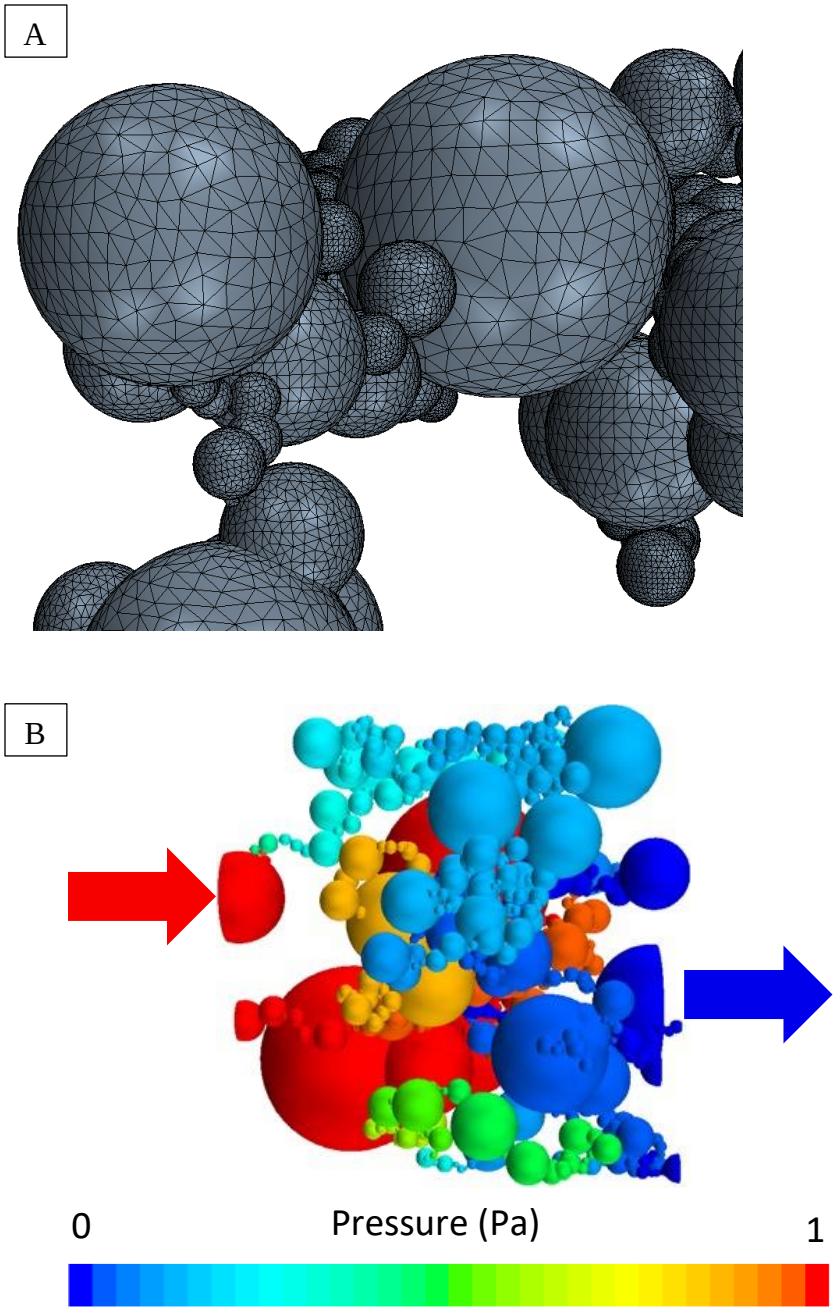

Fig. 2.4. Pore-scale simulations. A) A polyhedral mesh type was applied to adequately capture the complex nature of a 3D-pore-microstructure. The average pore size is 10 µm while the minimum cell size of the mesh is 0.75 µm. B) Representative pressure distribution across a 3D pore microstructure at steady state conditions. The inlet is on the left (red arrows) and the outlet is on the right (blue arrows).

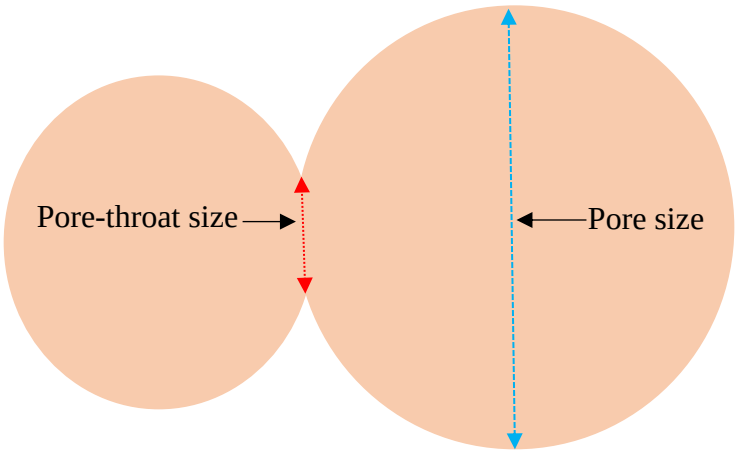

Fig. 2.5. A schematic comparing pore-throat (red line) and pore size (blue line).

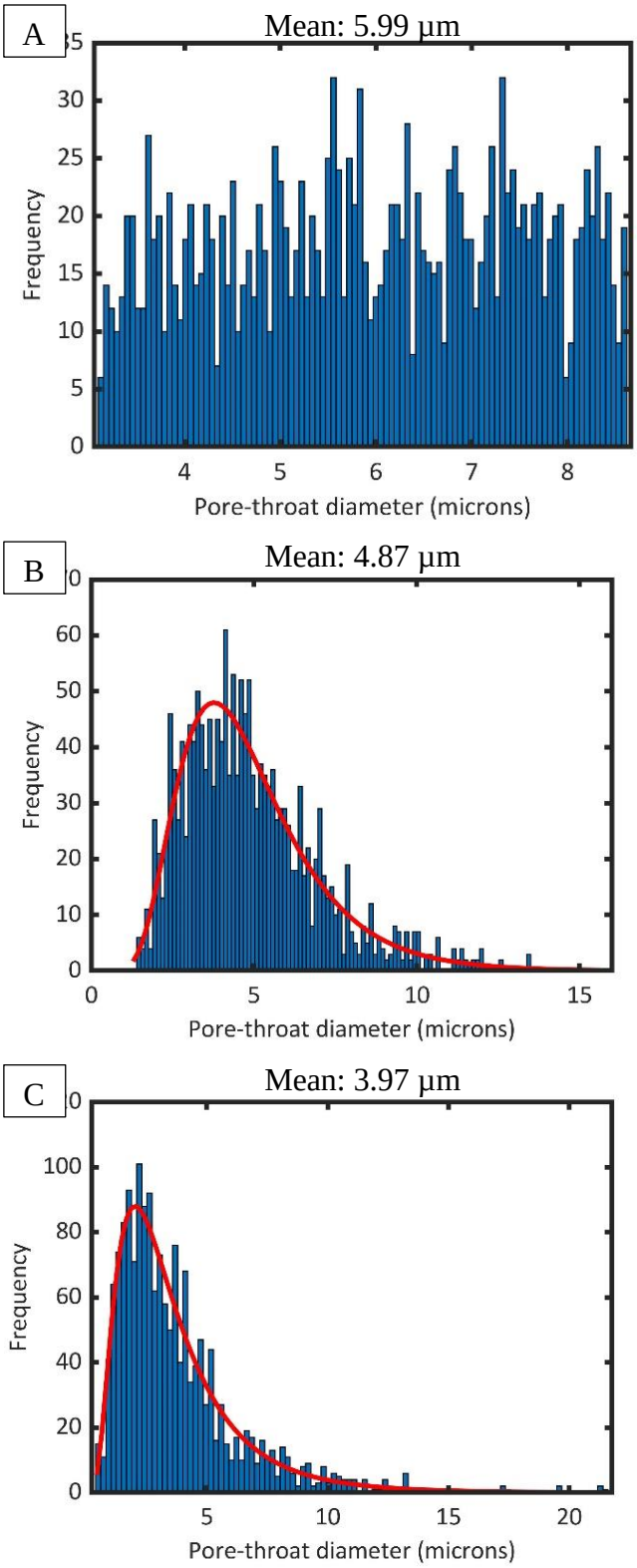

Fig. 2.6. Histogram of pore-throat size distribution of a single 3D pore microstructure for A) group I, B) group II, and C) group III.

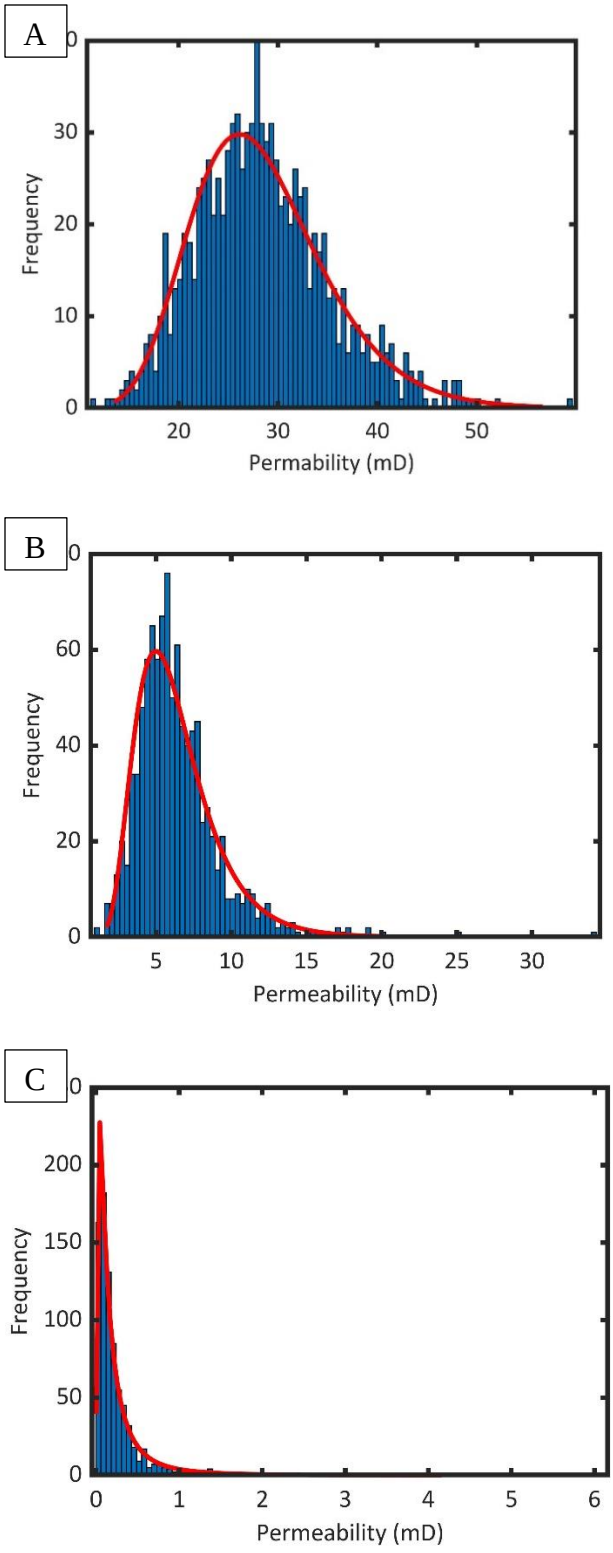

Fig. 2.7. A lognormal density function (red line) fitted on histograms of permeability distribution for (A) group I, (B) group II, and (C) group III.

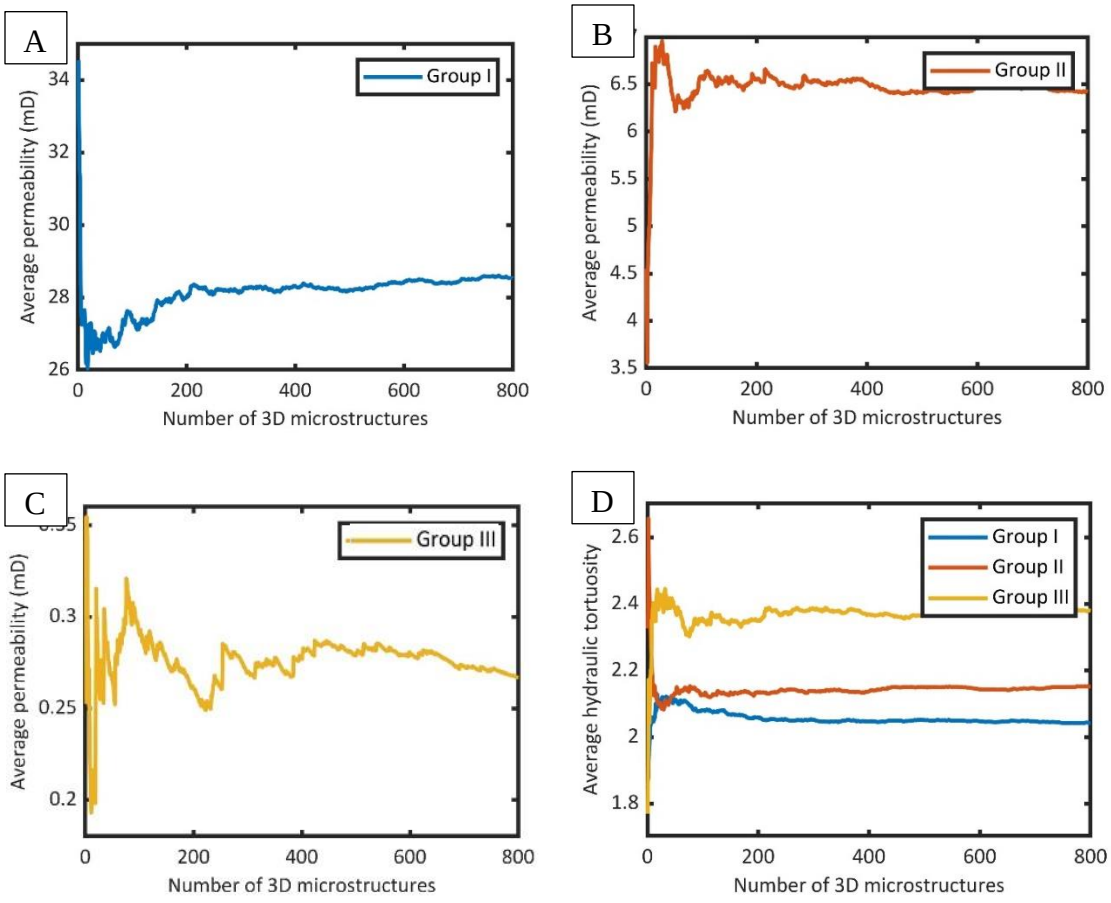

Fig. 2.8. A, B, and C shows the change in average permeability with the number of 3D pore microstructures while D shows the change in average hydraulic tortuosity with the number of 3D pore microstructures.

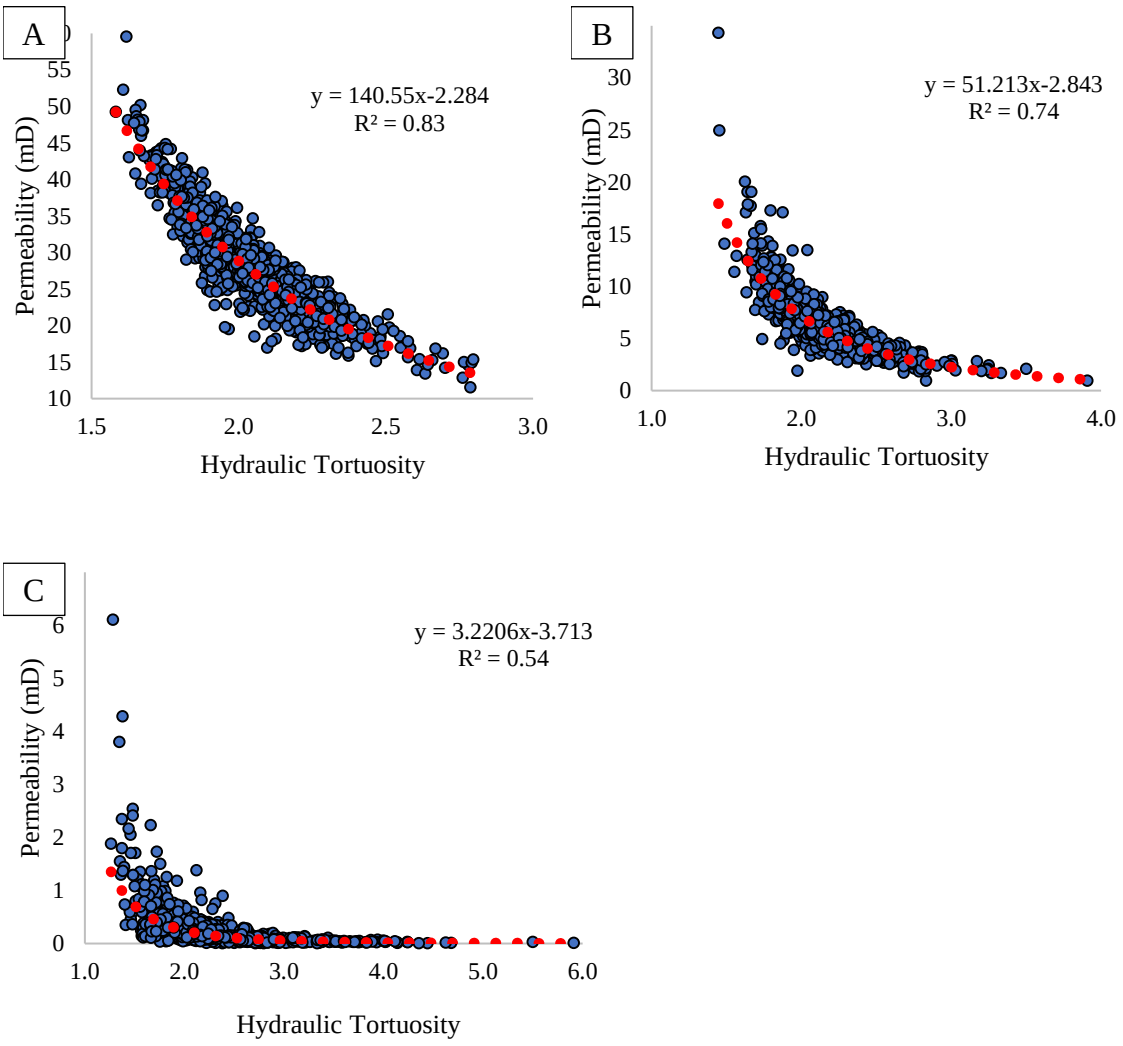

Fig. 2.9. Hydraulic tortuosity against permeability for A) group I, B) group II, and C) group III. The red dotted line is the best data fit which is power law.

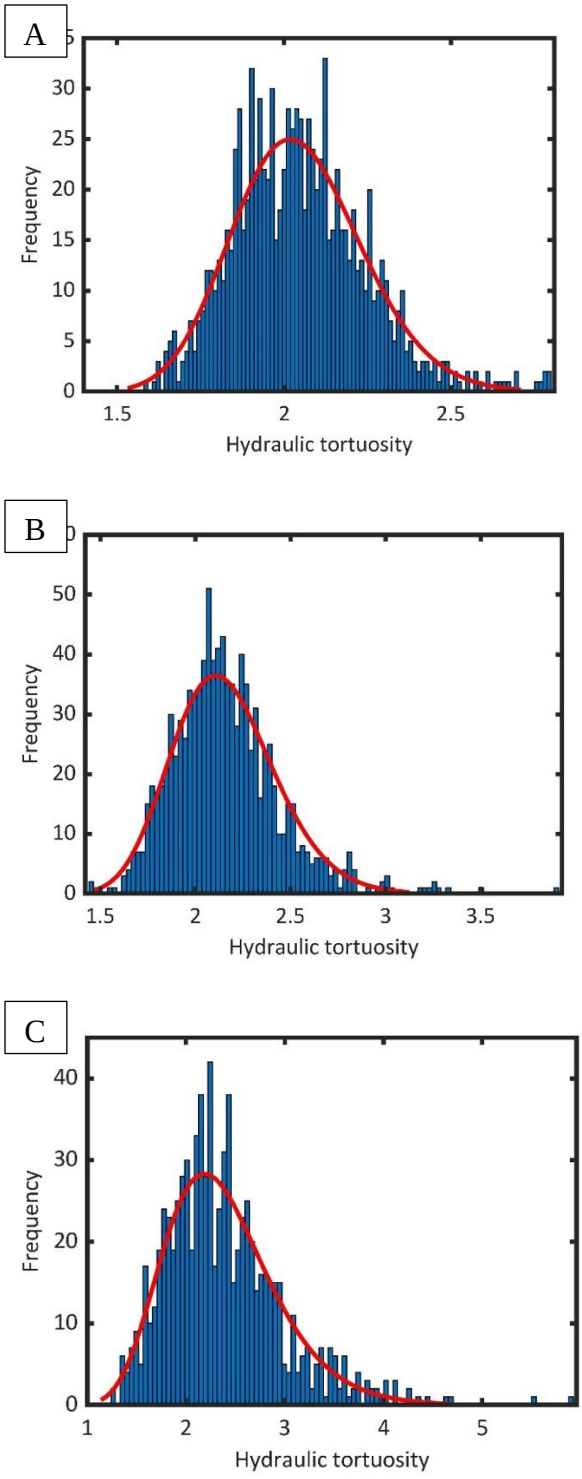

Fig. 2.10. A lognormal density function (red line) fitted on histograms of hydraulic tortuosity distribution for the stochastically generated 3D pore microstructures: (A) group I, (B) group II, and (C) group III.

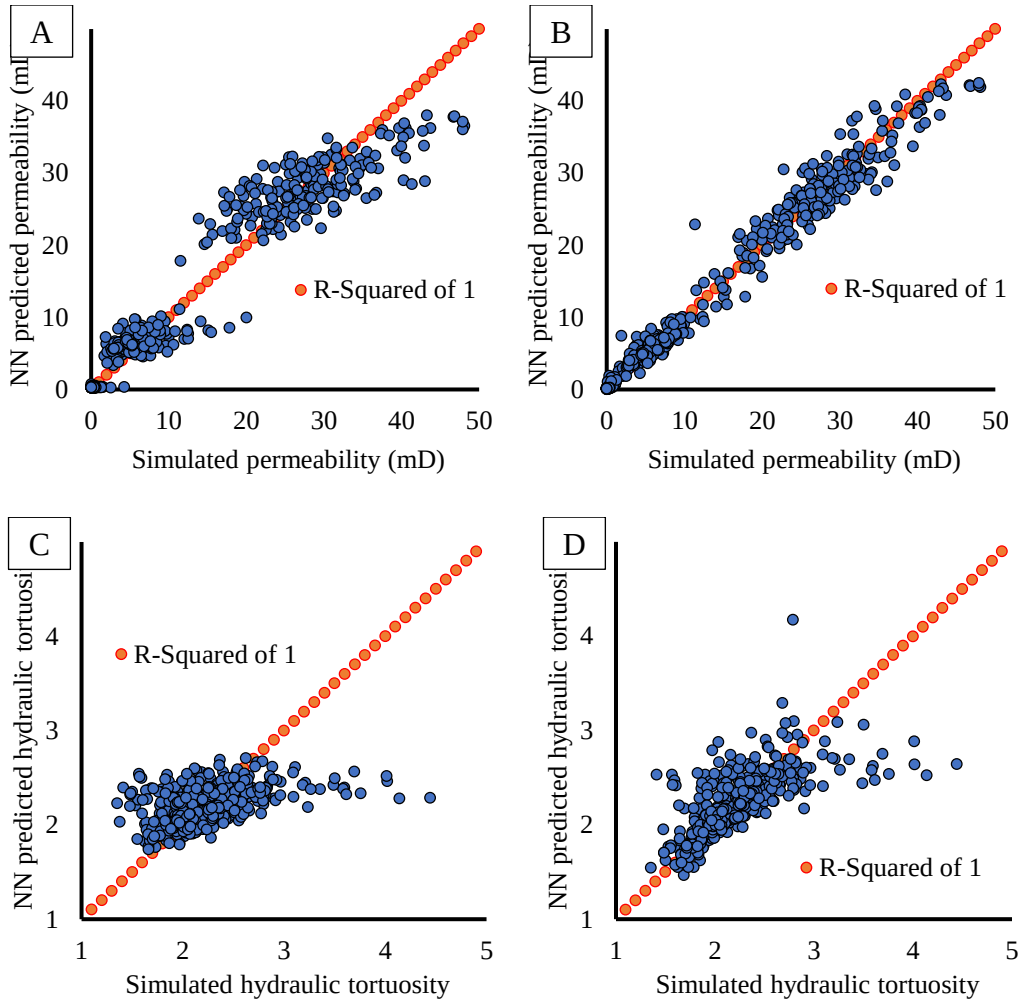

Fig. 2.11. Pore-scale simulations versus NN predictions of permeability and hydraulic tortuosity data. A) Permeability predictions made from surface are parameters (pS, bS), domain length scale, standard deviation of PTSD, and PTSD percentiles (1st, 10th, 25th, 50th, 75th, and 90th). B) Permeability predictions made with tortuosity added as a 11th parameter. C) Hydraulic tortuosity predictions made from pore microstructure parameters: pS, bS, domain length scale, standard deviation of PTSD, and PTSD percentiles (1st, 10th, 25th, 50th, 75th, and 90th). D) Hydraulic tortuosity predictions made with permeability added as a 11th parameter. The number of data point in each plot is 558.

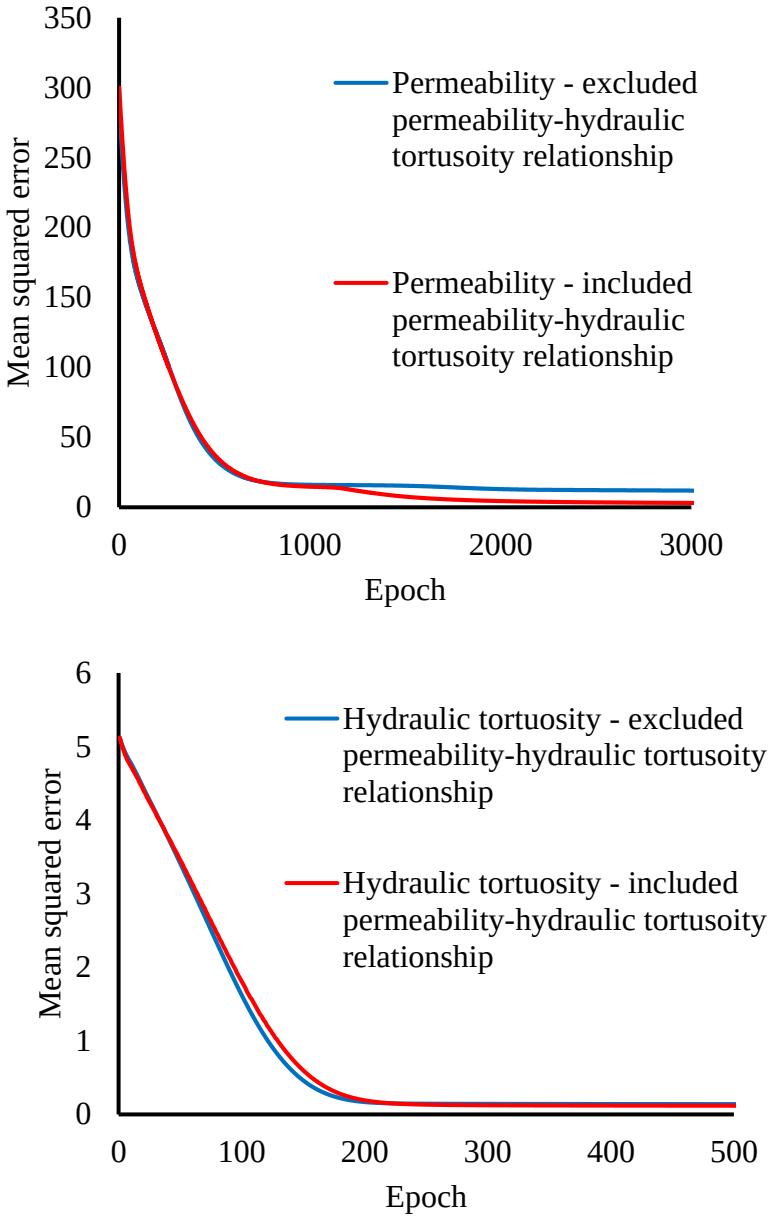

Fig. 2.12. Variation in MSE of validation data with epoch for A) the permeability NN model and B) the hydraulic tortuosity NN model.

Tables

Table 2.1. Statistical analysis of permeability.

Group	Mean pore size (μm)	Standard deviation of PSD (μm)	Mean Permeability (mD)	CV of Permeability	Skewness	Kurtosis
I	10	0	28.47	24%	0.57	3.59
II	10	5	6.39	44%	2.32	16.27
III	10	11	0.27	161%	6.24	62.97

Table 2.2. Statistical analysis of hydraulic tortuosity.

Group	Mean pore size (μm)	Standard deviation of PSD (μm)	Mean Hydraulic Tortuosity	CV of Hydraulic Tortuosity	Skewness	Kurtosis
I	10	0	2.05	10%	0.62	3.82
II	10	5	2.16	13%	1.05	5.93
III	10	11	2.38	25%	1.21	5.94

Supplementary information

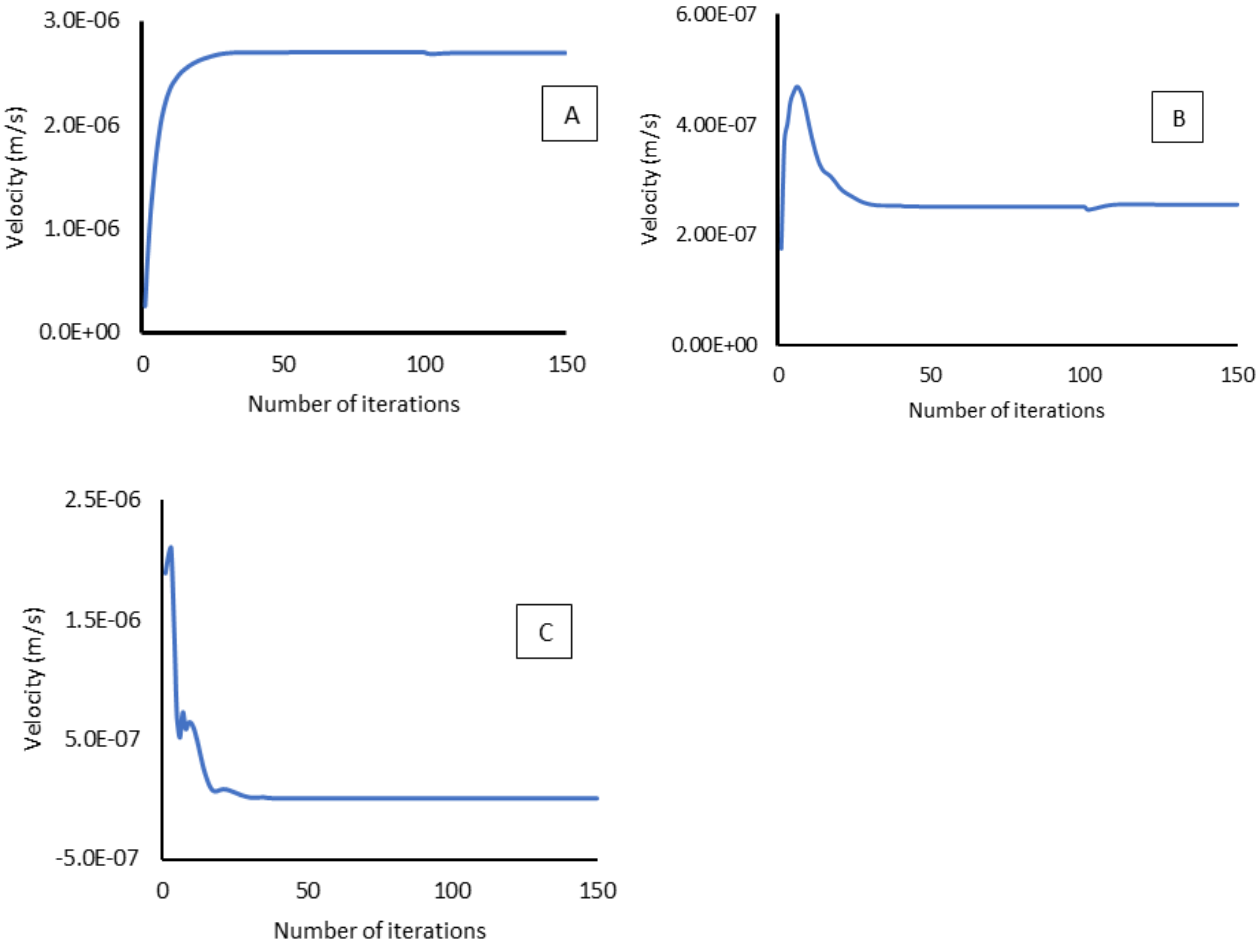

Fig. 2.1S. A-C showing the simulations were mesh independent for representative samples from group I, II, and III, respectively. The minimum mesh size for the first hundred iterations is 0.75 microns while the minimum mesh size was reduced 30% to 0.53 microns for the last 50 iterations.

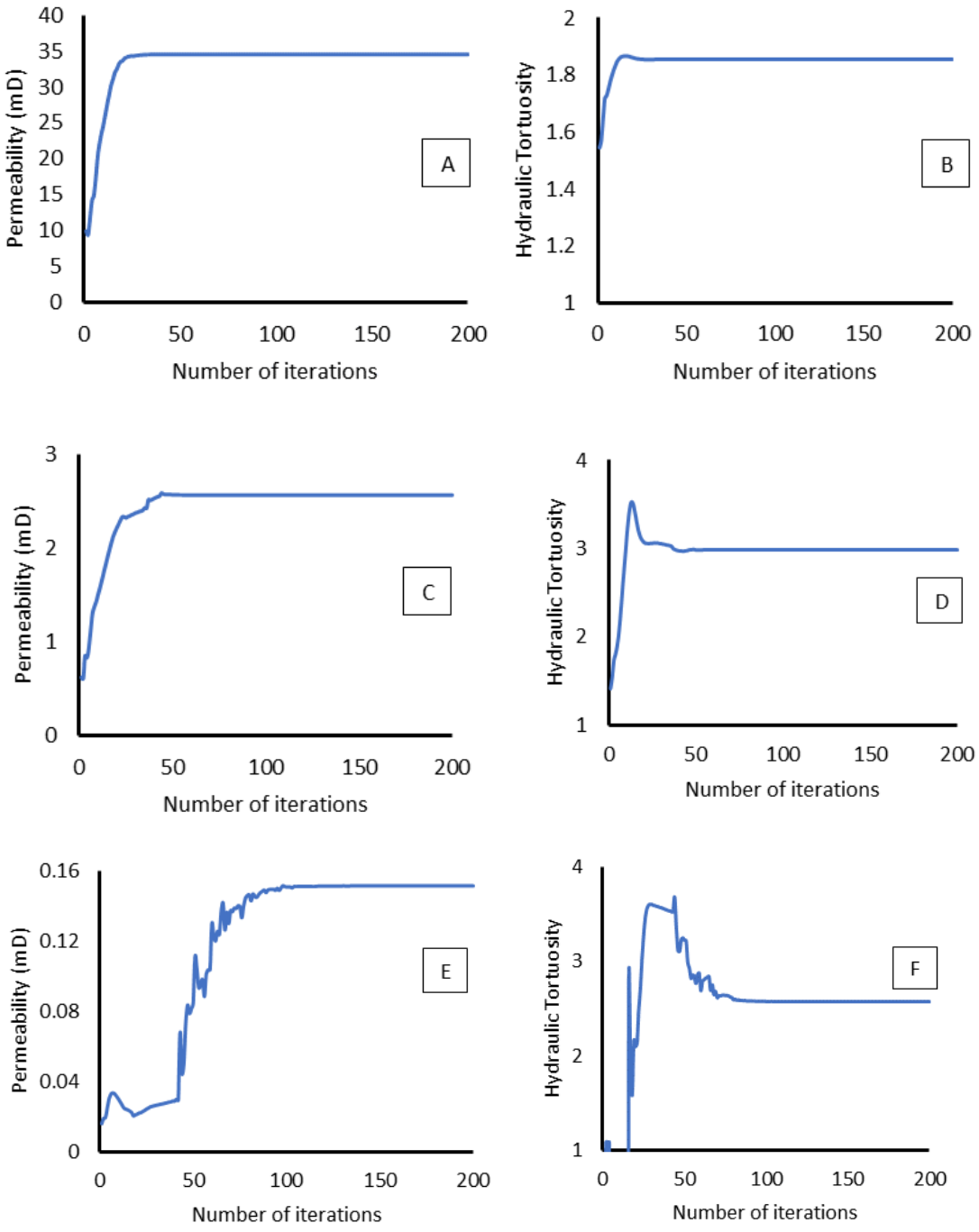

Fig. 2.2S. A-F showing that 200 iterations is sufficient for the permeability and hydraulic tortuosity to converge. A & B, C & D, and E & F are representative samples from group I, II, and III, respectively.

Table 2.1S. Correlation matrix for group I.

Parameters and Targets	Standard deviation of PTSD	PTSD Percentile						Domain Length Scale*	pS	bS	Hydraulic Tortuosity	Permeability
		1st	10th	25th	50th	75th	90th					
Standard deviation of PTSD	1.0	-0.3	-0.6	-0.5	-0.1	0.4	0.5	N/A	0.0	0.0	-0.1	0.0
PTSD: 1st percentile	-0.3	1.0	0.3	0.2	0.1	0.0	0.0	N/A	-0.1	-0.1	0.0	0.0
PTSD: 10th percentile	-0.6	0.3	1.0	0.6	0.3	0.2	0.1	N/A	-0.2	-0.3	0.0	0.1
PTSD: 25th percentile	-0.5	0.2	0.6	1.0	0.6	0.3	0.2	N/A	-0.2	-0.4	-0.1	0.2
PTSD: 50th percentile	-0.1	0.1	0.3	0.6	1.0	0.5	0.3	N/A	-0.3	-0.5	-0.1	0.2
PTSD: 75th percentile	0.4	0.0	0.2	0.3	0.5	1.0	0.5	N/A	-0.2	-0.4	-0.2	0.2
PTSD: 90th percentile	0.5	0.0	0.1	0.2	0.3	0.5	1.0	N/A	-0.1	-0.3	-0.1	0.1
Domain Length Scale*	N/A	N/A	N/A	N/A	N/A	N/A	N/A	N/A	N/A	N/A	N/A	N/A
pS	0.0	-0.1	-0.2	-0.2	-0.3	-0.2	-0.1	N/A	1.0	0.6	0.3	-0.3
bS	0.0	-0.1	-0.3	-0.4	-0.5	-0.4	-0.3	N/A	0.6	1.0	0.6	-0.6
Hydraulic Tortuosity	-0.1	0.0	0.0	-0.1	-0.1	-0.2	-0.1	N/A	0.3	0.6	1.0	-0.9
Permeability	0.0	0.0	0.1	0.2	0.2	0.2	0.1	N/A	-0.3	-0.6	-0.9	1.0

* Not applicable because the parameter was constant in this group

Table 2.2S. Correlation matrix for group II.

Parameters and Targets	Standard deviation of PTSD	PTSD Percentile						Domain Length Scale*	pS	bS	Hydraulic Tortuosity	Permeability
		1st	10th	25th	50th	75th	90th					
Standard deviation of PTSD	1.0	0.0	-0.1	0.0	0.0	0.3	0.5	N/A	0.0	0.0	0.1	-0.1
PTSD: 1st percentile	0.0	1.0	0.1	0.0	0.0	0.0	0.0	N/A	0.0	0.0	0.1	0.0
PTSD: 10th percentile	-0.1	0.1	1.0	0.4	0.1	0.0	0.0	N/A	0.1	0.0	0.1	-0.1
PTSD: 25th percentile	0.0	0.0	0.4	1.0	0.4	0.2	0.1	N/A	0.1	0.1	0.2	-0.2
PTSD: 50th percentile	0.0	0.0	0.1	0.4	1.0	0.4	0.2	N/A	0.1	0.0	0.1	-0.1
PTSD: 75th percentile	0.3	0.0	0.0	0.2	0.4	1.0	0.4	N/A	0.1	0.0	0.1	-0.2
PTSD: 90th percentile	0.5	0.0	0.0	0.1	0.2	0.4	1.0	N/A	0.1	0.0	0.1	-0.1
Domain Length Scale*	N/A	N/A	N/A	N/A	N/A	N/A	N/A	N/A	N/A	N/A	N/A	N/A
pS	0.0	0.0	0.1	0.1	0.1	0.1	0.1	N/A	1.0	0.1	0.3	-0.3
bS	0.0	0.0	0.0	0.1	0.0	0.0	0.0	N/A	0.1	1.0	0.2	-0.3
Hydraulic Tortuosity	0.1	0.1	0.1	0.2	0.1	0.1	0.1	N/A	0.3	0.2	1.0	-0.8
Permeability	-0.1	0.0	-0.1	-0.2	-0.1	-0.2	-0.1	N/A	-0.3	-0.3	-0.8	1.0

* Not applicable because the parameter was constant in this group

Table 2.3S. Correlation matrix for group III.

Parameters and Targets	Standard deviation of PTSD	PTSD Percentile						Domain Length Scale*	pS	bS	Hydraulic Tortuosity	Permeability
		1st	10th	25th	50th	75th	90th					
Standard deviation of PTSD	1.0	0.0	-0.1	0.0	0.0	0.2	0.3	0.0	0.0	0.1	-0.1	0.1
PTSD: 1st percentile	0.0	1.0	0.1	0.0	-0.1	0.1	0.1	-0.1	0.0	0.1	0.1	0.0
PTSD: 10th percentile	-0.1	0.1	1.0	0.3	0.0	0.0	0.0	-0.1	0.1	0.0	0.1	-0.1
PTSD: 25th percentile	0.0	0.0	0.3	1.0	0.3	0.1	0.0	0.0	0.1	0.0	0.1	-0.1
PTSD: 50th percentile	0.0	-0.1	0.0	0.3	1.0	0.3	0.1	0.0	0.1	0.1	0.1	0.0
PTSD: 75th percentile	0.2	0.1	0.0	0.1	0.3	1.0	0.5	0.0	0.1	0.1	0.1	0.0
PTSD: 90th percentile	0.3	0.1	0.0	0.0	0.1	0.5	1.0	0.0	0.1	0.1	0.1	0.0
Domain Length Scale	0.0	-0.1	-0.1	0.0	0.0	0.0	0.0	1.0	0.0	0.0	0.0	0.0
pS	0.0	0.0	0.1	0.1	0.1	0.1	0.1	0.0	1.0	0.2	0.2	-0.2
bS	0.1	0.1	0.0	0.0	0.1	0.1	0.1	0.0	0.2	1.0	0.2	-0.2
Hydraulic Tortuosity	-0.1	0.1	0.1	0.1	0.1	0.1	0.1	0.0	0.2	0.2	1.0	-0.5
Permeability	0.1	0.0	-0.1	-0.1	0.0	0.0	0.0	0.0	-0.2	-0.2	-0.5	1.0

CHAPTER III

MACHINE LEARNING MODELING OF PERMEABILITY IN 3D HETEROGENEOUS POROUS MEDIA USING A NOVEL STOCHASTIC PORE-SCALE SIMULATION APPROACH.

3.1 Abstract

Accurate predictions of rock permeability is critical for resource exploration and environmental management. To improve on existing approaches to permeability prediction, this study employed a stochastic pore-scale simulation approach. The petrophysical properties needed for the implementation of this approach are porosity and pore size distribution (PSD) of rock samples which can be obtained easily from mercury injection capillary pressure measurements. The approach was tested on four carbonate and five siliciclastic rock cores. To consider a wide range of possible pore connectivity scenarios that can be associated to the same PSD and porosity, the employed stochastic pore-scale simulation approach involves the generation of hundreds of 3D pore micro-structures of the same PSD and porosity but different stochastic pore connectivity. Permeability is calculated by averaging the permeability distribution obtained from pore-scale flow simulations through the generated 3D pore microstructures. Permeability estimations were closer to measured permeability with this approach than with five deterministic empirical model equations. Machine learning was used to reduce the required

number of pore-scale simulations by 157 times and reproduced permeability estimated from pore-scale flow simulations with a mean absolute percentage error of 10%.

3.2 Introduction

Predictions of flow properties in heterogeneous porous media are highly problematic. In general, assessments of subsurface flow and reactive transport processes through rocks requires knowledge of permeability (Beisman et al., 2015; Harbaugh, 2005; Xu et al., 2006). Permeability is the ease of fluid flow through porous media (Friedman, 1976; Zhang, 2013). Fundamentally, permeability is a function of the pore microstructure of porous media (Algive et al., 2012; Chen et al., 2015; Cheng et al., 2019). True permeability of rocks is obtained through laboratory measurement from core plugs (rock samples) and pressure transient analysis of well test data (Mohebbi & Kaydani, 2015). In absence of true permeability measurements, permeability is traditionally estimated from model equations that relate permeability to other petrophysical rock properties. Kozeny (Kozeny, 1927; Ozgumus et al., 2014) proposed one of the foremost equations used in permeability estimations. The Kozeny equation is formed from the combination of Darcy's Law (Darcy, 1856), the Hagen-Poiseuille velocity equation (Sutera & Skalak, 1993), and the concept of tortuosity (Ghanbarian et al., 2013). Kozeny's equation is expressed mathematically as (Ozgumus et al., 2014):

$$K = \frac{\phi d^2}{\tau} \tag{3.1}$$

where K is the permeability, τ is the tortuosity defined as the ratio of actual length of flow path in the porous media to the length of flow path in the absence of porous media, d is the pore hydraulic diameter, and φ is the porosity of the porous media.

The equation was later modified into the Kozeny-Carman equation (Carman, 1937; Ozgumus et al., 2014). The Kozeny-Carman equation is given by (Ozgumus et al., 2014):

$$K = \frac{\phi d^2}{16\, K_k} \tag{3.2}$$

where Kk is the Kozeny constant which captures the effect of tortuosity, particle shape, and connectivity of pores.

The dependence of the Kozeny and Kozeny-Carman equations on tortuosity (Ozgumus et al., 2014) implies that it is not suited for making permeability prediction in heterogenous porous media. This is due to the deterioration of permeability-tortuosity at increased levels of heterogeneity (Ishola et al., 2022). Also, porosity, which is the key parameter in Kozeny-Carman equation (Carman, 1937; Ozgumus et al., 2014) is known to have poor correlation with permeability (Sun et al., 2017). Permeability have been shown to vary up to five orders of magnitude for a very narrow porosity range (Westphal et al., 2005). Pore size distribution of rocks is deemed to provide better estimation of permeability when combined with porosity (Westphal et al., 2005). This can be implemented using Nuclear Magnetic Resonance (NMR) T2 data through the Timur-Coates (TC) equation (Timur, 1968) and the Schlumberger-Doll-Research (SDR) equation (Kenyon, 1992). Westphal (Westphal et al., 2005) identified heterogeneity as a limitation

in the application of TC and SDR equations in carbonate rocks because they assume even distribution of pore connectivity and employ total porosity instead of effective porosity in their respective equations. Mercury injection capillary pressure (MICP) is another routine approach used to make permeability predictions using empirical models. Several authors have used percentage mercury saturation or geometric average of pore throat sizes as a parameter to predict permeability (Rahul Dastidar, Carl H Sondergeld, et al., 2007; Jairam Kamath, 1992; S. Kolodzie, 1980; Pittman, 1992; Purcell, 1949; B. Swanson, 1981; Wells & Amaefule, 1985). The use of MICP for permeability predictions is empirical and it depends heavily on the data distribution that are used in deriving the respective model equations. In general, empirical model equations are constrained by the data used in their derivations. This is a challenge for heterogeneous rocks such as carbonate rocks because pore connectivity in these rocks can vary significantly in space even within the same outcrop due to diagenesis (Choquette & Pray, 1970), leading to poor estimates of permeability.

Numerical approaches have been proposed and used to estimate permeability of rocks (Blunt et al., 2013; Vilcáez et al., 2017). The main advantage in the use of numerical approaches is the fact that it is not biased since it is dependent on fundamental governing equations of fluid flow (Chen & Doolen, 1998; Chorin, 1968). However, numerical approaches are dependent on the fidelity of the 3D microstructure image used to conducting flow simulation as well as its representative nature. Different approaches have been employed to construct 3D pore microstructures of rocks from either 2D SEM images or 3D X-ray micro-CT scan images (Blunt et al., 2013; Xiong et al., 2016). The construction of 3D pore microstructures from 2D SEM images has been done by packing

together irregular grains using statistical techniques (e.g., two-point, multiple- point, and simulated annealing) (Manwart et al., 2000; Okabe & Blunt, 2004). That said, 2D representations of pore microstructural features can vary significantly from their true 3D nature in heterogeneous rocks. The use of FIB-SEM image overcomes this challenge but is a very expensive and time-consuming procedure. Notably, FIB-SEM is extremely small and does not provide a representative distribution of pore microstructural features of rock samples (Blunt et al., 2013; Xiong et al., 2016). The use of 3D pore microstructures from 3D X-ray micro-CT solves this problem. Though, this technology has a typical resolution of about 1–50 μm which fails to capture smaller pores in rocks as well as pore connectivity (Xiong et al., 2016). For permeability calculations, numerical methods such as Navier Stokes (Chorin, 1968) and Lattice Boltzmann methods (Chen & Doolen, 1998) provide good estimates of permeability, however, it requires a lot of computational resources which makes its adoption less attractive. These encourages the use of pore network modeling which is less accurate in comparison (Tembely et al., 2020). This is due to over simplification of pore microstructures making permeability calculations faster and less computationally intensive (Tembely et al., 2020).

To reduce the time and cost of obtaining representative 3D pore microstructure images and conducting respective pore-scale flow simulations, we use machine learning (ML) models instead of pore-scale flow simulations to predict permeability. ML models in the approach is trained with permeability values obtained by a novel stochastic pore-scale simulation approach. The stochastic pore-scale simulation approach is detailed in our prior paper (Ishola et al., 2022). This approach entails generating 3D pore microstructures of the same porosity and pore size distribution (PSD) but stochastic pore connectivity.

Direct pore-scale simulations of permeability on the stochastically created 3D pore microstructures is used in obtaining the permeability distribution which is analyzed to determine the most probable permeability of a sample with a given porosity and PSD. Direct pore-scale simulations is a common approach to infer porous media properties using pore microstructure images (Kohanpur et al., 2022; Konangi et al., 2021).

In some cases, it might require thousands of stochastically generated 3D pore micro- structures to reach representative elementary values. For practicality, ML is used to reduce the computational cost of direct pore-scale simulations of permeability (Tembely et al., 2020). The use of ML in geoscience is routine and has been used in making permeability predictions at various scales (Al Khalifah et al., 2020; Erofeev et al., 2019; Graczyk & Matyka, 2020; Male et al., 2020). The features employed in these studies include salts mass concentrations, porosity, lithology, depth, density, grain size, sample color, sample images, formation factor, pore throat diameter, tortuosity, and specific surface area. Algorithms used included linear regression, decision tree, random forest, gradient boosting, support vector machines, and neural network. Different from previous approaches, our approach relies solely on the fundamental pore microstructural parameters as features while the target (permeability) is physics derived through direct pore-scale simulations through the Navier Stokes equation. A key advantage of our approach over existing ML approaches for pore-scale permeability predictions lies in the use of PSD of rocks instead of pore-scale images which existing models generally use as feature data (Graczyk & Matyka, 2020; Tembely et al., 2020; Tembely et al., 2021; J. Wu et al., 2018). This implies that the computational resources required by our ML approach is significantly lower since our feature data is a CSV file and not an image data that could be up to tens of

Gigabytes in size which requires large computer RAM and GPUs to run. Furthermore, the use of MICP data as in this study provides continuum scale pore size distribution in rocks at higher resolution compared to direct imaging techniques (Anovitz & Cole, 2015; Blunt et al., 2013; Xiong et al., 2016). The workflow introduced in this study is easy to implement given the ease of obtaining continuum scale porosity and PSD of rocks from nuclear magnetic resonance (NMR) and mercury injection capillary pressure (MICP) data.

3.3 Material and methods

3.3.1 Workflow

To test the proposed ML approach to predict permeability, nine core plugs were obtained. The description of the core plugs is shown in Fig. 3.1. Fig. 3.2 shows the general workflow of this study. The data required in implementing the workflow are PSD and porosity of a rock sample (Fig. 3.2A) which is used in generating 3D pore microstructures of the same PSD and porosity but different stochastic pore connectivity (Fig. 3.2B). Pore-scale flow simulations are conducted on the generated 3D pore microstructures (Fig. 3.2C) which provides a distribution of possible permeability values of the analysed core plug (Fig. 3.2D). The input data (porosity and PSD) and respective distribution of possible permeability values are used to train a ML model (Fig. 3.2E). It is noteworthy that the ML model could be trained with combined data of several rock samples. The permeability distribution obtained from pore-scale simulations was averaged to obtain the permeability for the respective core plug which was compared to measured values as wells as permeability obtained from known empirical model equations. The permeability of the

core plugs were obtained from standard laboratory procedures while porosity and PSD of the core plugs were obtained from their MICP data.

3.3.2 Permeability measurement

Permeability measurements was based on Darcy's law (Darcy, 1856) which can be expressed as:

$$K = \frac{Q \times \mu \times L}{A \times \Delta P} \tag{3.3}$$

where Q is the volumetric flowrate through the inlet or outlet in m^3/s, A is the cross-sectional area perpendicular to the flow at the respective boundary in m^2, K is the absolute permeability of the rock domain in m^2, ΔP is the pressure drop in the principal direction of the fluid in Pa, μ is the dynamic viscosity of the fluid in Pa-s, and L is the length along the direction of the pressure drop in meters. Calculated permeability was converted from m^2 to mD.

For pressure drop measurement, we used a Hassler Type core-holder (RCH-series of Core Laboratory) where water was injected into the core plugs through a 260 dual syringe pump (Teledyne ISCO). Flow rates varied from 0.025 to 0.5 mL/min. Confining pressure was applied to close the space between the core plug and the interior of the core holder to prevent flow of injected fluid around the core plug. Low flow rates were used to avoid flow channelling through the core plug and to ensure that the Reynolds number is very low ($lessthan 1 \times 10^{-4}$); enough for the application of Darcy's law to be valid for permeability calculation. A pressure transducer was used to measure the pressure at the

inlet while the outlet pressure is known to be atmospheric pressure. The pressure drop across the core plug was observed through time to detect when the system reaches a steady state condition. The experiment is deemed to reach steady state when the pressure drop becomes constant. L and A were measure on the respective core plugs, while the dynamic viscosity of the fluid (water) is known to be 8.90×10^{-4} Pa·s.

3.3.3 Pore size distribution (PSD) data

PSD data of the core plugs was obtained from MICP data (Fig. 3.3). MICP is routinely used to deduce PSD in rocks using the Washburn equation (Klobes et al., 1997; Li et al., 2018; Liu et al., 2019; Schmitt et al., 2013; Shen et al., 2021; Wang et al., 2019; Yao & Liu, 2012). To partially account for shadowing or ink-bottle phenomenon in MICP data (Basan et al., 1997; Xiong et al., 2016), a cut off is applied to the MICP distribution. The cut off is applied at the minimum incremental pore volume (MIPV). The MIPV (Fig. 3.3) is coined in this study as pore size where the incremental porosity abruptly drops before attaining 100 % mercury saturation. A cut off is applied at MIPV because the pressure to get to the pores beyond this point is already very high; hence the entire pore system unsaturated at this point is erroneously captured as tiny pores (Basan et al., 1997; Xiong et al., 2016). Furthermore, the low magnitude of incremental volume at the MIPV can be interpreted as a semi-isolated pore system which might contribute to the overall flow through the core plug. In absence of accurate data for this region, we assume that the region has the same pore size distribution as the remainder of the core plug. It is noteworthy, that the applied cut-off also discards tiny pores in the core plugs. In this study, the pore geometry is simplified to a sphere. Data provided from MICP analysis of core

plugs is a plot of pore radius against incremental pore volume (Fig. 3.3). To obtain the pore population of the core plugs, the incremental pore volume is divided by the corresponding volume of a single pore (Eq. (3.4)). Pore population was normalized (Eq. (3.5)) to ease comparison among the core plugs (Fig. 3.5).

$$P = \frac{P_v}{\frac{4}{3}\pi r^3} \tag{3.4}$$

$$P_p = \frac{P}{\sum P} \tag{3.5}$$

where P_V is the incremental pore volume from MICP data, r is the corresponding pore radius, $\sum P$ is the total number of pores in the analysed core plug, P is the number of pores of certain pore radius, and P_p is the normalized pore size distribution.

Fig. 3.4 shows the PSD of all the core plugs to have lognormal distribution. Our core plugs include unimodal (Core plug A-H) and bimodal (Core plug I) PSD to test the versatility of the workflow. The MICP analysis also provided porosity ($\emptyset_m$). It's important to note the porosity provided by MICP is effective porosity given that all the pores must be accessible by injected mercury.

3.3.4 Stochastic generation of 3D pore microstructures

The stochastic generation of 3D pore microstructures (Fig. 3.5) follows the workflow employed by Ishola et al., 2022 (Ishola et al., 2022) where pore size distribution, effective porosity, and a spherical pore geometry were used to create multiple realizations of 3D pore microstructures of the same effective porosity, PSD, and pore shape while

stochastically connecting the pores. The fixed effective porosity, PSD, pore frequency, and pore shape helps consider the effect of a wide range of possible pore connectivity scenario in each core plug (Ishola et al., 2022). This is vital because pore connectivity cannot be accurately deduced in a representative core plug despite been a key control on permeability (Ishola et al., 2022). For each core plug, the number of stochastically generated 3D pore microstructures varied from 845 to 933. In total, 8,123 pore microstructures were generated across the nine core plugs. Summary data of the pore microstructures can be found in the supplementary information (Table 3.1S and 3.2S). Full details on the stochastic generation of 3D pore microstructures and precautions taken to ensure the representative nature of the pore microstructural parameters is detailed in our preceding publication (Ishola et al., 2022).

3.3.5 Pore-scale simulations

Pore-scale simulations of flow (Fig. 3.6) through the stochastically generated 3D pore microstructures is executed with STAR-CCM+® computational fluid dynamics software, using its finite volume methodology to solve the mass continuity equation (Ishola et al., 2022):

$$\vec{\nabla} \cdot \rho\vec{V} + \frac{\partial \rho}{\partial t} = 0 \tag{3.6}$$

and Navier-Stokes momentum equation:

$$\frac{\partial \vec{V}}{\partial t} + \left(\vec{V} \cdot \vec{\nabla}\right)\vec{V} = -\frac{1}{\rho}\vec{\nabla}P + v\vec{\nabla}^2\vec{V} \tag{3.7}$$

where ρ is density of the fluid, v is kinematic viscosity, P is pressure, t is time, and $\vec{V}$ is fluid velocity.

This software has been successfully used for flow simulations in similar 3D pore microstructures and has been proven effective in simulating pore-scale flow and solute transport process (Oostrom et al., 2014; Yang et al., 2016; Yang et al., 2013). The implementation of pore-scale simulation in this study also follows the workflow used by Ishola et al., 2022 (Ishola et al., 2022) with the only difference being that the minimum cell size of the mesh was lowered to 0.375 μm from 0.75 μm to provide higher level of detail in the flow domain. The average number of cells across generated 3D pore microstructures is 1 million and the computational time per simulation is about 11 min. We employed Oklahoma State University's Pete supercomputing facilities (32 cores and 96 GB of RAM for each run) to execute the numerical portion of this study.

3.3.6 Permeability calculation

Numerical simulation of flow through each 3D pore microstructure at a Reynold number less than 0.0001 makes permeability estimation possible through Darcy's equation (Eq. (3)) (Chen et al., 2015; Darcy, 1856; Vilcáez et al., 2017) and is rewritten as (Darcy, 1856):

$$K = \frac{M \times \mu \times L}{\Delta P \times A \times \rho} \tag{3.8}$$

where K is the absolute permeability of the rock domain in m^2, ΔP is the pressure drop in the principal direction of the fluid in Pa, μ is the dynamic viscosity of the fluid in Pa-s, M is the mass flowrate through the inlet or outlet in kg/s, ρ is the density of the fluid flowing through the medium in kg/m^3, A is the cross-sectional area perpendicular to the flow at the

respective boundary in m^2, and *L* is the length along the direction of the pressure drop in meters.

Since properties of the fluid (density and viscosity of water) and pressure drop are constant, permeability is calculated from changes in mass flow rate and length scale (L^{-1}) of the 3D pore microstructure (Darcy, 1856). Calculated permeability was converted from m^2 to mD.

3.3.7 Machine learning implementation

Several ML algorithms were trained with pore microstructural parameters obtained from the generated 3D pore microstructures as features and corresponding permeability estimated from pore-scale simulations as the target. For ML implementation, the entire data set—permeability estimated from pore-scale flow simulations of all 3D pore micro structures generated for the nine core plugs—was randomized, and split into training and test set in ratio 7:3. The pore micro- structural parameters (features) used for ML implementation are the average pore-throat size, standard deviation of pore-throat size distribution (PTSD), 1st percentile of PTSD, 5th percentile of PTSD, 10th percentile of PTSD, 25th percentile of PTSD, 50th percentile of PTSD, 75th percentile of PTSD, 90th percentile of PSD, 99th percentile of PTSD, porosity, domain size of the pore microstructure, number of pores connected to the inlet (conin) and outlet (conout) flow faces of the pore microstructure, and minimum of conin and conout of the respective pore microstructures. The last three features are introduced in this study, and they are deemed

to capture pore connectively as they quantify the true number of alternative paths for a particle to from inlet to outlet. The target in this study is permeability.

The ML algorithms considered in this study are Linear Regression, Random Forest, Support Vector Machine, Gradient Boosting, and Artificial Neural Network (Verdhan, 2020). The algorithm with the best performance in our test is the Gradient Boosting (GB) algorithm based on mean absolute percentage error (De Myttenaere et al., 2016) between permeability obtained from the direct pore-scale simulations and permeability obtained from respective ML algorithms. Hence, only the parameters related to GB modelling are mentioned in this paper. A summary on the implementation of the remaining five ML algorithms and their relative performance is in the supplementary information (Fig. 3.1S and Table 3.3S). In the pre-processing stage of the data for machine learning deployment, the data was standardized to account for the scale difference in the features (Mohamad & Usman, 2013; Pedregosa et al., 2011). In this study, the data was standardized by:

$$s = \frac{x - \bar{x}}{\sigma} \tag{3.9}$$

where s is the value after standardization, x is the original value of feature, x is the feature average, and σ is the standard deviation of the features. Hence, all the features have a mean of zero and a standard deviation of one.

GB was implemented on Scikit-learn (Pedregosa et al., 2011). The maximum depth in the GB algorithm was varied between 3 and 10 while the number of estimators was varied from 10 to 1000. The learning rate used in this study ranged from 0.0001 to 1 with other parameters in the GB algorithm kept at default. GridSearchCV (Pedregosa et al., 2011)

was used to select the best combination of maximum depth and number of estimators. The GB model was trained with data from all nine core plugs and combination of hyperparameters was selected based on a five-fold cross validation. In the second phase of GB deployment, the number of training data was systematically reduced from 100% to 0.5% to test the minimum number of training data required to make relatively good permeability predictions. It's worth highlighting that the test data remained constant for objective comparison.

3.3.8 Statistical comparison of results

The permeability of each core plug was estimated by averaging the permeability of the 3D pore microstructures that were stochastically generated from the PSD and porosity data (Fig. 3.4) (Cardwell & Parsons, 1945; Farquharson & Wadsworth, 2018; Warren & Price, 1961). The permeability of each core plug estimated using this method was compared against permeability estimated using five notable model equations through the mean absolute percentage error (MAPE) (De Myttenaere et al., 2016). MAPE is the average of the absolute percentage error between measured permeability and estimated permeability for n pore plugs. It can be expressed as:

$$MAPE = \frac{1}{n}\sum_{i=1}^{n}\left|\frac{k_{m,i}-k_{e,i}}{k_{m,i}}\right| \times 100 \quad (3.10)$$

where $k_{m,i}$, and $k_{e,i}$ is the measured permeability and estimated permeability of core plug i, while n is the total number of core plugs.

MAPE was used in this study because it takes magnitude of the measured permeability into account, hence, an objective comparison across different scales can be made.

3.3.9 Previous approaches to permeability estimation

For comparison with the approach used in this study, permeability was estimated for all nine core plugs using five notable model equations that employ MICP data. This include Winland (S. Kolodzie, 1980), Swanson (B. Swanson, 1981), Wells-Amaefule (Wells & Amaefule, 1985), Kamath (Jairam Kamath, 1992), and Dastidar models (Rahul Dastidar, Carl H Sondergeld, et al., 2007). The respective equations are given by:

$$k_{Winland} = 49.4 * R_{35}^{1.7} * \emptyset^{1.47} \quad (3.11)$$

$$k_{Swanson\text{-}brine} = 355 * \left[\frac{s_b}{P_C}\right]_A^{2.005} \quad (3.12)$$

$$k_{Wells\text{-}Amaefule} = 30.5 * \left[\frac{s_b}{P_C}\right]_A^{1.56} \quad (3.13)$$

$$k_{Kamath} = 347 * \left[\frac{s_b}{P_C}\right]_A^{1.60} \quad (3.14)$$

$$k_{Dastidar} = 4073 * R_{wgm}^{1.64} * \emptyset^{3.06} \quad (3.15)$$

where s_b is the percent bulk volume occupied by mercury, PC is the mercury capillary pressure (Psia), A is the maximum amplitude, $R35$ is 35% mercury saturation of pore volume, $\emptyset$ is porosity (fraction), and R_{wgm} is the geometric mean of pore sizes. Eqs. (3.11) - (3.14) are dependent on the empirical correlation between a critical pore throat sizes where mercury infiltration is deemed to connect the entire pore system of rock sample while Eq. (3.15) considered the size of all the pore throat sizes that are in a rock sample by taking their geometric mean.

3.4 Results and discussion

3.4.1 Stochastic pore-scale simulations of permeability

Direct pore-scale simulations of permeability for the 3D pore microstructures stochastically generated from the PSD curves (Fig. 3.4) yield a distribution of possible permeability values for the respective core plug (Fig. 3.7). The permeability for each core plug is calculated via arithmetic mean of possible permeability values. In comparison to existing deterministic model equations attempted in this study (Tables 3.1 and 3.2), computed permeability for the core plugs is generally closer to measured permeability of the respective core plug. Table 3.1 shows the relative rank of all the methods based on MAPE for the nine core plugs used in this study. The Wells-Amaefule model (Wells & Amaefule, 1985) ranks second place after our approach and is the only other approach with an MAPE less than 100%. Wells-Amaefule model is only an expansion of the empirical correlation introduced by Swanson (B. Swanson, 1981) to include tight rocks with permeability as low as 0.00002 mD (Comisky et al., 2007). That said, the maximum permeability in the empirical correlation by Wells-Amaefule is 70 mD which is within a reasonable range compared to the permeability data used in our study (Fig. 3.1 and Table 3.3). It also implies that the Wells-Amaefule model might not work well with higher permeability data since the empirical model is fitted to a narrow permeability data range. That said, the permeability data density is relatively high compared to the other empirical model equations implemented in this study (Table 3.3). it is important to note that the permeability data used in the Wells-Amaefule model is gas permeability. However, the authors argued that it is on the same order of magnitude as Klinkenberg corrected and

liquid permeability given the conditions under which the values are obtained (Wells & Amaefule, 1985). In third place of MAPE ranking is the Dastidar model (Rahul Dastidar, Carl H Sondergeld, et al., 2007).

The Dastidar model (Rahul Dastidar, Carl H Sondergeld, et al., 2007) is fundamentally different from the other empirical model equations considered in this study. As show in Eq. (3.15), it takes the entire pore size distribution into account by using their geometric mean. In contrast, the other four model equations (Eqs. 3.11–3.14) use a threshold in mercury saturation through the rock samples. However, the MAPE of permeability obtained using the Dastidar model was 573%, which is relatively high. This could be due to three reasons: 1) The Dastidar model gives more weight to porosity than the average pore-throat size (Eq. (3.15)). Hence, porosity is the controlling parameter in this model. Porosity is known to have a relatively poor relationship with permeability (Westphal et al., 2005). 2) The weights used in Dastidar model (Eq. (3.15)) is derived from incremental porosity (Comisky et al., 2007; Rahul Dastidar, Carl H Sondergeld, et al., 2007) and not the pore populations. We believe pore population better reflects true frequency of pores in a rock sample. 3) The permeability data density used in developing the Dastidar model is relatively low (Table 3.3). The Winland approach (S. Kolodzie, 1980) ranks 4th place in this study with an MAPE of 676%. The performance of this model could be due to the inclusion of uncorrected air permeability in modelling which is known to overestimate permeability (Comisky et al., 2007). 240 of the 322 permeability data points used in developing the Winland model are uncorrected air permeability (Table 3.3). The Swanson-brine model (B. Swanson, 1981) ranked 5 out of the 6 methods in this study. The Swanson-brine model (B. Swanson, 1981) was established with permeability ranging

from 0.02 mD to 1000 mD, however, the permeability data density is low (Table 3.3). Given that the main difference between Wells-Amaefule model (Wells & Amaefule, 1985) and the Swanson- brine model (B. Swanson, 1981) is a significant reduction in permeability data density in Swanson- brine model (B. Swanson, 1981) (Table 3.3), we can conclude that this is responsible for the drop off in MAPE from 67% in Wells-Amaefule model (Wells & Amaefule, 1985) to 821% in Swanson-brine model (B. Swanson, 1981). It is noteworthy that permeability range used to establish the Wells-Amaefule model equation (Wells & Amaefule, 1985) (Table 3.3) is concentrated within the permeability data range of this study (Fig. 3.1) which might also influence the performance of Wells-Amaefule model (Wells & Amaefule, 1985). This underlines a pitfall in the use of empirical model equations because it is usually suited to the data distribution from which it was derived and can be unreliable when the permeability data density is poor. Kamath model (Jairam Kamath, 1992) ranked 6 out of 6 in in approaches tested in the study with a MAPE of 914%. Considering that permeability prediction is consistently overestimated across all core plugs (Table 3.1), it is plausible that the performance is driven by the datasets used in the study. Based on the relative performance of the model equations used in this study, we can conclude that, empirical permeability model equations are adversely impacted by permeability data density, the use of uncorrected air permeability, reliance on porosity as the key parameter, and the distribution of permeability data used in fitting the relationship. The use of the stochastic pore-scale simulation approach (Ishola et al., 2022) overcomes these limitations because it mimics mechanistic processes that occur in rocks through the governing equation of fluid flow,

and it considers different pore connectivity scenarios that can result in the same PSD and porosity.

3.4.2 Computational reduction with machine learning

Fig. 3.8 shows only a 10% difference between the permeability values computed from pore-scale flow simulations and a GB model trained with pore microstructural parameters (features) of 28 pore microstructures. It is worth noting that the total number of pore microstructures required to obtain a representative permeability value from pore-scale flow simulations across the nine core plugs employed in this study is ~4400 (Fig. 3.9). This implies that the time required to obtain representative permeability prediction across the core plugs is reduced from 34 days (4,400 3D pore microstructures) to 6 h (28 3D pore microstructures). If a pretrained GB model is available, permeability predictions will take less than a second on a 16 GB RAM computer. Fig. 3.8 also shows that permeability predictions do improve with the size of training permeability data. Therefore, there is need for trade-off between available computing resources and accuracy the GB model. That said, Fig. 3.10 shows 28 pore microstructures to be sufficient (green data points) as it is close to a perfect prediction (orange data points). However, if the objective is to replicate representative permeability values computed from pore-scale flow simulations with near perfection, a larger number of training permeability data is beneficial. It is worth nothing that the only information needed to implement this ML approach is porosity and PSD which can be obtained from X-ray imaging methods, MICP, and NMR data.

3.5 Conclusions

In this study we have employed a stochastic pore-scale simulation approach to predict the permeability of nine core plugs of both carbonate and siliciclastic sources. Our stochastic pore-scale simulation approach is more accurate in predicting permeability compared to five notable deterministic model equations attempted in this study. To reduce the computational cost of predicting permeability by our stochastic pore-scale simulation approach, we used Gradient Boosting algorithm. This ML approach reduces the number of simulations needed to obtain representative permeability of all nine core plugs from 4,400 to 28, significantly reducing required computational resources and time. There are at least three key applications for our results: 1) a pretrained ML model using our approach can be incorporated with NMR information obtained while drilling to provide permeability information of penetrated formations, instantaneously; 2) a pretrained ML model using our approach could provide a simple tool to make quick assessments of rock samples before full laboratory experiments are applied to get true permeability of core plugs; and 3) the approach used in this study can help improve the performance and accuracy of fluid flow and reactive transport simulation computer programs. In general, the result of this study is beneficial in resource exploration as well as environmental protection and management.

Acknowledgements

This material is based upon work supported by the National Science Foundation under Grant HS-2041648. We appreciate the Association of Petroleum Geologist Foundation (AAPG), Oklahoma Geological Foundation (OGF), and the Oklahoma City Section of Society of Petroleum Engineers (SPE) for partial financial support of the Ph.D. research

of the first author. This is Oklahoma State University Boone Pickens School of Geology contribution number 2022- 130. Some of the computing for this project was performed at the High- Performance Computing Center at Oklahoma State University (OSU).

Figures

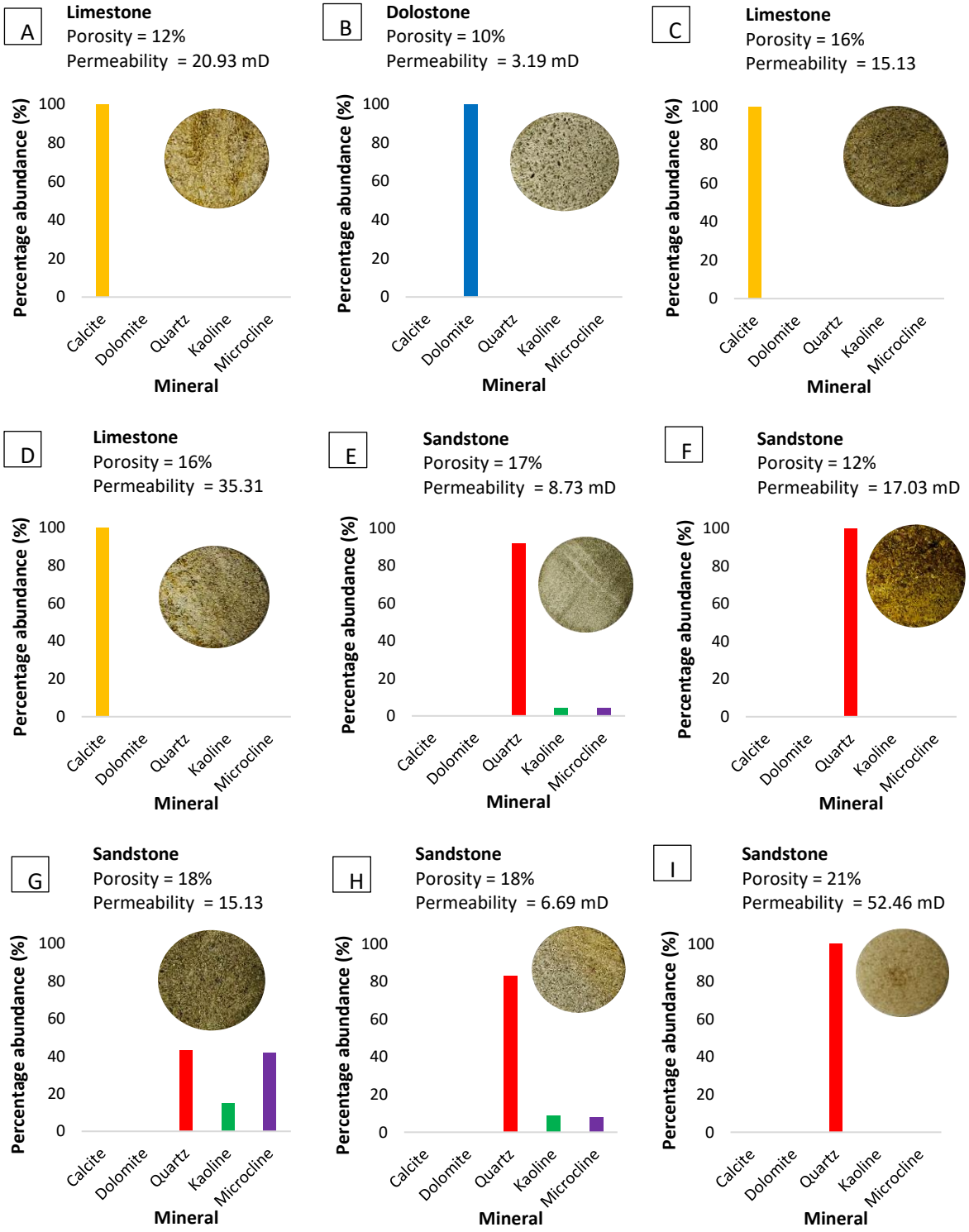

Fig. 3.1. Mineralogical composition of the core plugs employed in this study and their measured petrophysical properties.

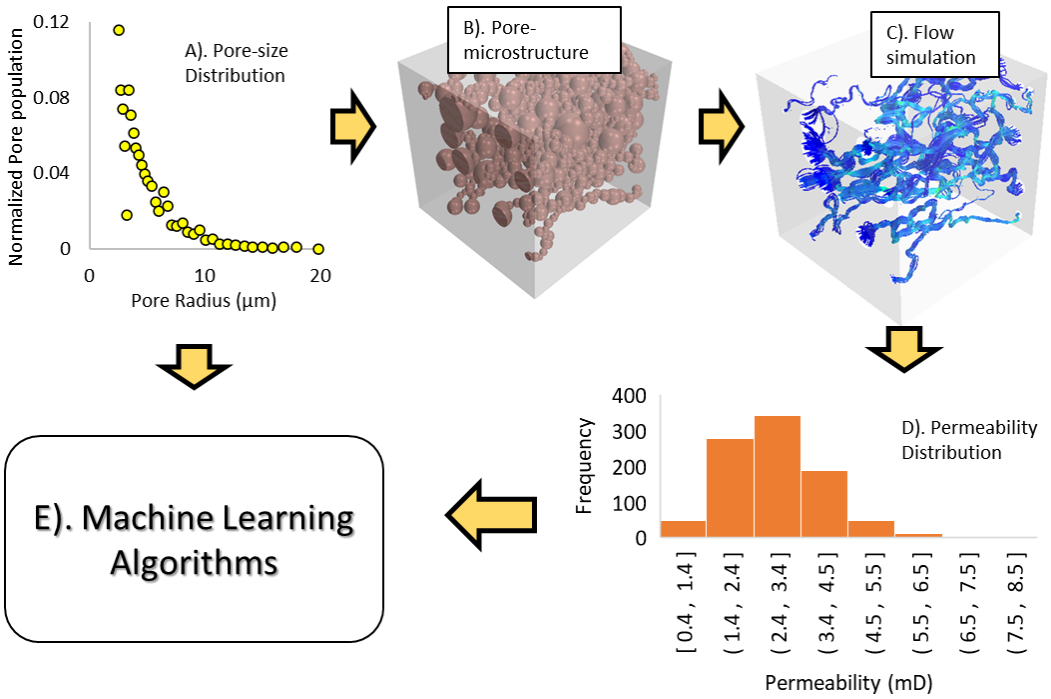

Fig. 3.2. Workflow of permeability prediction

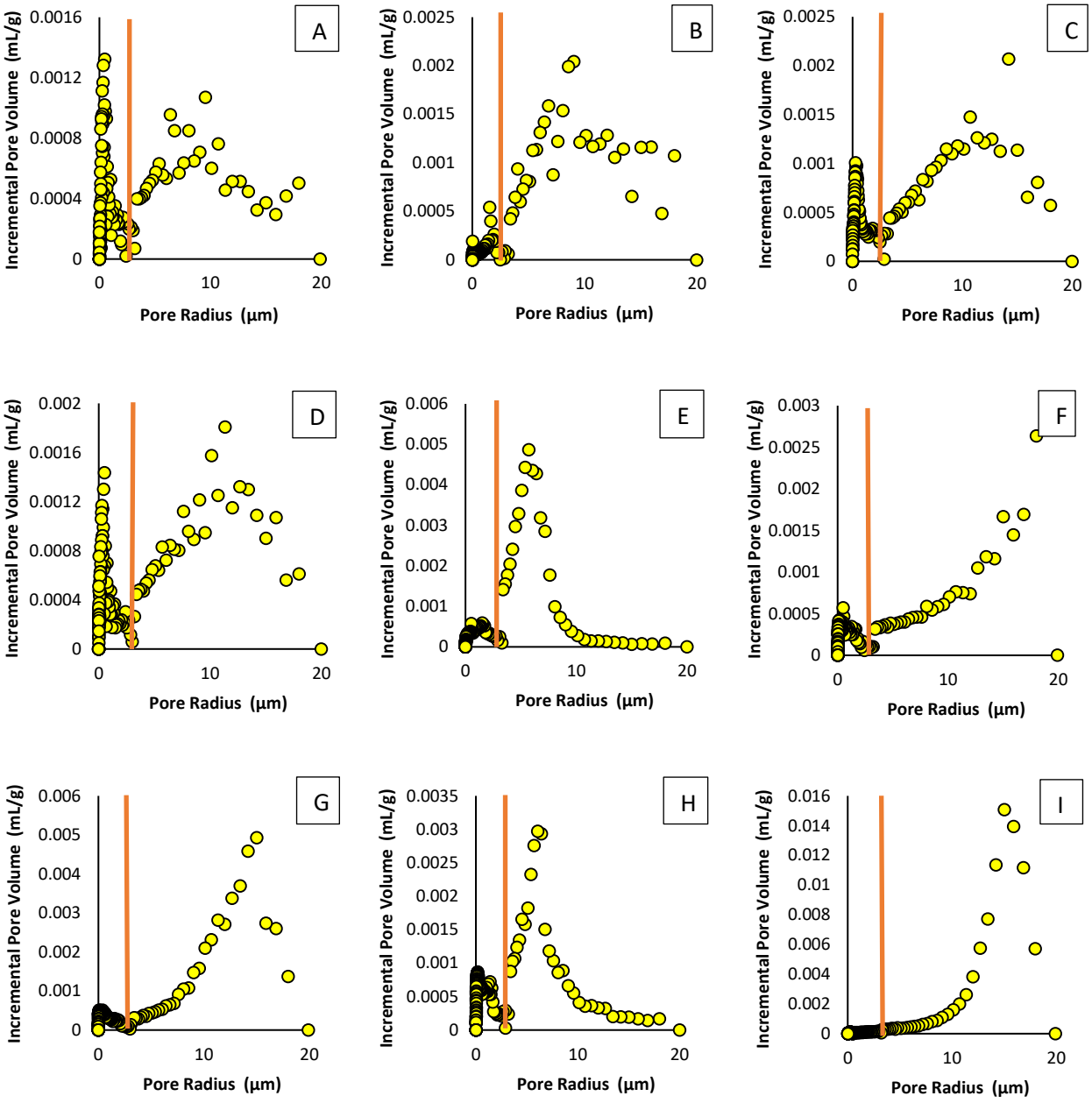

Fig. 3.3. MICP data of pore radius against incremental pore volume for all core plugs used in this study (Fig. 3.1).

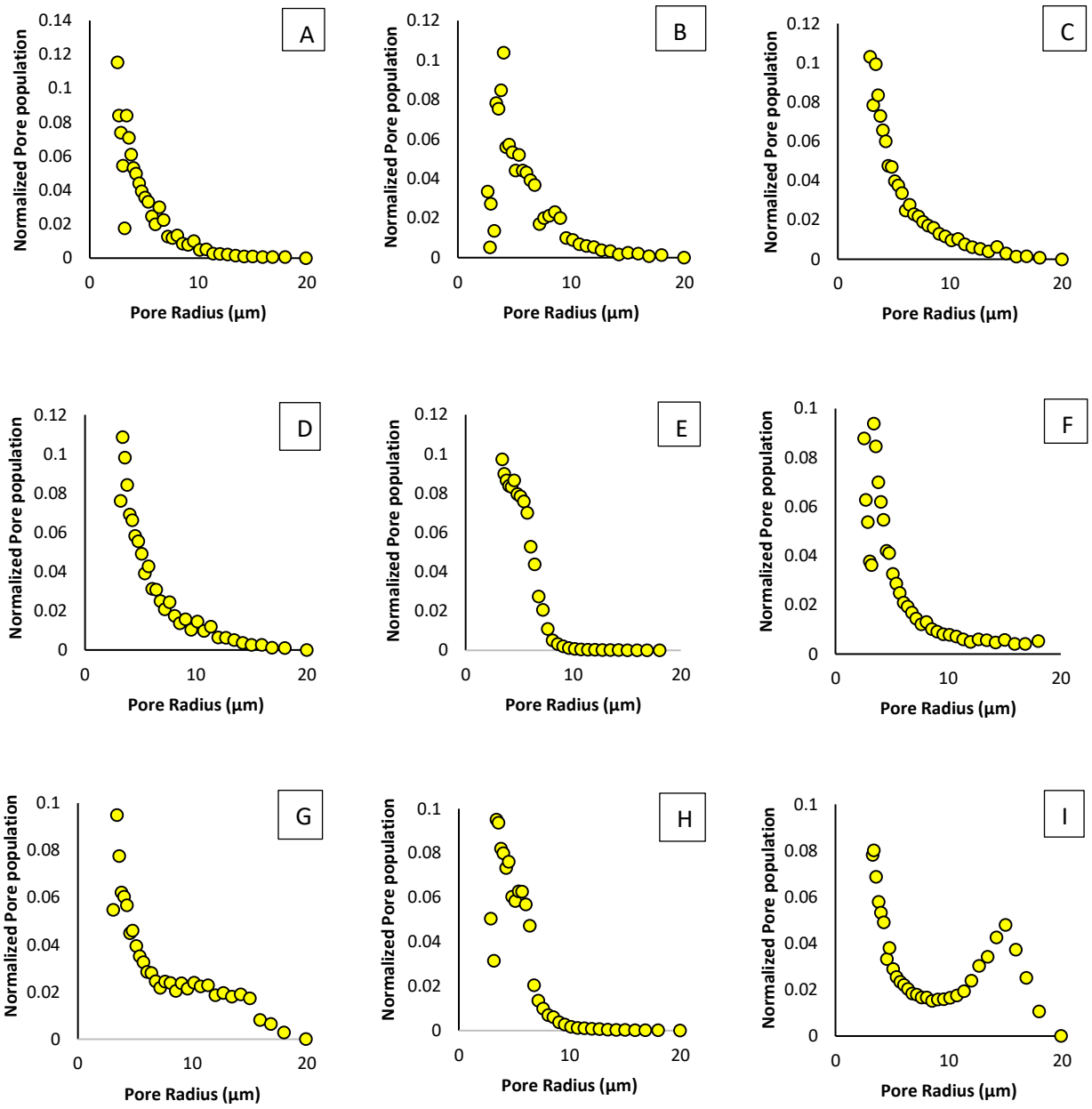

Fig. 3.4. MICP data plot of pore radius against normalized pore population for all core plugs used in this study (see Fig. 3.1).

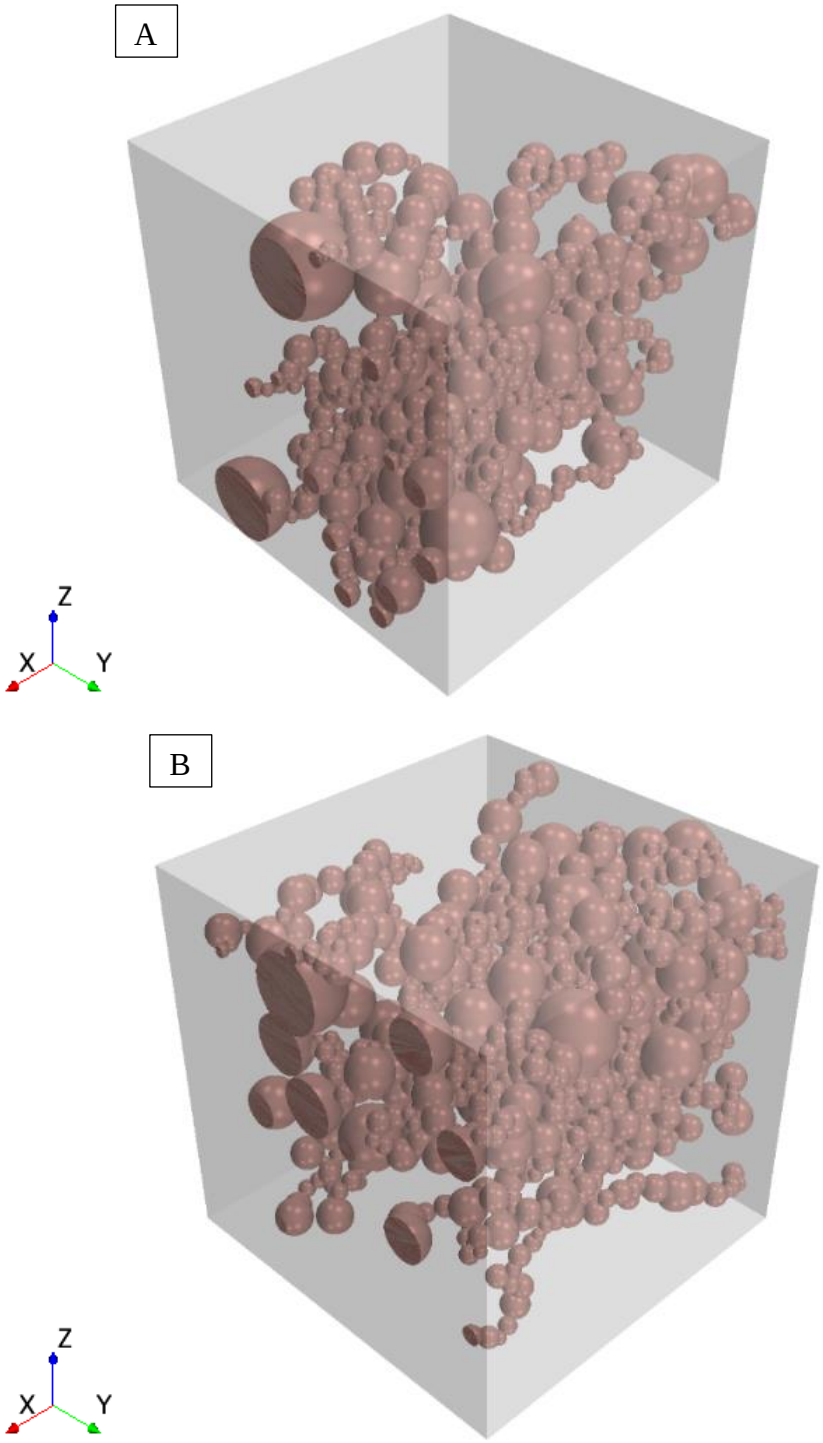

Fig. 3.5. Representative stochastically generated 3D pore microstructures showing different possible pore connectivity (brown) scenarios in core plug A (Fig. 3.1).

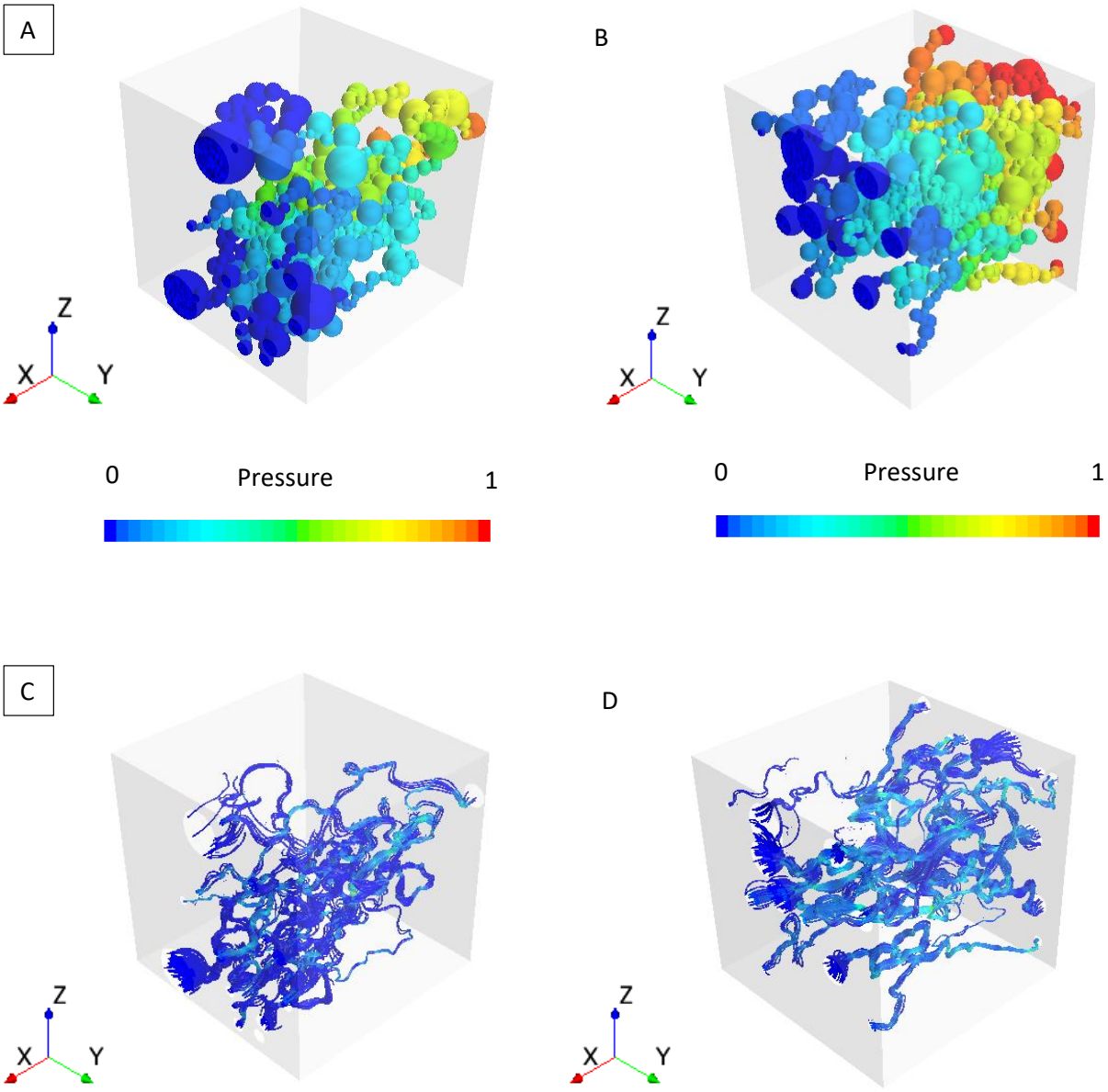

Fig. 3.6. Representative pressure distribution (A and B) and corresponding streamlines (C and D) through stochastically generated pore microstructures from PSD data (Figs. 3.4.A and 3.4.B). Flow is in the positive-X direction.

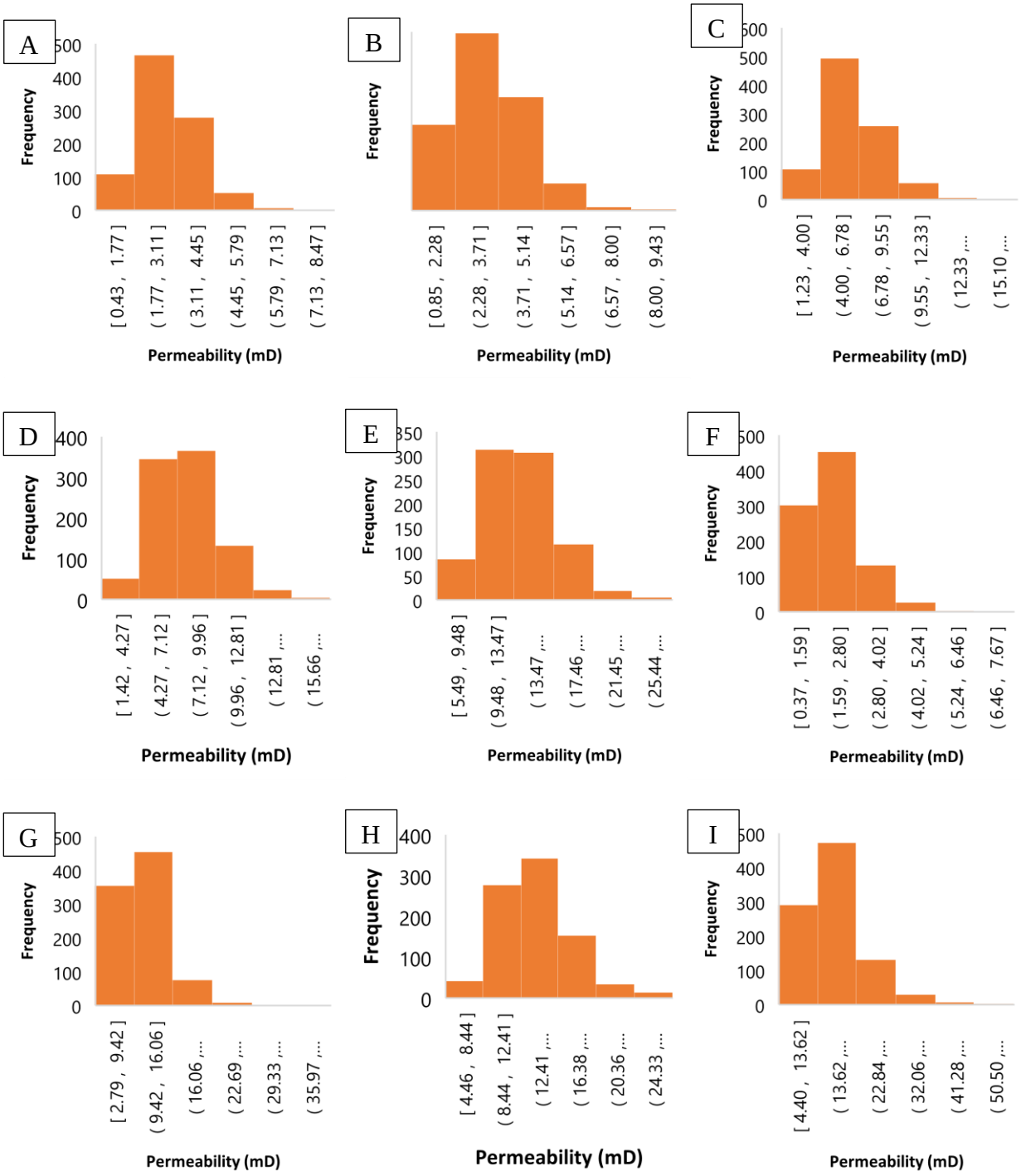

Fig. 3.7. Permeability distribution from stochastic pore scale simulations through the generated 3D pore-microstructures for each core plug.

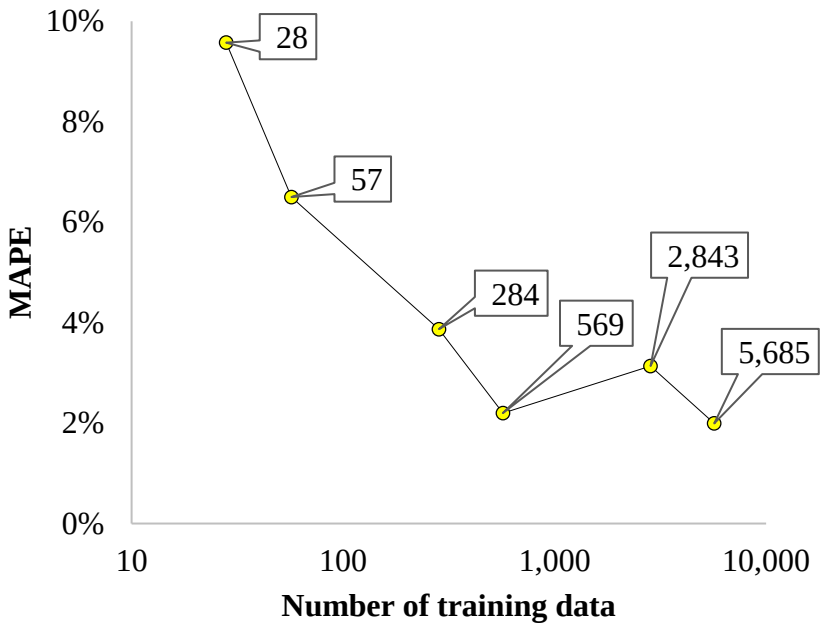

Fig. 3.8. MAPE of permeability of all nine core plugs used in this study. MAPE by core plug is shown in the supplementary information (Fig. 3.2S). The data highlighted in plot is number of training data.

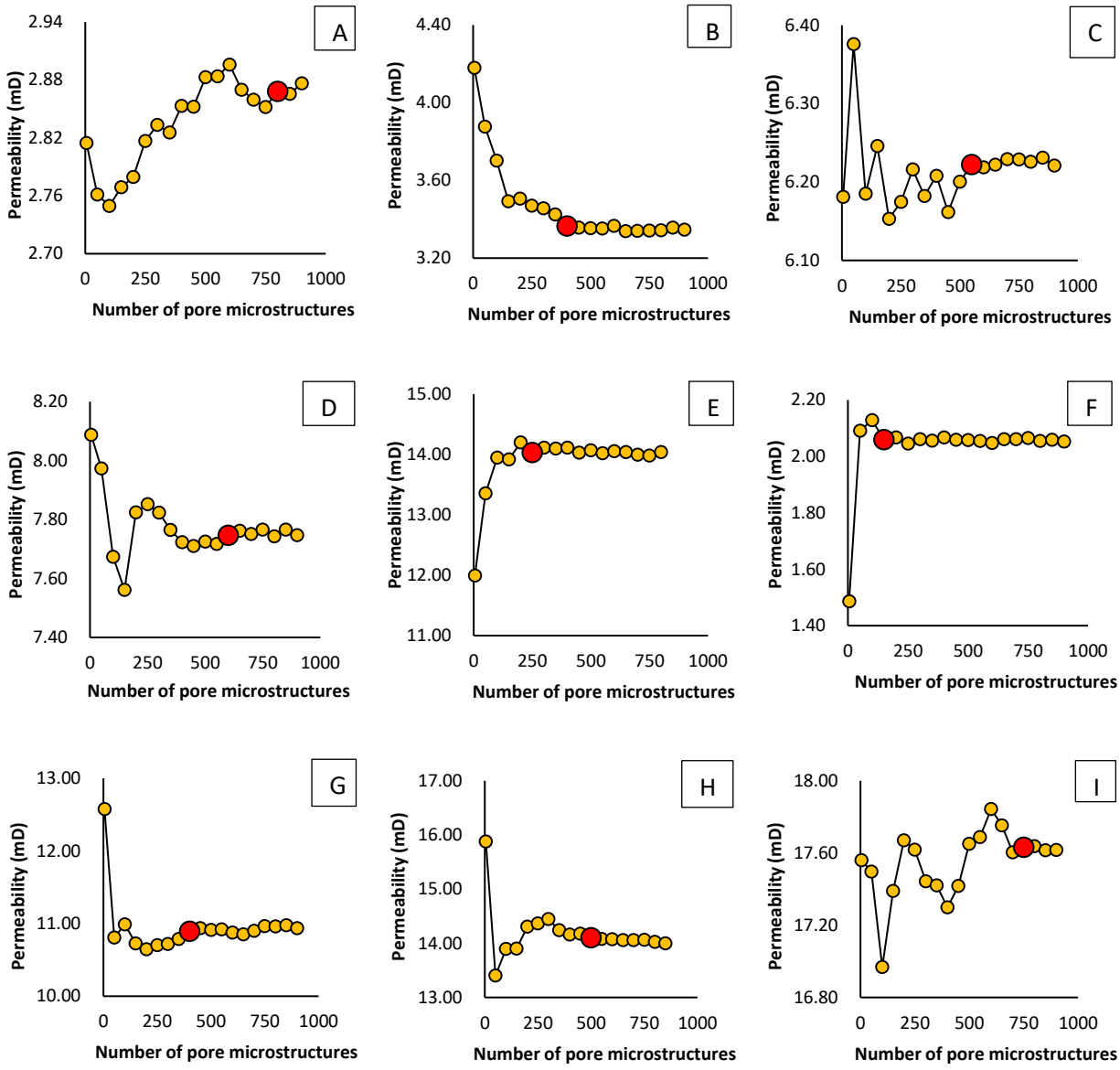

Fig. 3.9. Change in calculated permeability with number of 3D pore microstructures used for pore-scale flow simulations. The red point indicates the representative permeability value of the respective core plug.

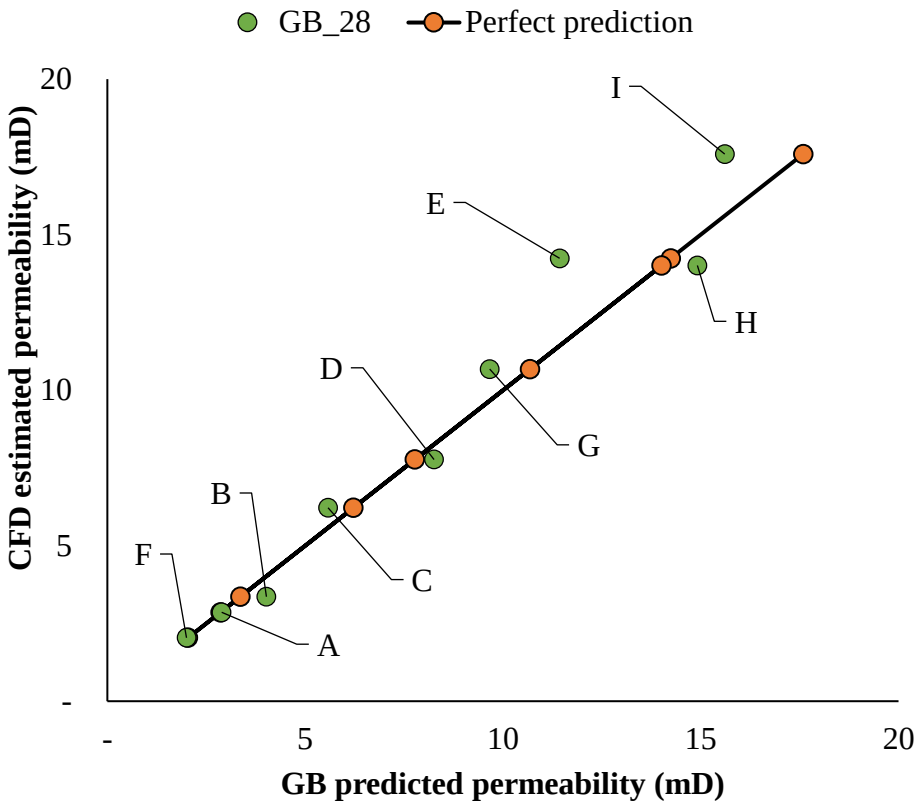

Fig. 3.10. A comparison between permeability predictions made using a GB model trained with 28 pore microstructural parameters (green) and an hypothetical perfect prediction (orange). The higlighted numbers are respective core plug IDs.

Tables

Table 3.1. Comparison of permeability (mD) between previous deterministic approaches and the stochastic pore-scale simulation approach used in this study with mean absolute percentage error (MAPE)

Sample	A	B	C	D	E	F	G	H	I	MAPE	Rank
Experimental permeability	20.96	3.19	15.13	35.31	8.73	17.03	15.13	6.69	52.46	NA	NA
Winland(S. Kolodzie, Jr., 1980)	9.29	68.75	46.16	40.51	68.66	53.14	240.16	36.18	536.31	676%	4th
Swanson(B. F. Swanson, 1981)	12.68	55.93	42.19	40.02	67.83	44.88	232.4	26.19	1593.46	821%	5th
Wells-Amaefule(Walls & Amaefule, 1985)	2.28	7.24	5.82	5.58	8.41	6.10	21.94	4.01	98.10	67%	2nd
Kamath(J. Kamath, 1992)	24.29	79.41	63.41	60.8	92.62	66.62	247.46	43.34	1150.05	914%	6th
Dastidar(R. Dastidar et al., 2007)	5.22	36.49	12.24	12.14	57.81	6.05	49.02	11.44	1640.37	573%	3rd
Stochastic simulation approach	2.87	3.33	6.21	7.75	14.00	2.05	10.94	14.00	17.60	64%	1st

Table 3.2. The respective absolute error (mD) across the nine core plugs in Table 3.1.

Sample	A	B	C	D	E	F	G	H	I
Winland(S. Kolodzie, Jr., 1980)	11.67	65.56	31.03	5.2	59.93	36.11	225.03	29.49	483.85
Swanson(B. F. Swanson, 1981)	8.28	52.74	27.06	4.71	59.10	27.85	217.27	19.5.0	1541.00
Wells-Amaefule(Walls & Amaefule, 1985)	18.68	4.05	9.31	29.73	0.32	10.93	6.81	2.68	45.64
Kamath(J. Kamath, 1992)	3.33	76.22	48.28	25.49	83.89	49.59	232.33	36.65	1097.59
Dastidar(R. Dastidar et al., 2007)	15.74	33.30	2.89	23.17	49.08	10.98	33.89	4.75	1587.91
Stochastic simulation approach	18.09	0.14	8.92	27.56	5.27	14.98	4.19	7.31	34.86

Table 3.3. Data summary of the empirical deterministic permeability models explored in this study (modified after Comisky et al., 2007).

Method	Year	Number of Samples	Sample Source	Permeability Measurement Type (s)	Permeability Range (mD)	Data Density*
Winland(S. Kolodzie, Jr., 1980)	1980	322	Mixed	Air, Klinkenberg corrected	N/A	N/A
Swanson(B. F. Swanson, 1981)	1981	56	Mixed	Brine	0.002-1000	0.06
Wells-Amaefule(Walls & Amaefule, 1985)	1985	35	Siliciclastic	pulse decay	0.00002-70	0.50
Kamath(J. Kamath, 1992)	1992	301	Mixed	Klinkenberg corrected	1-2000	0.10
Dastidar(R. Dastidar et al., 2007)	2007	150	Siliciclastic	Klinkenberg corrected	0.0001-10000	0.02

*Estimated by diving the number of samples by the permeability range.

Supplementary information

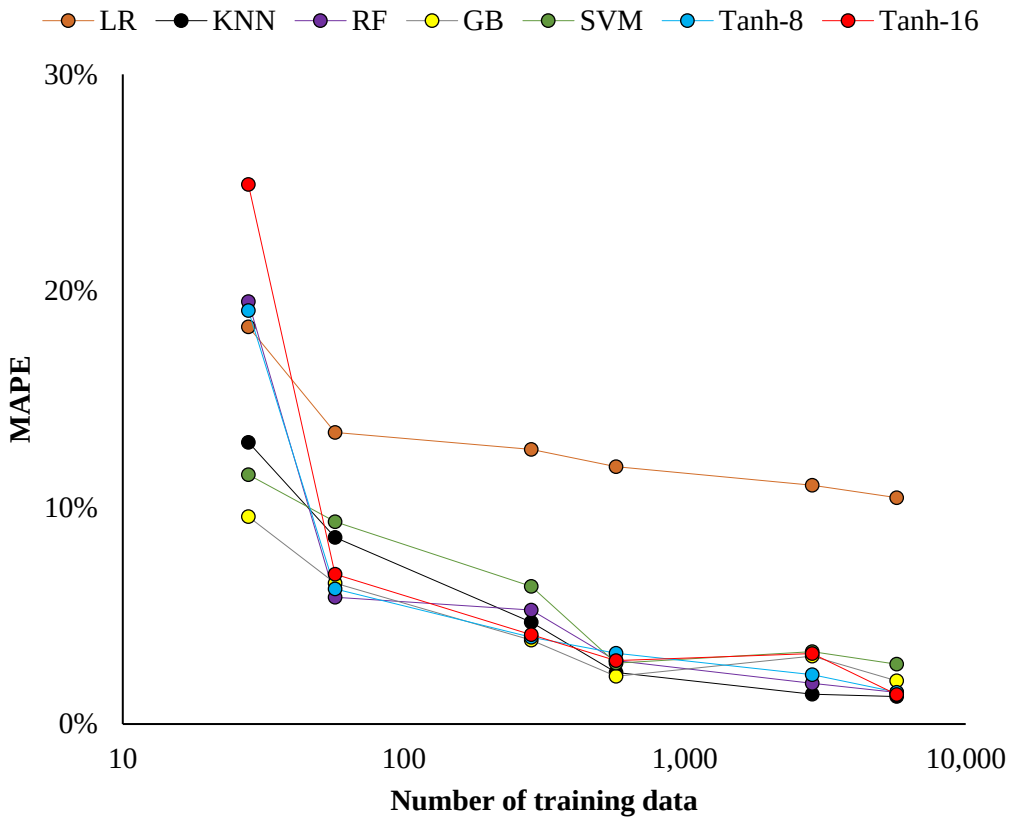

Figure 3.1S. Dependence of accuracy on training size across different machine learning algorithms. The hyperparameters for the various algorithm is detailed on Table 3.3S.

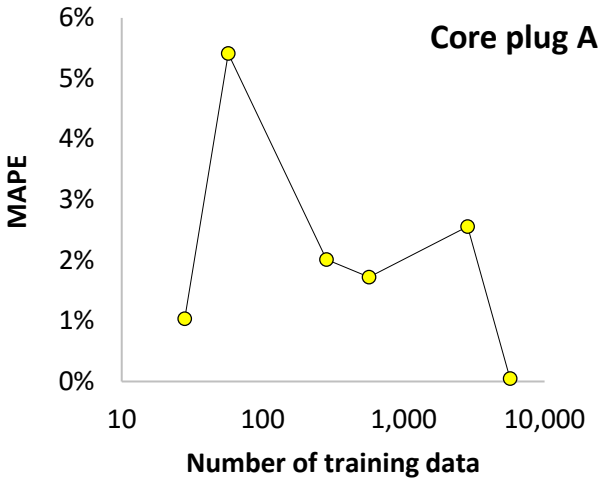
Core plug A
MAPE
6%
5%
4%
3%
2%
1%
0%
10
100
1,000
10,000
Number of training data

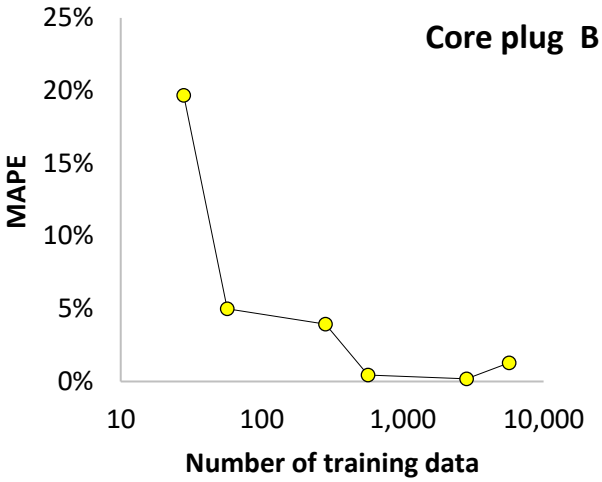
Core plug B
MAPE
25%
20%
15%
10%
5%
0%
10
100
1,000
10,000
Number of training data

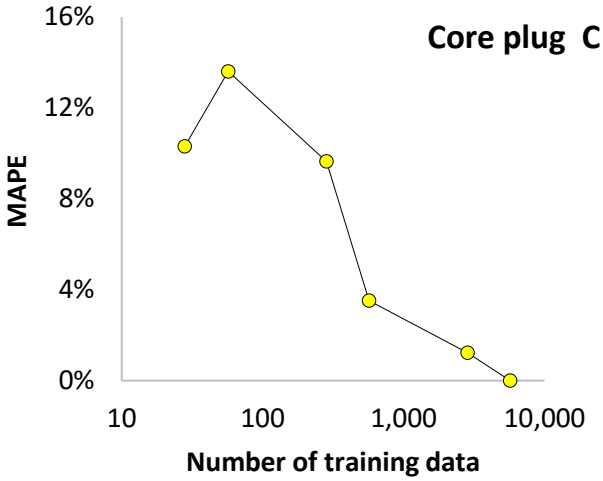
Core plug C
MAPE
16%
12%
8%
4%
0%
10
100
1,000
10,000
Number of training data

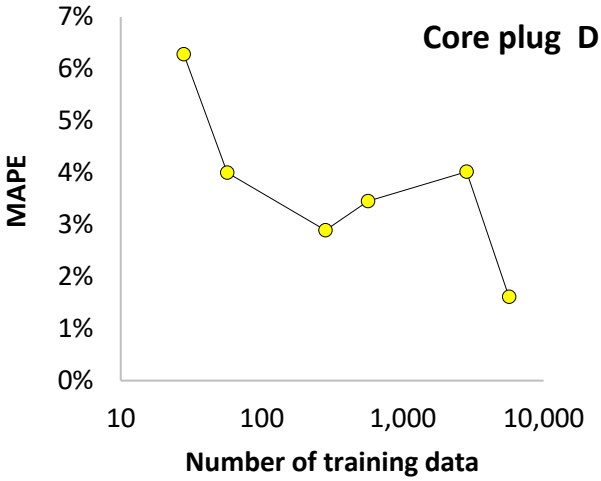
Core plug D
MAPE
7%
6%
5%
4%
3%
2%
1%
0%
10
100
1,000
10,000
Number of training data

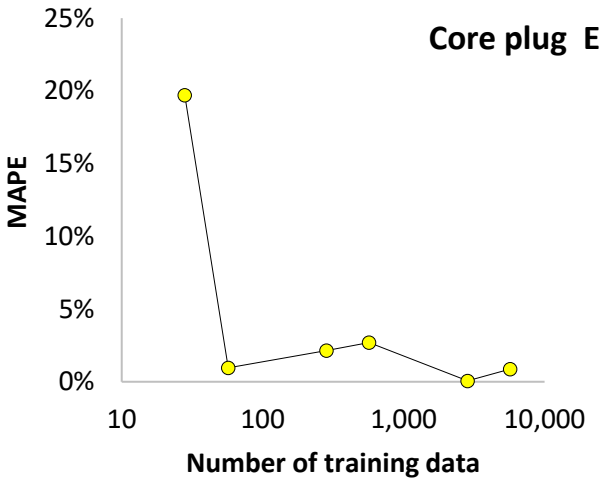
Core plug E
MAPE
25%
20%
15%
10%
5%
0%
10
100
1,000
10,000
Number of training data

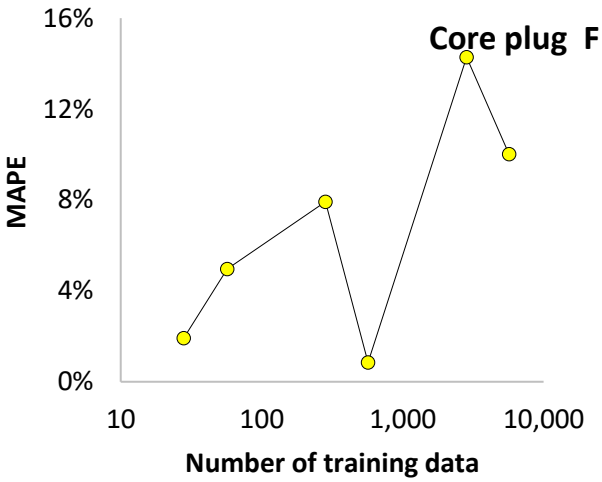
Core plug F
MAPE
16%
12%
8%
4%
0%
10
100
1,000
10,000
Number of training data

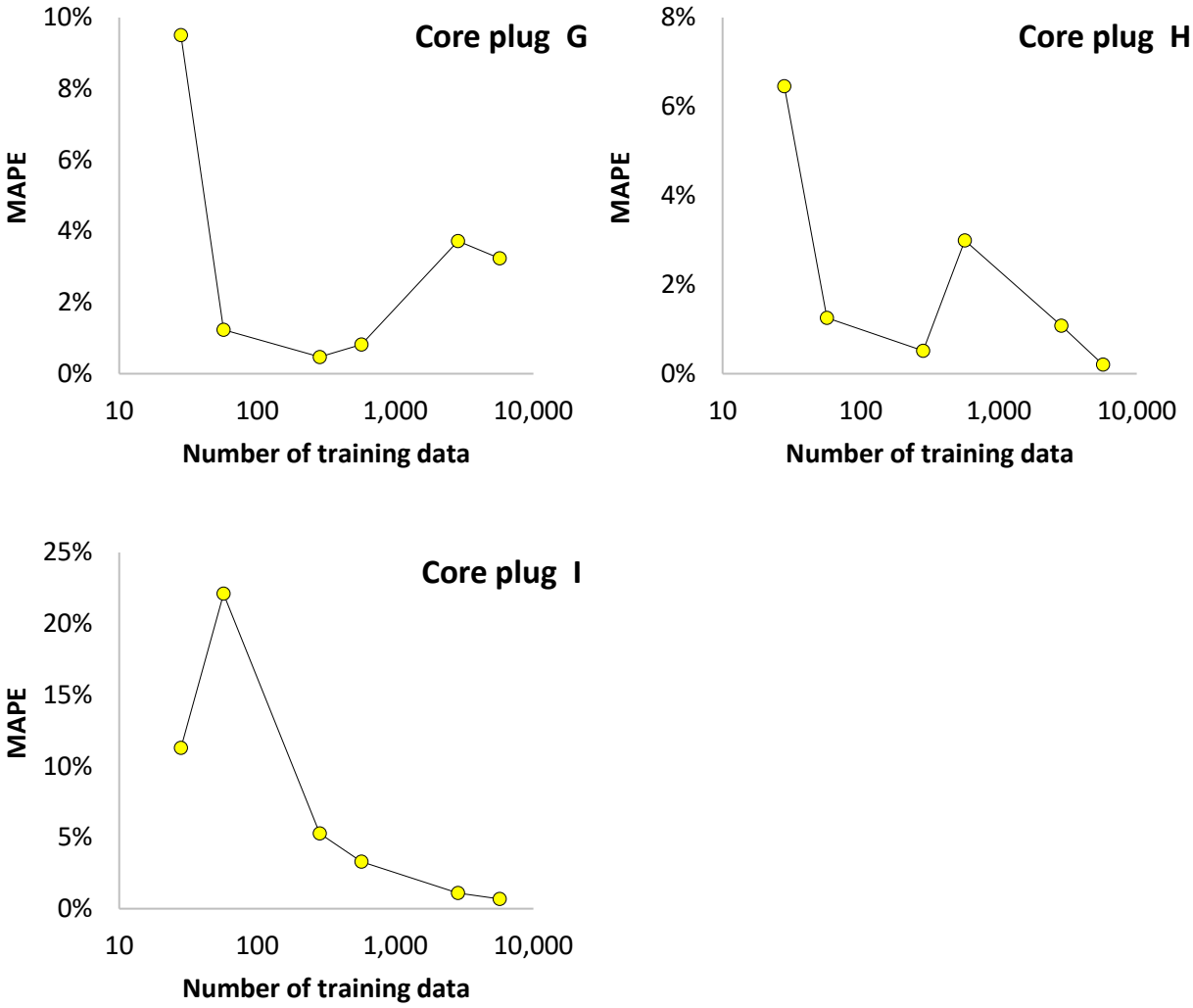

Figure 3.2S. MAPE of permeability by core plug.

Table 3.1S. Arithmetic mean of the data used in for ML training.

Sample	Mean PTSD	Standard deviation PTSD	Percentile of PTSD								count in	count out	count min	Porosity	Domain Length (microns)	Permeability (mD)
			1st	10th	25th	50th	75th	90th	99th							
A	4.45	1.60	1.97	2.68	3.34	4.23	5.18	6.44	9.77		11.28	11.02	8.89	13%	163.13	2.87
B	5.45	1.92	2.40	3.28	4.09	5.18	6.44	7.82	11.63		10.19	10.25	8.13	10%	205.01	3.34
C	5.10	1.86	2.27	3.07	3.84	4.85	5.94	7.26	11.52		12.94	12.93	10.55	16%	176.47	6.22
D	5.41	1.91	2.46	3.29	4.11	5.20	6.29	7.66	11.91		13.45	13.62	11.19	16%	180.06	7.75
E	5.37	1.58	2.59	3.38	4.17	5.28	6.37	7.46	9.61		17.58	17.67	14.93	17%	141.39	14.00
F	4.69	1.82	2.05	2.79	3.49	4.43	5.50	6.76	11.02		9.30	9.03	7.18	12%	201.19	2.05
G	6.18	2.71	2.52	3.54	4.46	5.63	7.06	9.37	16.53		13.82	13.49	11.37	18%	222.21	10.94
H	5.15	1.59	2.42	3.21	3.96	5.02	6.11	7.23	9.64		17.92	18.04	15.15	19%	137.46	14.00
I	6.86	3.69	2.55	3.67	4.68	5.89	7.59	11.39	21.35		14.81	15.00	12.45	21%	256.83	17.60
All**	5.41	2.09	2.36	3.21	4.01	5.08	6.28	7.95	12.61		13.41	13.39	11.04	16%	187.88	8.68

****All samples were used to train ML models simultaneously**

Table 3.2S. Coefficient of variation of the data used in for ML training.

Sample	Mean PTSD	Standard deviation PTSD	Percentile of PTSD							count in	count out	count min	Porosity	Domain Length	Permeability
			1st	10th	25th	50th	75th	90th	99th						
A	1%	4%	3%	2%	2%	1%	2%	2%	5%	32%	32%	27%	2%	3%	35%
B	1%	4%	3%	2%	2%	2%	2%	2%	5%	33%	34%	29%	2%	2%	37%
C	1%	5%	3%	2%	2%	1%	2%	2%	6%	30%	29%	25%	2%	2%	34%
D	1%	5%	3%	2%	2%	1%	1%	2%	6%	28%	29%	25%	2%	2%	31%
E	1%	3%	2%	2%	2%	1%	1%	2%	3%	24%	25%	20%	2%	1%	26%
F	2%	6%	3%	2%	2%	1%	2%	2%	7%	35%	36%	32%	2%	3%	43%
G	2%	5%	3%	2%	2%	2%	2%	4%	6%	28%	27%	24%	2%	2%	37%
H	1%	3%	3%	2%	2%	1%	1%	2%	3%	25%	25%	20%	2%	1%	27%
I	2%	5%	3%	3%	2%	2%	3%	6%	5%	26%	27%	22%	2%	2%	40%
All**	13%	32%	9%	10%	10%	10%	11%	19%	30%	35%	36%	34%	21%	19%	73%

****All samples were used to train ML models simultaneously**

Table 3.3S. Summary of model parameters used for the respective machine learning algorithms.

ML algorithms	Hyperparameters	Additional note
LR **(Linear Regression)**	Not applicable	Data used directly, no basis function or combination used.
KNN **(K- Nearest Neighbor)**	(), {'n_neighbors': [1,5,10,15,20,25,30,35,40,45,50,100,200], 'weights': ["uniform", "distance"]}, cv = 5	All hyperparameters were tested and the best combination based on a five-fold cross validation was selected using GridSearchCV. All other parameters are kept constant. This is applied to KNN, RF, GB, and SVM.
RF **(Random Forest)**	(random_state=100), {'n_estimators': [10,50,100,200,300,400,500,600,700,800,900,1000], 'max_depth': [1,2,3,4,5,6,7,8,9,10]}, cv = 5	
GB **(Gradient Boosting)**	(random_state=100), {'learning_rate': [0.0001, 0.001, 0.1, 1], 'n_estimators': [10,100,200,300,400,500,600,700,800,900,1000], 'max_depth': [3,4,5,6,7,8,9,10]}, cv = 5	
SVM **(Support Vector Machine)**	(), {'C': [1,10,50,100,150,200,250,300],'epsilon': [0.05,0.1,0.3,0.5], 'kernel': ['linear', 'poly', 'rbf', 'sigmoid']}, cv = 5	
Tanh-8 **(Feed forward Neural network)**	one hidden layer; activation="tanh"; batch normalization. model_checkpoint = tf.keras.callbacks.ModelCheckpoint(filepath=checkpoint_filepath, save_weights_only=True, monitor='val_loss', mode='min', save_best_only=True, verbose=0, save_freq="epoch") history = model.fit(X_train_std, y_train, batch_size = 3000, epochs = 20000, verbose = 2, validation_split = 0.2, callbacks=[model_checkpoint])	For Tanh-8 the number of neurons is 8 while Tanh-16 had 16 neurons. Due to the random nature of initial weights in Feed Forward Neural Network, model predictions are expected to vary when training is repeated. To account for this, training and predictions were repeated 20 times for the same set of parameters. An average of the predictions was used as the final prediction of targets.
Tanh-16 **(Feed forward Neural network)**		

CHAPTER IV

AUGMENTING XRAY MICRO-CT DATA WITH MICP DATA FOR HIGH RESOLUTION PORE-MICROSTRUCTURAL AND FLOW MODELLING OF CARBONATE ROCKS.

4.1 Abstract

Pore microstructural modelling is essential in understanding transport processes through rocks and is very critical in many geoscience and engineering applications. Generally, pore microstructural modeling is dependent on imaging technologies such as Scanning Electron Microscopy (SEM) and Micro Computed Tomography (micro-CT) to provide data on various pore microstructural elements in a rock. While the use of these imaging techniques provide visual confirmation into the pore microstructures of rocks, they are often limited in the ability to provide high resolution data at representative scale. This is a technological limitation which requires a very small sample to obtain resolution of rocks sufficient to reveal key pore microstructural features that control flow (i.e., pore throats size distribution as well as pore connectivity) especially in tighter rocks. This poses significant challenges to the understanding of transport processes through porous media and limits the capacity to accurately predict flow properties of rocks. In this study, we introduce a novel workflow to generate pore microstructures from high resolution and

statistically representative data. The workflow utilized MICP data to account for pore throat size distribution, micro-CT images for pore body size distribution, and stochastic modeling for pore connectivity. The micro-CT and MICP data used to construct our 3D pore-microstructures were obtained at continuum scale and covers a significant spectrum of pore-microstructural features of interest. Four carbonate rock samples were used to test the proposed workflow, and the generated pore microstructures were validated by comparing the simulated permeability through the pore microstructures with the laboratory measurement of permeability in a representative rock sample.

4.2 Introduction

Pore microstructures are fundamental to flow and transport processes in rocks (Ishola et al., 2022; Regnet et al., 2019; Starnoni et al., 2017). Appropriate information of the pore microstructure is crucial in many geoscience and engineering applications. The pore microstructure of rocks control fundamental flow and transport properties such as permeability and hydraulic tortuosity (Ishola et al., 2022). These properties are crucial in hydrocarbon exploration, geothermal exploration, groundwater exploration, carbon sequestration, hydrogen storage, mineral exploration, and environmental studies. The pore microstructure of rocks can be described as the configuration of voids. Characteristic features of pore microstructures include pore throats, pore body, pore shape and pore topology. These features vary in rocks because of heterogeneity. Generally, pore microstructures are less heterogenous in siliciclastic rocks and more heterogenous in carbonate rocks. Heterogeneity in pore microstructures results largely from a combination of deposition and diagenesis (Hollis, 2011; Morad et al., 2010; Regnet et al., 2019; Wang

et al., 2017). An increase in the degree of heterogeneity has been shown to lead to increased degree of uncertainty in permeability and hydraulic tortuosity of rocks (Ishola et al., 2022).

Traditionally, flow properties such as permeability are predicted from pore-microstructural information measurable in rock samples such as porosity. While this approaches generally work well in siliciclastics, they often fail in carbonate rocks because of the inherent heterogeneity (Dasgupta & Mukherjee, 2020; Westphal et al., 2005). Porosity measurements have been shown to have possible permeability measurements spanning five orders of magnitude in permeability (Westphal et al., 2005; Yang & Aplin, 2010; Zhang et al., 2017). Inclusion of pore size distribution data via measurements like nuclear magnetic resonance (NMR) (Westphal et al., 2005) and mercury injection capillary pressure (MICP) (Comisky et al., 2007) has help constrained empirical approaches to predicting permeability. The next step to further constrain flow properties of rocks is to account for pore connectivity. Connectivity is known to play a key role on fluid flow (Bernabé et al., 2010; Civan, 2002; Dasgupta & Mukherjee, 2020; Ishola et al., 2022; Zhao et al., 2022). Conventionally, the inclusion of pore connectivity in pore microstructural modelling relies on imaging techniques which are used to reveal the position of three-dimensional connections that exist between pores in rocks. There are two main techniques for obtaining 3D images of rocks. The more common approach is the use of X-ray computed tomography (micro-CT) (Bazaikin et al., 2017; Xiong et al., 2016; Zhang et al., 2019). Micro-CT has the capacity to image relatively large volumes of rocks (typically, rock cores of 1-inch diameter by few inches length) such that the calculated rock properties are representative at continuum scale. That said, there is a linear relationship between sample size and resolution of images obtained from micro-CT (Bazaikin et al., 2017). This

implies that obtaining high resolution images of rocks is only possible for smaller sample sizes which is as the cost of the representative nature of pore-microstructural information obtained from the samples (Bazaikin et al., 2017; Blunt et al., 2013; Mees et al., 2003; Xiong et al., 2016). Conversely, a representative sample size has lower image resolution resulting in the erosion of smaller pore-throats and the associated pore connectivity. For a sample size ranging from ~0.5 to ~100 mm, the corresponding resolution of images obtainable ranges from ~0.7 to ~ 120 μm (Wang & Miller, 2020). The inability of micro-CT to capture the connecting paths in rocks at representative scale results in 3D images of floating unconnected pores which is not suitable for direct simulation of fluid flow on the 3D image. Poor resolution of micro-CT images could also lump unresolved pore microstructures with larger ones resulting in a higher average sizes of pore-microstructural features which can significantly increase permeability (Devarapalli et al., 2017). In agreement to the observations of Devarapalli and others, Saxena et al. (2019) and others showed the lower limit of permeability for a given porosity to increase with coarser resolution of micro-CT images due to the overestimation of pore-throat sizes in the micro-CT images (Saxena et al., 2019; Saxena et al., 2018). This indicates the crucial role of resolution in making flow predictions from rock micro-CT images.

An alternative approach to obtaining high resolution images of rock samples is using the focussed ion beam scanning electron microscope imaging technique (FIB-SEM) (Blunt et al., 2013; Uchic et al., 2007; Xiong et al., 2016). FIB-SEM is a destructive technique that provides image resolution of up to 0.4 nm but can only practically image up to tens of cubic microns of the image which is not statistically representative of heterogeneous rocks because the statistical occurrence of pores with sizes in the order of tens to hundreds of

cubic microns cannot be obtained from this data (Saraji & Piri, 2015; Uchic et al., 2007; Xiong et al., 2016). Although obtaining high resolution images with micro-CT and FIB-SEM comes at the cost of sample size (Saxena et al., 2018), its resultant effect on a rock's representative elementary volume (REV) might be inconsequential. This is because the volume to reach REV will often get larger as heterogeneity increases (Adeleye & Akanji, 2017; Bear, 1972). Hence, for relatively homogenous samples, smaller sample sizes might suffice, allowing the acquisition of high-resolution images that are representative in nature.

Generally, poor image resolution hinders the ability to visualize pore connectivity in representative rock samples, making it difficult to simulate fluid flow as these connections between pores are the pathways for fluid movement through the rock. There are several approaches to accounting for pore connectivity in images with poor resolution. This includes the use of random distribution of pore connectivity to account for possible connectivity scenarios (Jivkov et al., 2013; Jivkov & Xiong, 2014). However, the approach by Jivkov and others assumes uniform spatial distribution of pore centroids which is not the case in heterogenous rocks. Mehmani and Prodanovic´, 2014 approached pore network modelling differently by using the Delaunay tessellation of grain centres in a two-scale network construction. The workflow yielded less structured spatial distribution but assumes a fixed connectivity with a coordination number of four in its *macronetwork* and *micronetwork* (Mehmani & Prodanović, 2014). The fixed nature of pore connectivity is the key limit of this approach as this is not a feasible configuration for heterogeneous rocks. Statistical approaches such as multiple-point statistics (Okabe & Blunt, 2004) have been shown to reproduce realistic pore-microstructural information of 2D thin sections of rocks which in turn produced reasonable permeability values. Wu and others improved on

this by using 3D micro-CT images in their reconstruction which accounts for anisotropy and 3D configuration of the pore microstructure (Y. Wu et al., 2018). Like the modelling approaches led by Jikov, Mehmani, and Okabe (Jivkov et al., 2013; Jivkov & Xiong, 2014; Mehmani & Prodanović, 2014; Okabe & Blunt, 2004), the capacity of 3D multipoint statistics to capture and produce realistic pore connectivity depends on the quality of the image in terms of resolution and its statistical representation of the rock sample. Furthermore, the proposed workflow by Wu and others does not work well with high heterogeneity (Y. Wu et al., 2018).

In an earlier study (Ishola et al., 2022), we emphasize the relevance of accounting for the stochastic connectivity of pores in making predictions of permeability and hydraulic tortuosity of heterogeneous porous media by using equally probable pore connectivity scenarios where porosity and pore size distribution are kept constant. The approach in this study replicates permeability pattern found in real rocks which is validated by the lognormal distribution of permeability found in real heterogenous rocks (Malin et al., 2020; Sahin et al., 2007). In another study (Ishola & Vilcáez, 2022), we applied the proposed stochastic pore-scale simulation approach to predict permeability of nine rocks. Generally, the estimated permeability of the samples was closer to true values when compared to five popular permeability equations. In the current study, we built on our existing workflow (Ishola et al., 2022) to generate realistic pore microstructural models by augmenting X-ray micro-CT data with MICP data to account for a wider range of pore sizes. This novel workflow uses high resolution and statistically representative data simultaneously. Here, we estimate a critical pore throat radius (EPTR) from MICP data while the distribution of pore body radius (PSD) was obtained from micro-CT images.

Like other studies, we simplified the pore shape to a sphere of equivalent volume to the true geometry. To account for pore connectivity, we employed the stochastic approach by (Ishola et al., 2022; Ishola & Vilcáez, 2022) to generate equally probable flow paths in rock samples of the same porosity and pore size distribution. The results of this approach are validated by comparing the simulated permeabilities using the stochastically constructed 3D pore microstructures to laboratory measurements as well as estimates from well-known empirical permeability models.

4.3 Material and methods

Four carbonate rock samples were used in this study (Fig. 4.1). For each of the rock samples three sets of data were obtained. This includes laboratory permeability measurement of the samples (Section 2.1), MICP information (Section 2.2), and 3D micro-CT images (Section 2.3). This dataset what used to generate pore microstructural models (Section 2.4) and validated via numerical simulation of permeability (Section 2.5).

4.3.1 Rock permeability

Permeability of our samples were obtained using Darcy's law (Darcy, 1856) via Eq. (4.1).

$$K = \frac{Q \times \mu \times L}{A \times \Delta P} \tag{4.1}$$

where K is the absolute permeability of the rock domain (m^2), Q is the volumetric flowrate through the samples (m^3/s), μ is the dynamic viscosity of the fluid injected into the samples (Pa-s), L is the length along the principal direction of fluid travel in the samples (m), A is

the cross-sectional area of flow (m^2), and ΔP is the pressure drop in the principal direction of the fluid (Pa).

In our laboratory setup for permeability measurement, we used a Hassler Type core-holder (RCH-series of Core Laboratory) to hold respective core samples at a pressure of 2000 psi. Water was injected into the held core samples with a 260 dual syringe pump (Teledyne ISCO) at flow rates ranging from 0.025 to 0.5 ml/min. The range of flow rate used in this study resulted in a maximum Reynolds number of 1×10^{-4} which ensures that the application of Darcy's laws to estimate permeability is valid in all our laboratory experiments. We used a Rosemount Pressure Sensor to measure pressure at the inlet of our samples while the outlet pressure is known to be atmospheric pressure for our experimental setup. The experiment is deemed to have reached steady state when the pressure-drop across the sample stopped changing through time. MICP data of the samples were obtained from Integrated Core Characterization Center, University of Oklahoma, USA while micro-CT images of the rock samples were obtained using Phoenix Nanotom M at Baker Hughes facility in Oklahoma City, USA.

4.3.2 Effective pore throat radius

In this study, we propose the use of an effective pore throat radius (EPTR) to help capture the resultant effect of pore throats in a rock. EPTR in this study refers to the weighted average pore throat size, estimated from MICP data of a representative rock sample (Fig. 4.2). This is an improvement from previous studies where pore throat used in pore microstructural modelling is often inferred from micro-CT images (Sun et al., 2021;

Willson et al., 2012; K. Zhang et al., 2022) which has poor resolution for representative volume required to represent a rock sample (Bazaikin et al., 2017; Blunt et al., 2013; Mees et al., 2003; Xiong et al., 2016). We estimated EPTR from MICP data of rock sample at continuum scale via three steps:

Step one: Account for the ink bottle effect. The shadowing or ink-bottle phenomenon (Xiong et al., 2016) causes overestimation of smaller pores since incremental pressure in MICP acquisition tends to mask large volume hidden behind tight pores as tighter pores. For this study, we applied a cut off at the minimum incremental pore volume (MIPV). MIPV (Fig. 4.2) represents the pore size where the incremental porosity abruptly reduces close to zero before attaining 100% mercury saturation (Ishola & Vilcáez, 2022). While this approach tries to remove false data, it is noteworthy that it also ignores pores sizes less than MIPV cut off. Change in incremental pore volume (Fig. 4.2 red line) is used to track differences in incremental pore volume at the start of the incremental pore volume vs pore-throat radius plot. Broken green line is interpreted as MIPV in the samples in this study (Fig. 4.2). It's noteworthy that the start of the incremental pore volume is 100% mercury saturation, hence, the application of MIPV to the start of the plot.

Step two: Estimate the weight of each pore-throat size. In a previous work by Dastidar and others, the fraction of each incremental pore volume is used as weights Eq. (4.2) (Rahul Dastidar, Carl H Sondergeld, et al., 2007).

$$w_i = \frac{v_i}{\sum_{i=1}^{n}(v_i)} \tag{4.2}$$

Where n is the number of pore-throat size data point, v_i is the incremental pore volume of a given pore-throat i.

Here, we used the ratio of the incremental pore volume to the curved surface area (s) of an equivalent cylinder as weights:

$$w_i = \frac{v_i/s_i}{\sum_{i=1}^{n}(v_i/s_i)} \tag{4.3}$$

curved surface area (s) is given by:

$$s_i = 2\pi r_i h_i \tag{4.4}$$

Where r_i is the radius of a given pore-throat i and h_i is corresponding the pore throat length. In this study we assumed h_i to be constant, hence, s_i is controlled by r_i in Eq. (4.4).

The incremental pore volume (v_i) accounts for the fraction of total volume of fluid a pore throat (i) controls resulting in that pore throat size having more influence on flow through the rock sample. The curved surface area s_i is introduced in this study to account for the impact of frictional interaction at the fluid-rock interface which negates flow through a pore-throat i. Curved surface area and not total surface area is used here because the pore throats are idealized as cylinders and the portion of the cylinder having the frictional interaction with the fluid flowing through is the curved surface since the idealized cylinder is expected to be hollow for fluid to pass through it.

Step three: Calculate the EPTR by using the estimated weights to compute a weighted average pore throat radius (Eq. 4.5).

$$EPTR = \frac{\sum_{i=1}^{n}(w_i \times r_i)}{\sum_{i=1}^{n}(w_i)} \tag{4.5}$$

The estimated EPTR (Table 1) was used as the pore throat radius to construct pore microstructures following our stochastic approach (Ishola et al., 2022; Ishola & Vilcáez, 2022). The MICP data also provided effective porosity which was used as control to constrain constructed pore microstructures.

4.3.3 Pore-body size distribution (PSD) data

The PSD used in this study was obtained from micro-CT images of the rock samples in Fig. 4.1. The size of the micro-CT images for all the samples is 1000 x 1000 x 1000 pixels in x, y, and z directions with a resolution of 7.5 μm (Fig. 4.3). The resulting 422 mm^3 volumes were segmented (Fig. 4.4.) to separate the pores in the image from the background using a watershed algorithm. The watershed algorithm (Gostick, 2017) was used to help disconnect pores that are connected which prevents the estimation of local pore networks as a single pore volume. The volume distribution of the resultant isolated pores was obtained from the segmented image. PSD (Fig. 4.5) is obtained from the volume distribution by calculating the pore radius of equivalent spherical volume for each of the pores Eq. (4.6).

$$R_i = \sqrt[3]{\frac{3\times V_i}{4\times \pi}} \tag{4.6}$$

Where R_i is the radius of the equivalent sphere of volume V_i and i is the pore obtained from the micro-CT image.

To verify the representative nature of the PSD data, we conducted a representative elementary volume (REV) analysis on the segmented 3D image for each sample (Bear, 1972). The purpose of the REV was to determine if the PSD obtained from the micro-CT data is representative. In the REV analysis, we evaluated the percentage change in average PSD, standard deviation of PSD, and skewness of PSD (Fig. 4.6) for volumes of micro-CT image data (Fig. 4.4), ranging from 0.05 mm^3 to 422 mm^3. For this study, a 5% change in average pore-size was applied as cut off for the representative volume. The REV study showed all our samples to have a representative volume of 27 mm^3 given by the relatively low percentage change in all the three statistical parameters tracked through the varying volume of the rock images (Fig. 4.6). This implies that any subsample in the range of 27 mm^3 to 422 mm^3 will approximately have the same PSD.

4.3.4 Stochastic generation of 3D pore microstructures

In this study, we employ the 3D stochastics pore generation approach used by (Ishola & Vilcáez, 2022) to generate pore microstructures of the same pore size distribution and effective porosity but different pore connectivity. The pore sizes were randomly obtained from the respective PSDs of the samples and the pore throat sizes were fixed to the respective EPTRs. The pore microstructures construction approach involves the stochastic spatial distribution of pores in a computational domain given four constraints. The first constraint is that the first pore in the computational domain is at the centre to allow equal possible spreading path to the entire domain. Subsequent connections start randomly along established paths in the computational domain. The second is that a space already occupied by a pore is no longer available to subsequent pores added into the

system. The third constraint is that for a pore microstructure to be valid, there must be at least a connecting path between the inlet and outlet of the computational domain. The fourth constraint is that porosity is equal to effective porosity, and this is provided by the MICP data in this study. The resultant stochastic pore microstructure has equal probability of occurring while honouring the effective porosity and pore size distribution of the parent sample (Fig. 4.7). The number of pores in each pore microstructures in this study ranges from 950 to 1000 which consequently results in digital rock volume ranging from 6.07 to 25.44 mm^3 (Table 4.2). It is noteworthy that the digital rock volume varies depending on the number of pores in each pore-microstructural model (Table 4.2), sizes of the pores sampled from the PSD (Fig. 4.5), and the effective porosity of the sample (Fig. 4.2). In this study we assumed a cylindrical pore throat with length of 1 μm.

4.3.5 Model validation

4.3.5.1 Pore-scale simulations and permeability estimations for validation

Fluid flow was simulated through each of the stochastically generated 3D pore microstructures (Fig. 4.7). For each sample, 200 pore microstructures were generated and used for flow simulation. Steady state simulations of fluid flow (Fig. 4.8) were accomplished with STAR-CCM+®, a computational fluid dynamics software that solves the mass continuity equation (Eq. 4.7) and Navier Stokes equation (Eq. 4.8) using its finite volume methodology.

$$\vec{\nabla} \cdot \rho\vec{V} + \frac{\partial \rho}{\partial t} = 0 \tag{4.7}$$

$$\frac{\partial \vec{V}}{\partial t} + \left(\vec{V} \cdot \vec{\nabla}\right)\vec{V} = -\frac{1}{\rho}\vec{\nabla}P + v\vec{\nabla}^2\vec{V} \tag{4.8}$$

where ρ is density of the fluid, v is kinematic viscosity, P is pressure, t is time, and $\vec{V}$ is fluid velocity.

STAR-CCM+® has been benchmarked against experiments and shown to accurately replicate pore scale fluid flow (Oostrom et al., 2014; Yang et al., 2016; Yang et al., 2013). In this study, we used an unstructured polyhedral mesh type to capture the complex geometry of the pore-microstructural models generated. All the generated pore microstructures were assigned a minimum cell size of 0.2 μm while other parameters in the mesh generator were kept at default. The number of cells in each pore microstructure varied from 3,050,166 to 6,141,038 (Table 3). In all simulations, water was used as the fluid and there was no chemical reaction in the computational domain. A no-slip wall boundary condition was used throughout the computational domain except at the opposite sides along the intended flow direction which had inlet pressure set at 1 Pa and outlet pressure set at 0 Pa to drive fluid flow. To ensure that permeability calculations were valid, we made certain that the Reynolds number of all the pore scale simulations was less than 1 since Darcy's law (Darcy, 1856) was used in making estimating permeability (Eq. 4.1). All simulations were seen to have converged for permeability when the change in permeability in the last two iterations is less than 1% while attaining residuals (continuity, x momentum, y momentum, and z momentum) less than 10^{-4} by the end of 200 iterations assigned in all our flow simulations.

4.3.5.2 Benchmarking simulated permeability.

To evaluate if augmenting X-ray micro-CT data with MICP data produce realistic pore microstructures using our previously proposed stochastic pore-scale simulation approach, the arithmetic average permeability of 200 possible pore microstructures was compared with measured permeability values from rock samples as well as estimations from popular empirical models. Empirical models considered includes Winland (S. Kolodzie, 1980), Swanson (B. Swanson, 1981), Wells-Amaefule (Wells & Amaefule, 1985), Kamath (Jairam Kamath, 1992), and Dastidar models (Rahul Dastidar, Carl H Sondergeld, et al., 2007) given by Eq. (4.9) – (4.13).

$$k_{Winland} = 49.4 * R_{35}^{1.7} * \emptyset^{1.47} \quad (4.9)$$

$$k_{Swanson\text{-}brine} = 355 * \left[\frac{s_b}{P_C}\right]_A^{2.005} \quad (4.10)$$

$$k_{Wells\text{-}Amaefule} = 30.5 * \left[\frac{s_b}{P_C}\right]_A^{1.56} \quad (4.11)$$

$$k_{Kamath} = 347 * \left[\frac{s_b}{P_C}\right]_A^{1.60} \quad (4.12)$$

$$k_{Dastidar} = 4073 * R_{wgm}^{1.64} * \emptyset^{4.06} \quad (4.13)$$

where s_b is the percent bulk volume occupied by mercury, P_C is the mercury capillary pressure (Psia), A is the maximum amplitude, R_{35} is 35% mercury saturation of pore volume, $\emptyset$ is porosity (fraction), and R_{wgm} is the geometric mean of pore sizes.

4.4 Results and discussion

4.4.1 The role of stochastic pore connectivity in pore scale numerical simulations

In this study, we evaluated the importance of pore connectivity on estimating permeability and hydraulic tortuosity using fluid flow simulations on stochastically

generated 3D pore-microstructures for each sample. Each sample despite using a fixed pore throat size (EPTR), fixed porosity, and fixed PSD, shows a permeability distribution (Fig. 4.9) with a coefficient of variation of 34% in sample A, 35% in sample B, 32% in sample C, and 26% in sample D. The variation in permeability in all samples confirms the relevance of accounting for pore connectivity given the range of possible permeability that could have been used in making inferences if only one pore-microstructure was deemed as representing of each sample. The same applies to hydraulic tortuosity which is shown in Fig. 4.10 to have a coefficient of variation of 15% in sample A, 17% in sample B, 14% in sample C, and 12% in sample D. Given that pore connectivity cannot be measured directly in rocks due to limitations in resolution and/or due to high cost, stochastically constructed pore microstructures of equal probability of occurrence helps account for the unknown connectivity in rock samples. Considering the large number of possible connectivity scenarios reflected by a distribution of possible property (permeability and hydraulic tortuosity) values can be used to make more robust inferences.

In this study, we obtain permeability and hydraulic tortuosity of the four samples by computing average permeability (Fig. 4.11) and hydraulic tortuosity (Fig. 4.12) values. The number of pore-scale simulated permeability and hydraulic tortuosity values used to calculate average permeability and hydraulic tortuosity values was deemed sufficient when the percentage change in target property is approximately zero percent. As shown in Fig. 4.11, the number of required pore scale permeability is 144 for sample A, 128 for sample B, 146 for sample C, and 108 for sample D. For hydraulic tortuosity, the number of required simulations to be representative is 61 for sample A, 80 for sample B, 88 for sample C, and 31 for sample D (Fig. 4.12). The number of required pore-microstructures were

lower for hydraulic tortuosity given the lower influence of pore throat sizes and pore connectivity have on hydraulic connectivity compared to permeability (Ishola et al., 2022) which is also underlined by lower CV of hydraulic tortuosity obtained in this study (Fig. 4.10) compared to permeability (Fig. 4.9). A plot of number of pore microstructures to reach REV against heterogeneity in the four samples (Fig. 4.13) show that the number of pore microstructures required to obtain representative permeability and hydraulic tortuosity increases with heterogeneity. This implies that relatively heterogenous rocks benefits more from stochastic modelling.

4.4.2 Pore-microstructural model validation

To validate if augmenting X-ray micro-CT data with MICP data reproduced measured permeability of real heterogenous rock samples, we compared simulated permeability with measured permeability of the samples as well as permeability estimates from five well known model equations. We evaluated how close the estimated permeability from our approach and permeability estimates from the five model equations match the measured permeability of the samples using mean absolute percentage error (MAPE). MAPE is given by $MAPE = \frac{1}{n}\sum_{i=1}^{n}\left|\frac{k_{m,i}-k_{e,i}}{k_{m,i}}\right| \times 100$ where $k_{m,i}$, and $k_{e,i}$ is the measured permeability and estimated permeability of respective samples while n is the total number of samples which is four in this study. Based on MAPE (Table 4 and 5), the estimated permeability from our approach here matches more closely with measured values than the five empirical models considered in this study. From the MAPE calculated, we can interpret estimated permeability from our approach to generally differ from measured value by 53%. The closest MAPE to our result is the estimate obtained from using the

Wells-Amaefule Method which had an MAPE of 90% while the remainder of the empirical models have MAPEs greater than 300%.

The comparative accuracy obtained by augmenting X-ray micro-CT data with MICP data shows that accounting for the stochastic connectivity of pores and actual pore throats, outperforms empirical models in predicting permeability. This validates the workflow introduced in this study where we account for the stochastic connectivity of pore bodies through pore throats via a combination of EPTR from MICP data, PSD from X-ray micro-CT images, and pore connectivity from stochastic modelling. There are at least two ways to reduce MAPE of the current study. This includes, (1) developing efficient codes that allows easy incorporation of the true pore shapes found in micro-CT images which like most studies is approximated to spheres in this study, and (2) obtaining super higher resolution images of the samples at representative scale beyond the micro-CT resolution of 7.5 microns in this study. Solving these problems will push constructed pore microstructures closer to the truth. The use of real pore shapes is important to make our workflow viable for multiphase flows.

4.5 Conclusions

In this study, we augmented X-ray micro-CT data with MICP data for stochastically constructing high resolution 3D pore-microstructures**.** The micro-CT and MICP data used to construct our 3D pore-microstructures were obtained at continuum scale and covers a significant spectrum of pore-microstructural features of interest. The micro-CT and MICP data used to construct our 3D pore-microstructures were obtained at continuum scale and covers a significant spectrum of pore-microstructural features of interest. We showed that

accounting for the stochastic connectivity of the pore microstructures can result in a probabilistic distribution of the target property which guides different possible outcomes that should be considered when the target property is being estimated. The use of a stochastic pore-scale simulation approach is shown here to be more beneficial when there is a higher degree of heterogeneity in PSD. This is shown to be the case with permeability and hydraulic tortuosity which are key controls of transport in porous media. We validated the introduced pore scale modelling approach by showing that upscaled pore scale permeabilities match more closely with measured results in comparison to five well known empirical models. It is noteworthy that this study is based on single phase flow. To capture key concepts in multiphase flows, we suggest the use of angular or irregular shapes instead of spherical pores. Our workflow will help build models that will help improve understanding of pore scale processes and better assess their role in fluid flow as well as reactive transport processes at pore and continuum scale. Key areas of application for this workflow includes, petroleum exploration and production, carbon sequestration, environmental studies, and groundwater exploration. In the future, we intend to expand the study outside porosity range (10-16%) and permeability range (5-35mD) of the samples in this study to help test the efficacy of the introduced workflow on more diverse rock types while using true geometry found in micro-CT images of rock samples.

Figures

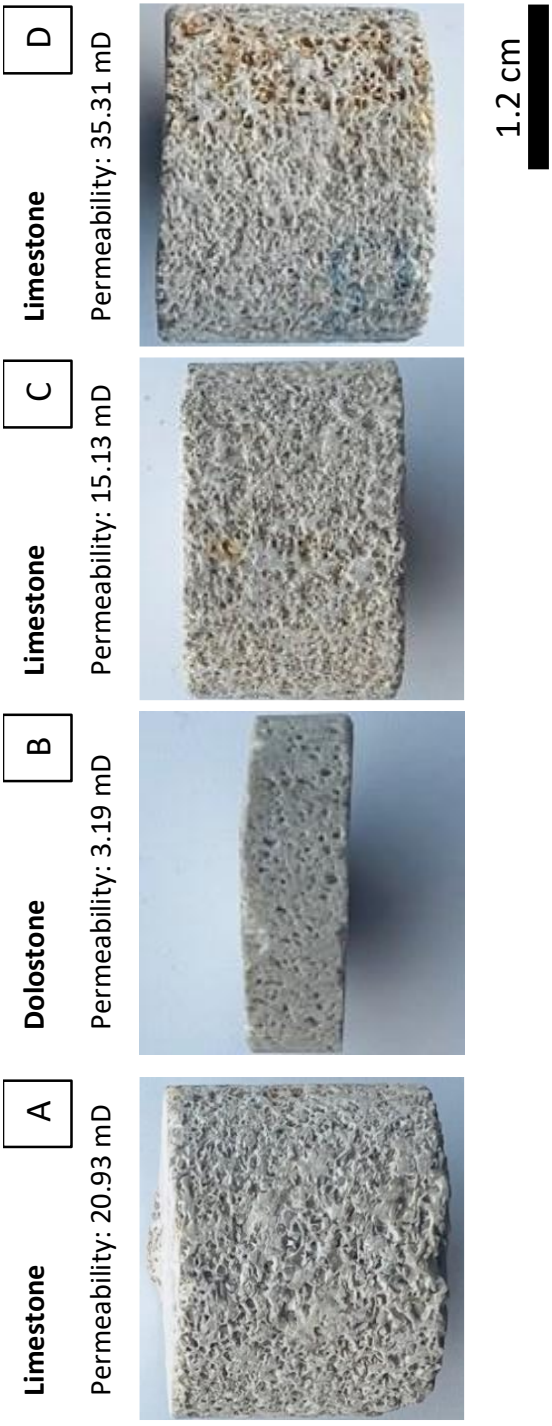

Fig. 4.1. Rock samples (A-D) used in this study along with respective permeability measured in each sample.

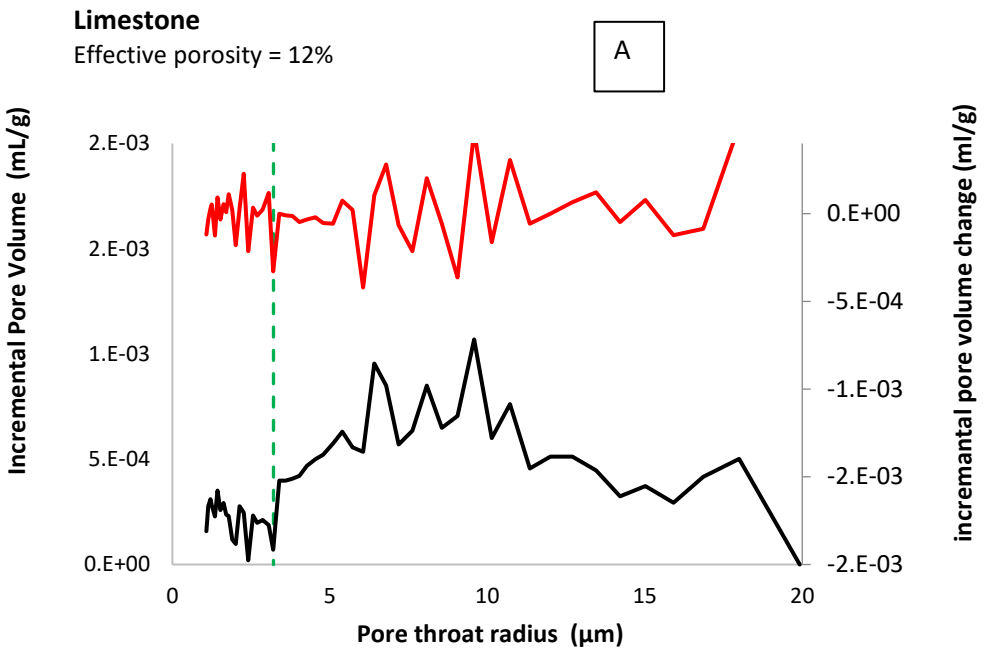
Limestone
Effective porosity = 12%
A
Incremental Pore Volume (mL/g)
2.E-03
2.E-03
1.E-03
5.E-04
0.E+00
0
5
10
15
20
Pore throat radius (µm)
0.E+00
-5.E-04
-1.E-03
-2.E-03
-2.E-03
incremantal pore volume change (ml/g)

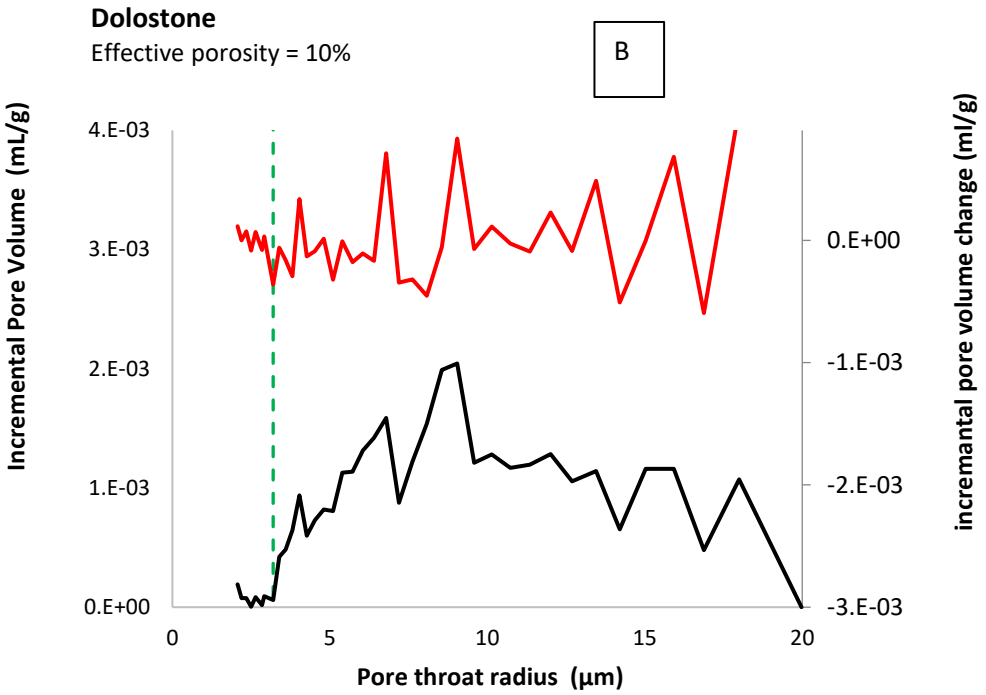
Dolostone
Effective porosity = 10%
B
Incremental Pore Volume (mL/g)
4.E-03
3.E-03
2.E-03
1.E-03
0.E+00
0
5
10
15
20
Pore throat radius (µm)
0.E+00
-1.E-03
-2.E-03
-3.E-03
incremantal pore volume change (ml/g)

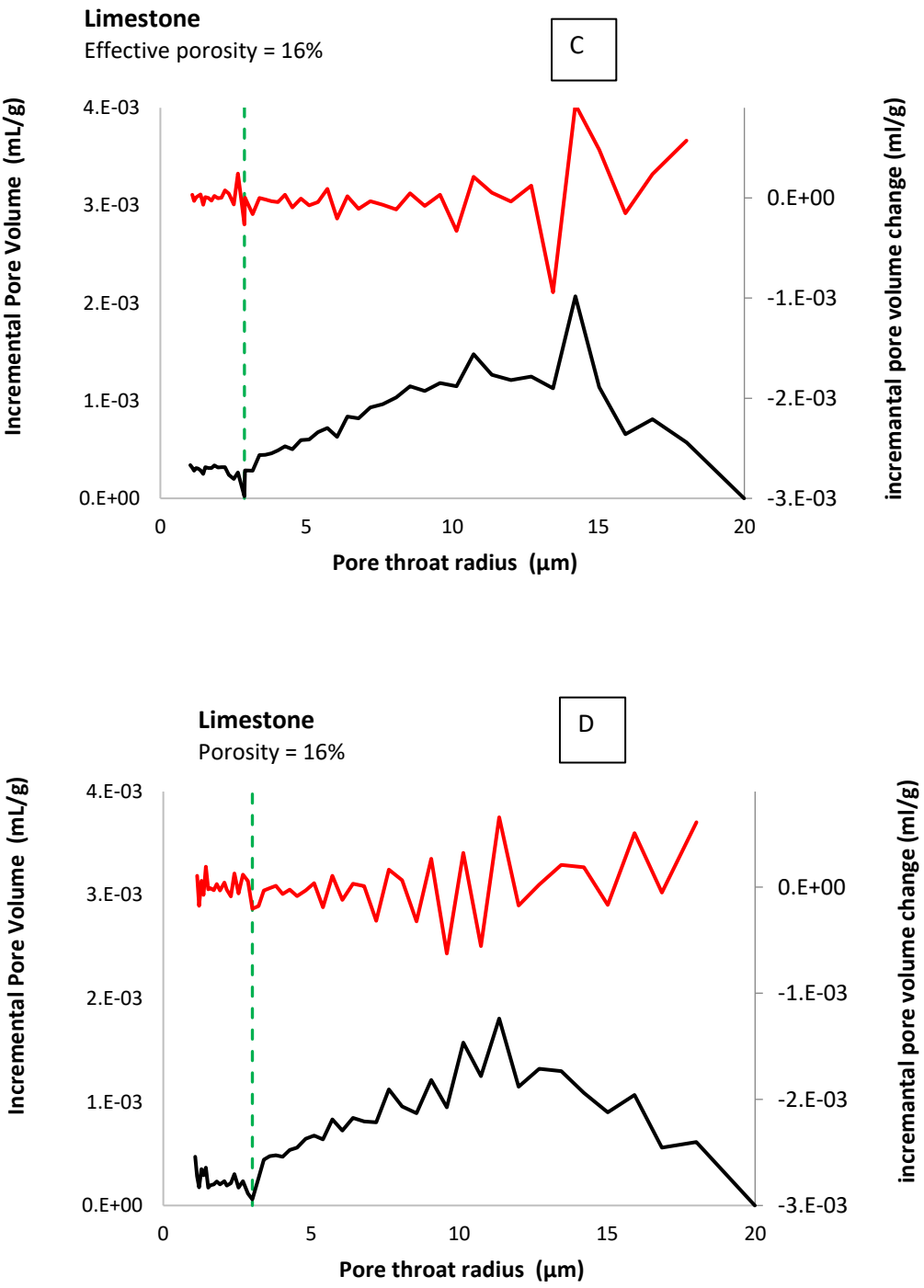

Fig. 4.2. MICP data of pore radius for study samples in Fig. 4.1. The green broken line represents MIPV, the black line is the incremental pore volume while red line is the incremental pore volume change.

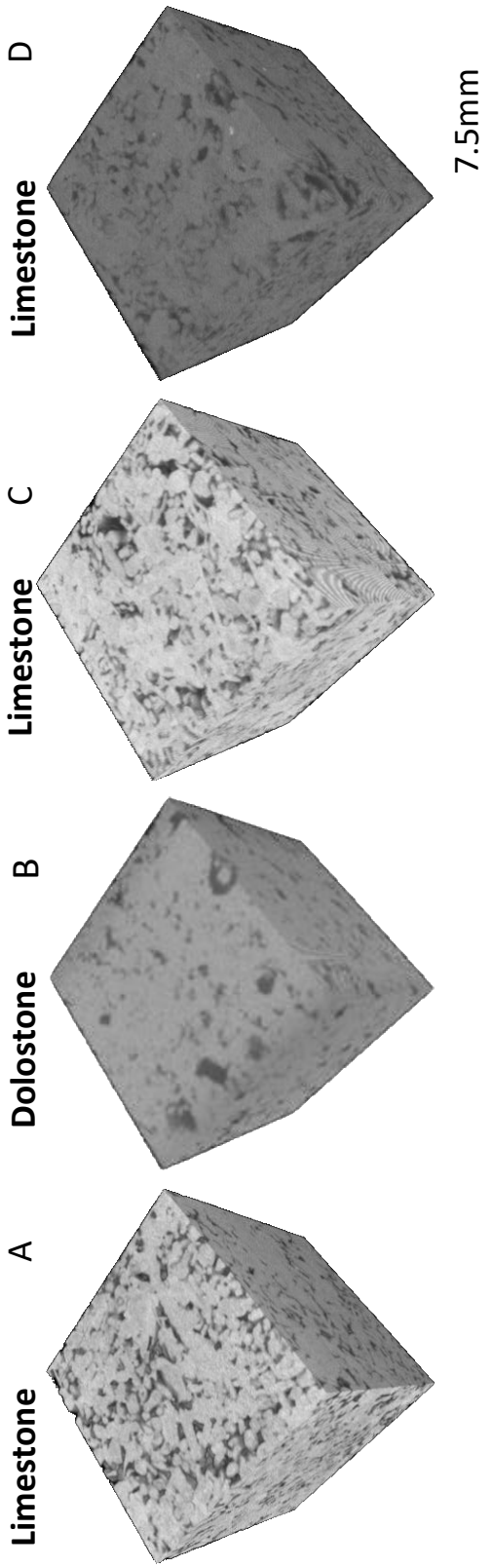

Fig. 4.3. 3D micro-CT images of the four carbonate samples (A-D) used in this study.

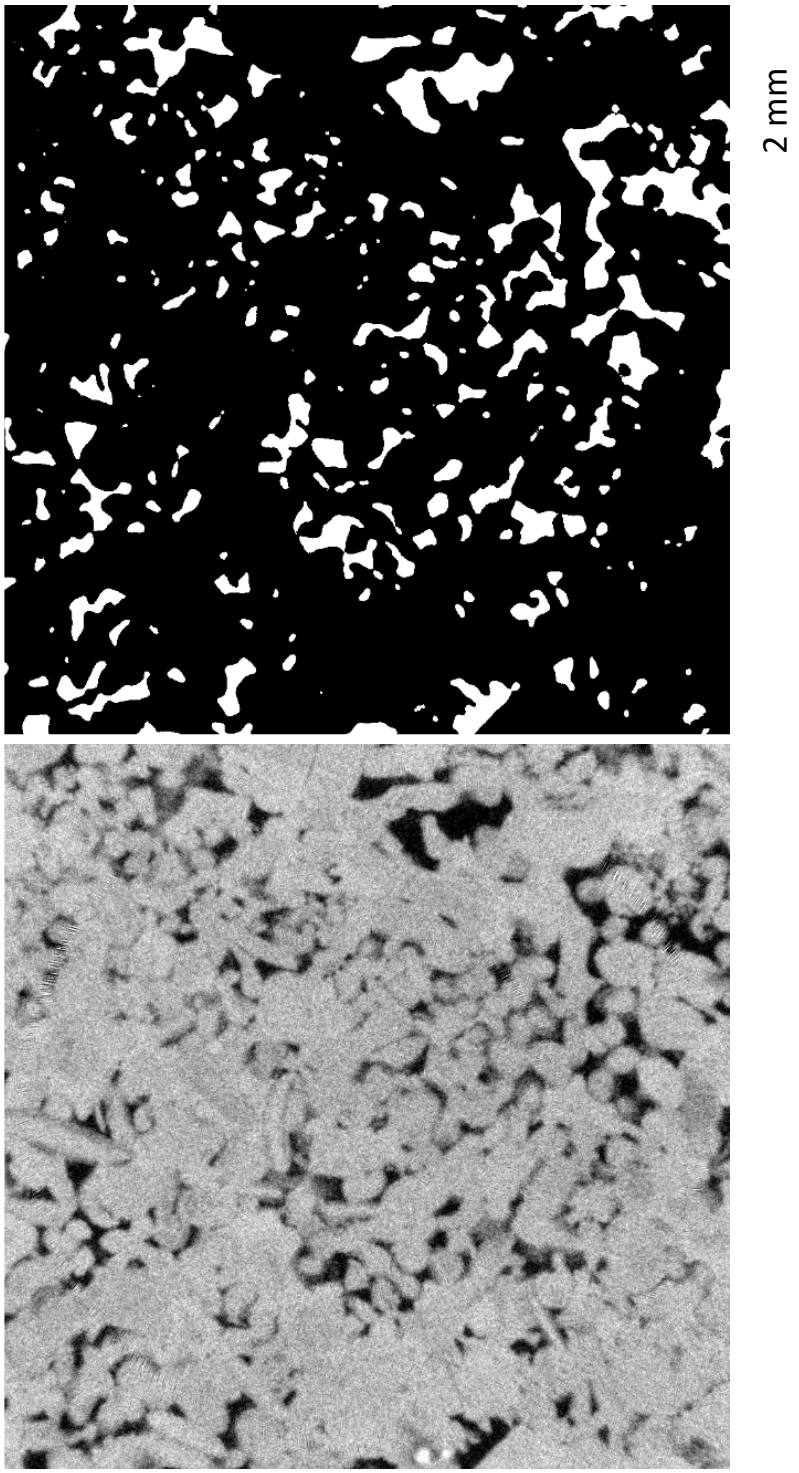

Fig. 4.4. (a) A 2D slice through unprocessed micro-CT image of sample A. (b) A 2D slice through segmented micro-CT image of sample A.

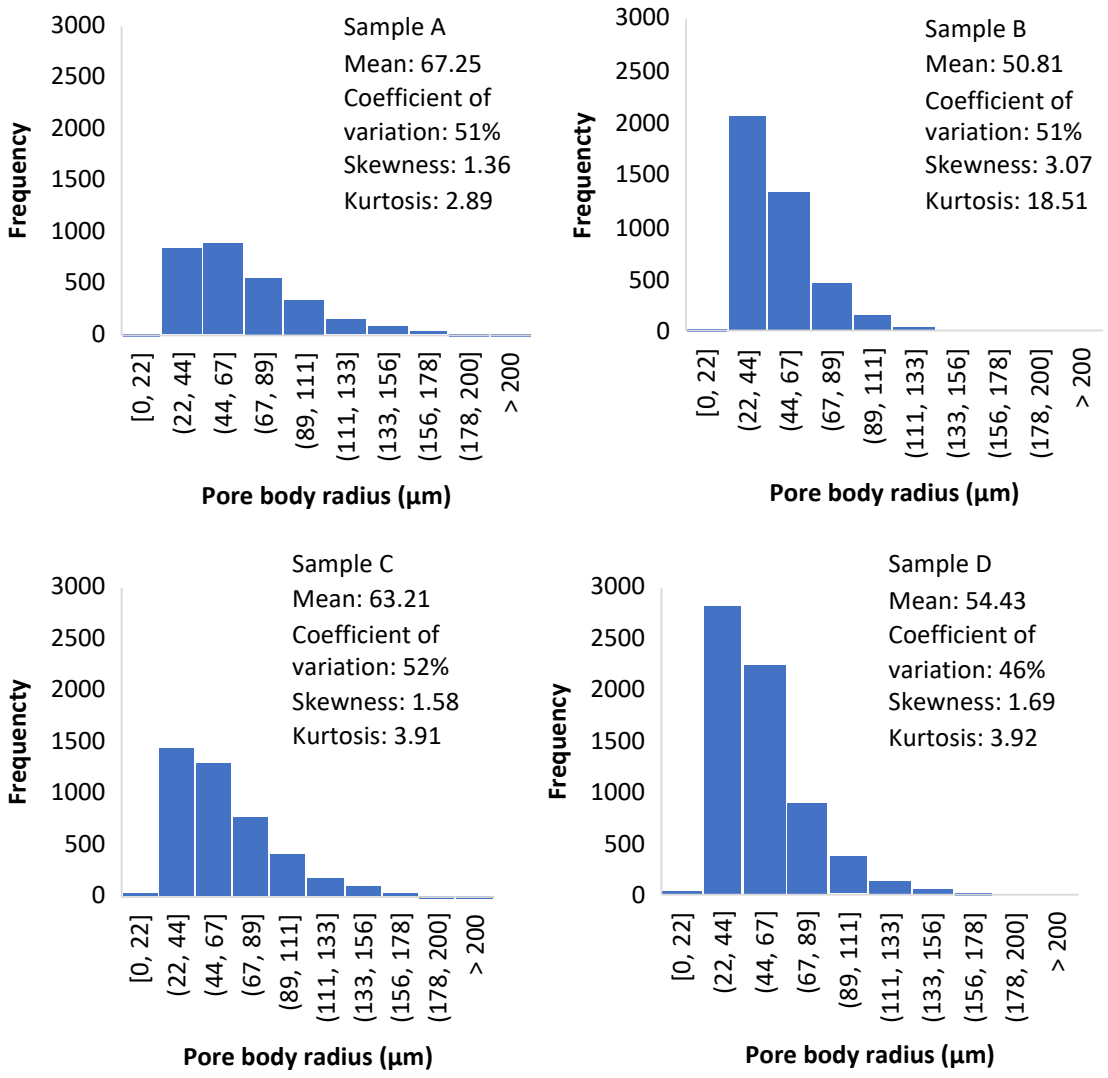

Fig. 4.5. Pore size distribution (PSD) of all samples micro-CT images (Fig. 4.3).

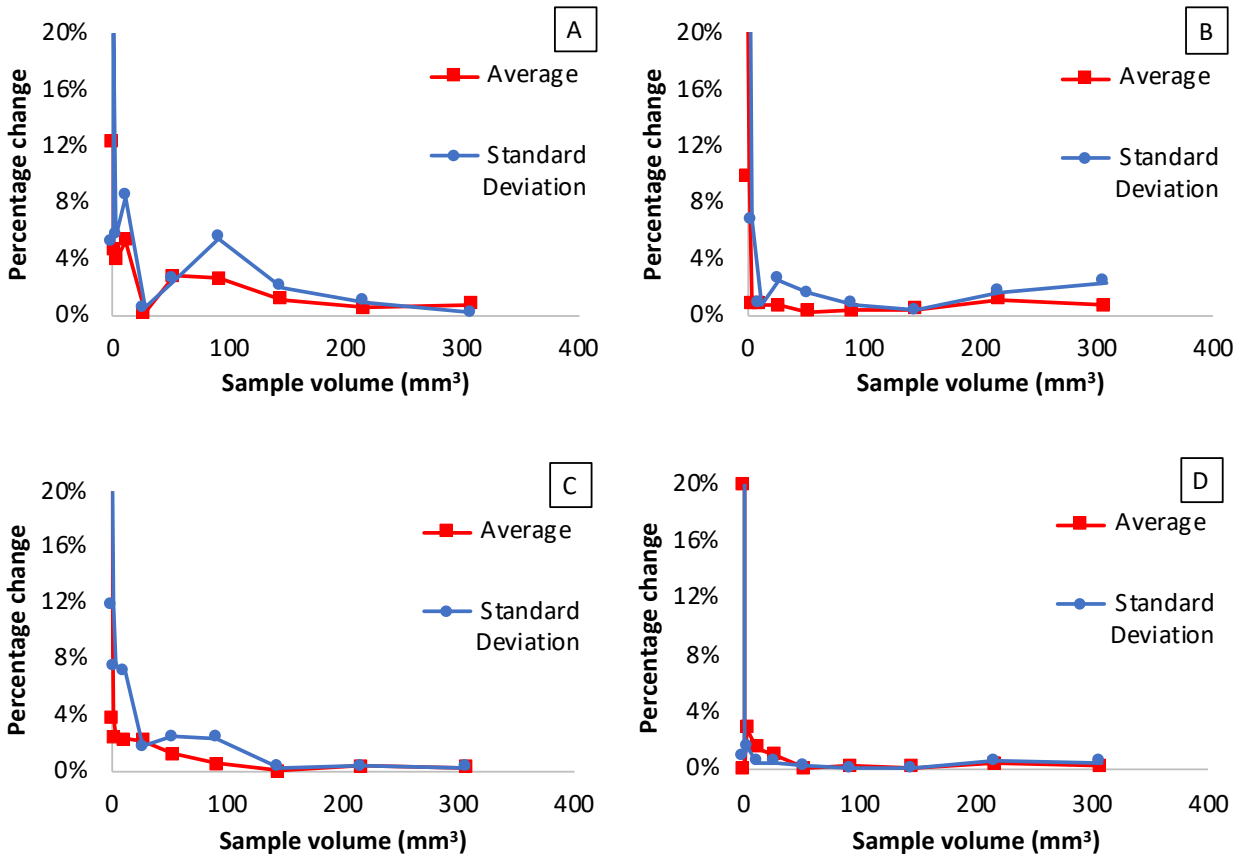

Fig. 4.6. Percentage changes in average, standard deviation, and skewness of PSD. (A) – (D) corresponds to rock samples A, B, C, and D.

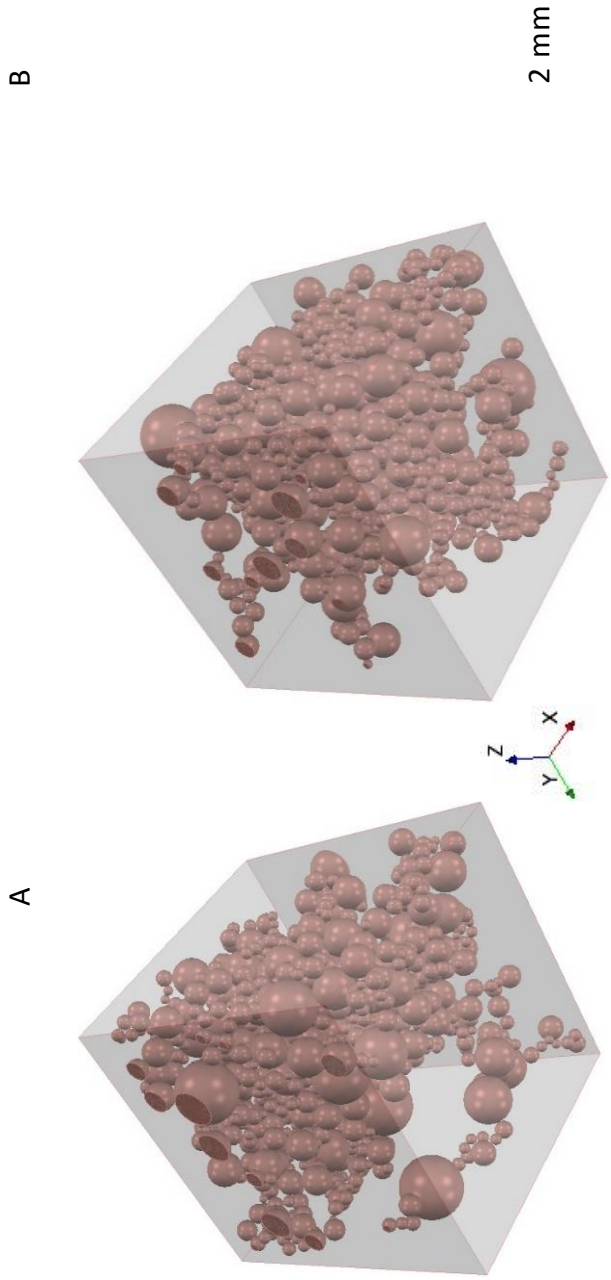

Fig. 4.7. (a) and (b) show two stochastic pore-microstructural models of sample D. (b) is zoomed in to reveal the pore throat pore body relationship.

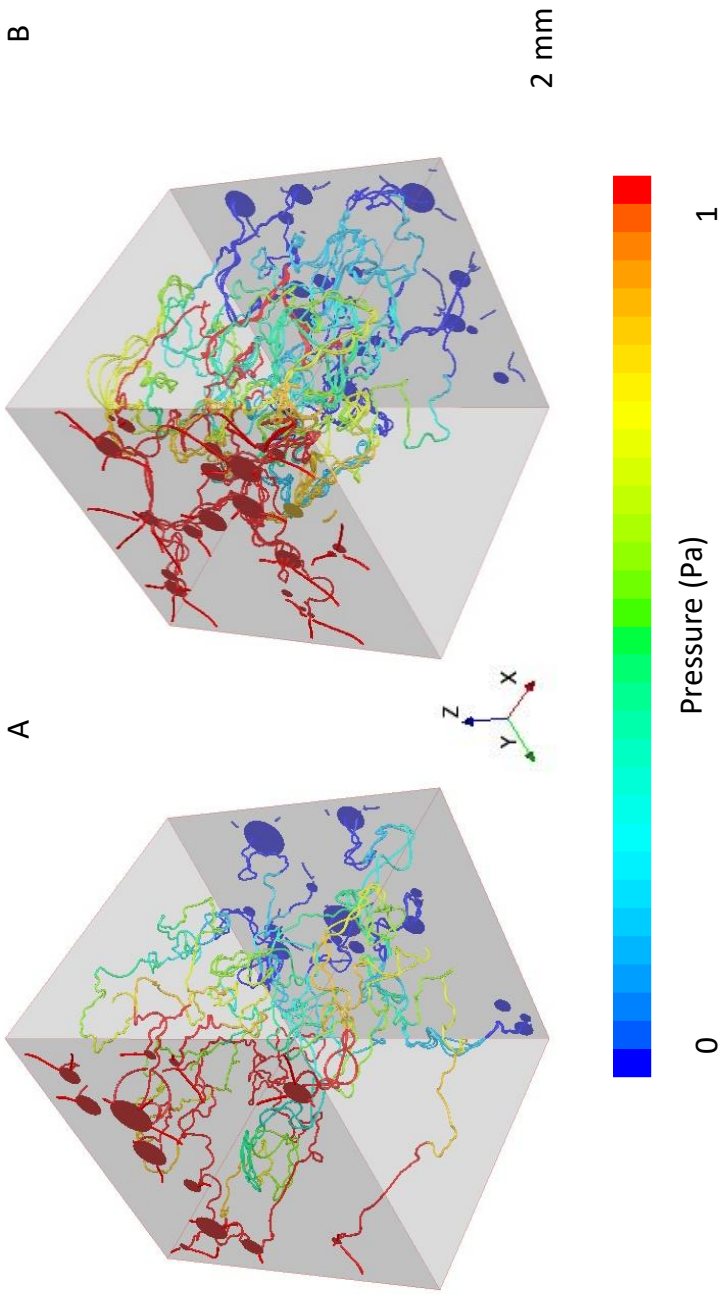

Fig. 4.8. Pressure distribution superimposed on principal flow paths through the pore-microstructural models in Fig. 4.7 at steady state. Flow in the image is in the positive X direction.

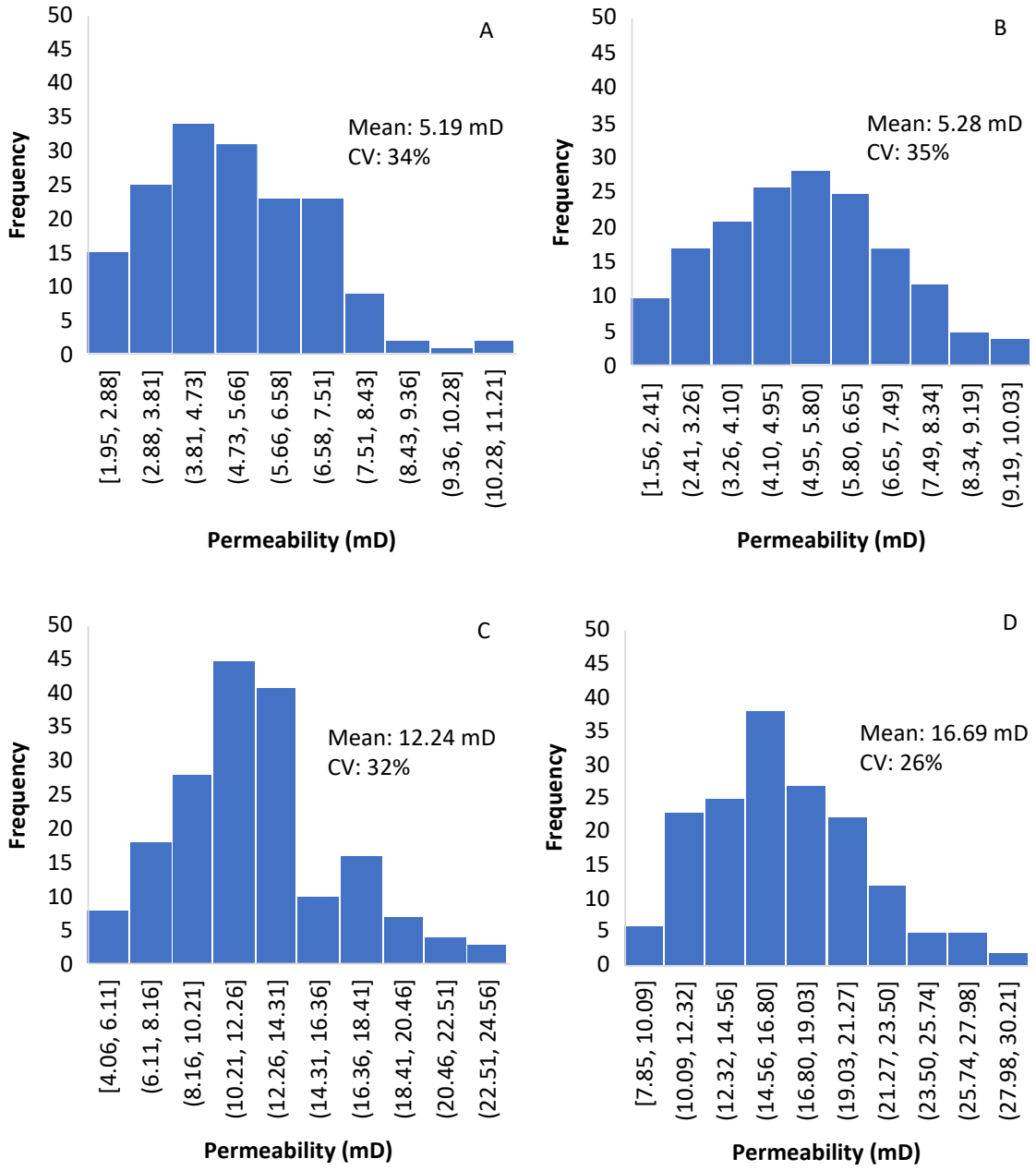

Fig. 4.9. Permeability distribution across respective samples.

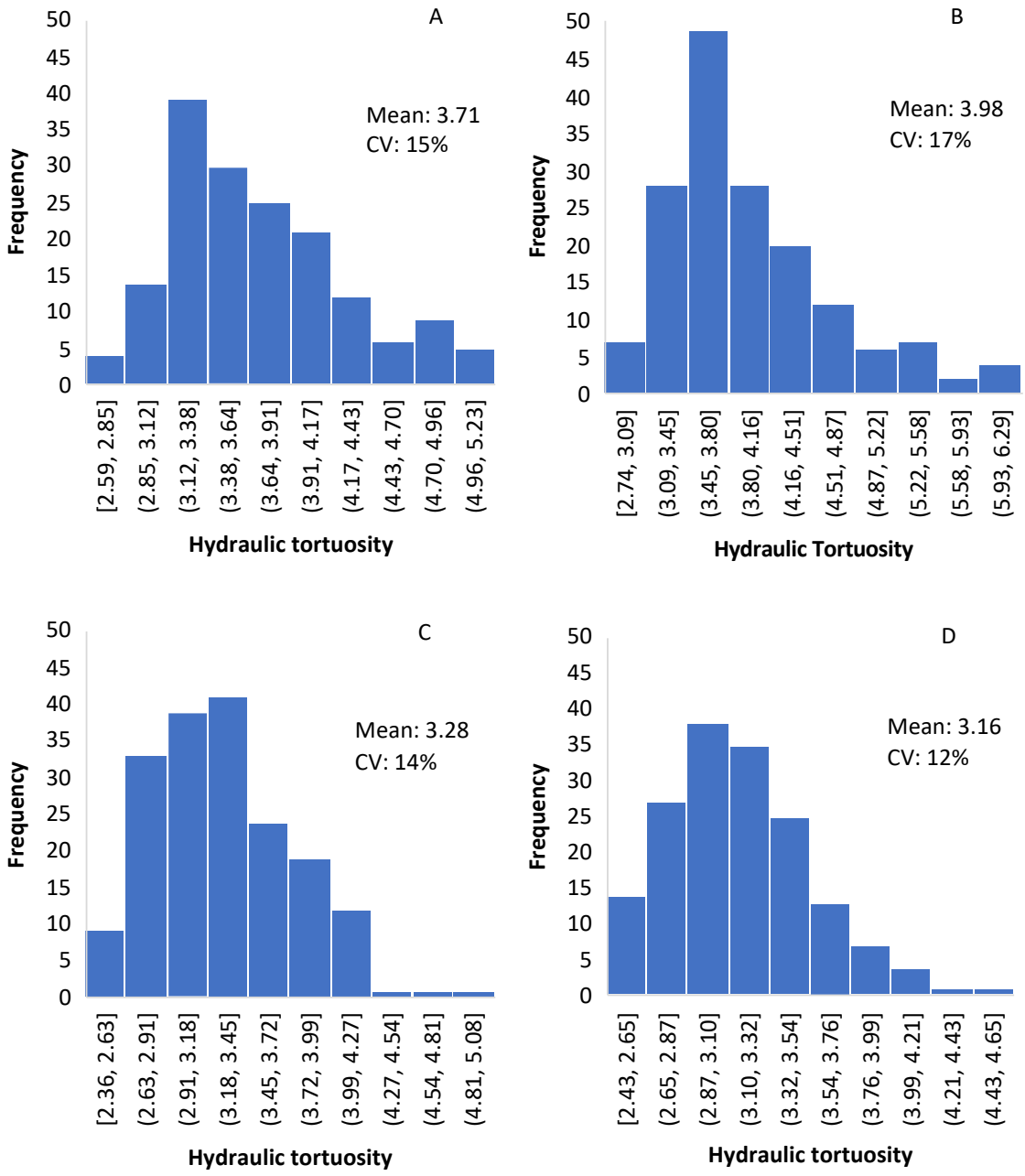

Fig. 4.10. Hydraulic tortuosity distribution across respective samples.

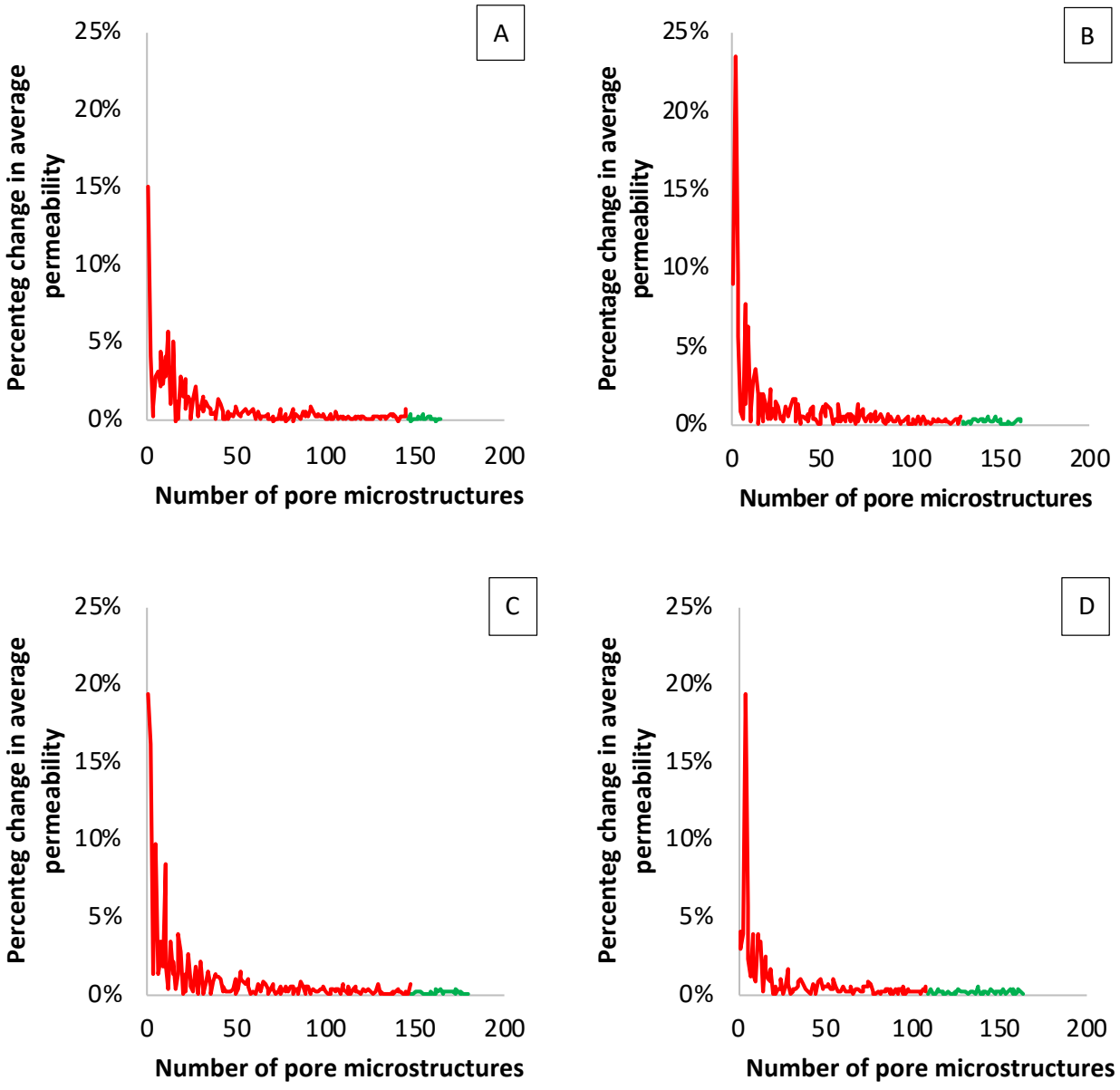

Fig. 4.11. Percentage change in average permeability with number of pore-scale simulated permeability. Red portion of the plot is deemed unrepresentative while green is deemed representative. Representative number of pore microstructures used to simulate permeability for (a) is 144, (b) is 128, (c) is 146, and (d) is 108.

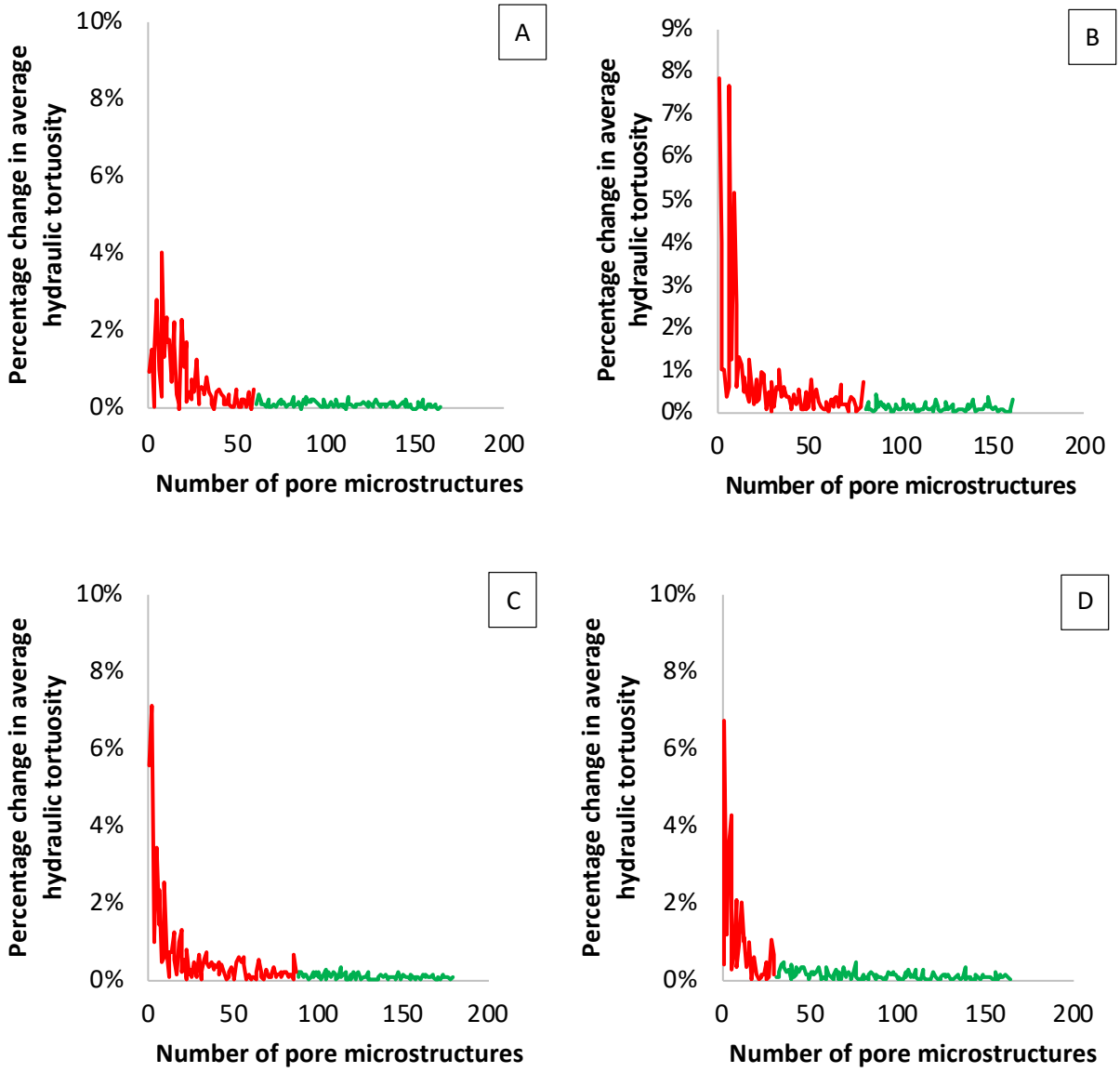

Fig. 4.12. Percentage change in average hydraulic tortuosity with pore-scale simulated hydraulic tortuosity. Red portion of the plot is deemed unrepresentative while green is deemed representative. Representative number of pore microstructures used to simulate hydraulic conductivity for (a) is 61, (b) is 80, (c) is 88, and (d) is 31.

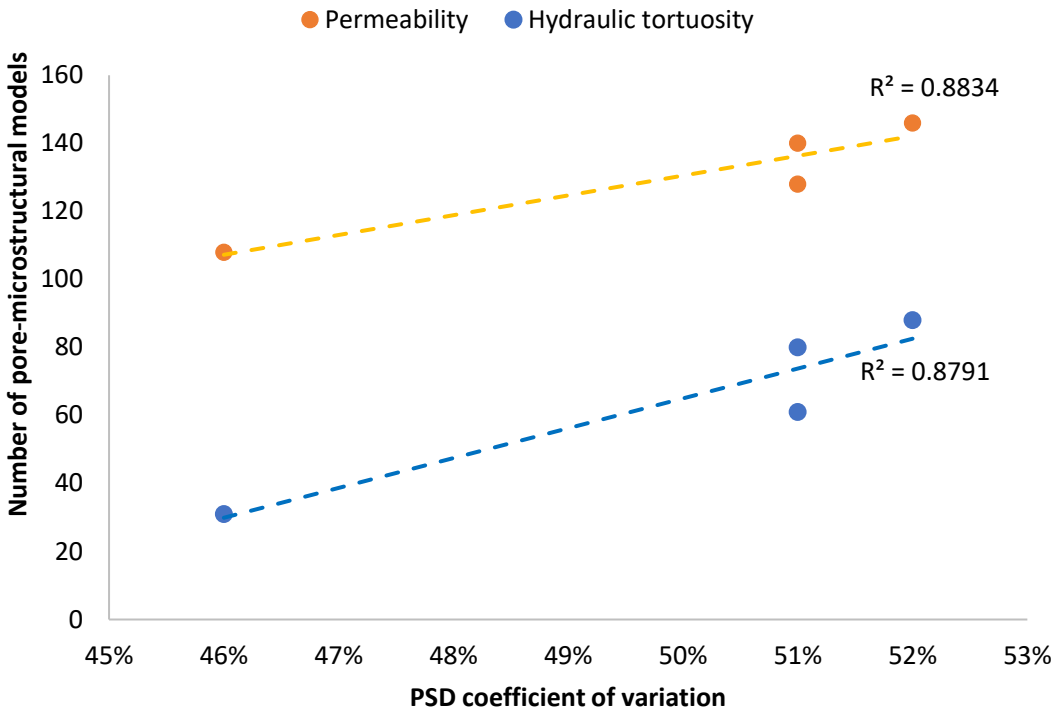

Fig. 4.13. Relationship between heterogeneity (PSD coefficient of variation) and required number of pore-microstructures to obtain representative nature of observed flow properties.

Tables

Table 4.1. EPTR of rock samples used in this study.

Sample	A	B	C	D
EPTR (μm)	7.016	7.503	7.773	7.785

Table 4.2. General properties of 200 stochastically generated 3D pore-microstructures.

Sample	Minimum number of pores	Maximum number of pores	Average digital rock volume (mm^3)	Minimum digital rock volume (mm^3)	Maximum digital rock volume (mm^3)
A	950	997	19.18	16.21	25.44
B	950	1000	11.11	8.51	16.49
C	953	998	12.76	10.60	15.10
D	951	998	7.16	6.07	8.61

Table 4.3. Statistics of cell count across generated pore-microstructural models.

Sample	Average	Minimum	Maximum
A	5,602,059	4,035,754	6,141,038
B	3,778,544	3,050,166	4,160,014
C	4,618,266	3,888,282	4,843,624
D	4,146,574	3,301,447	4,335,784

Table 4.4. Permeability measurements/ estimations using different approaches.

Permeability model approach	Sample A (mD)	Sample B (mD)	Sample C (mD)	Sample D (mD)
Experimental permeability	20.96	3.19	15.13	35.31
Winland (S. Kolodzie, 1980)	9.29	68.75	46.16	40.51
Swanson (B. Swanson, 1981)	12.68	55.93	42.19	40.02
Wells-Amaefule Method (Wells & Amaefule, 1985)	2.28	7.24	5.82	5.58
Kamath Method (Jairam Kamath, 1992)	24.29	79.41	63.41	60.8
OU Method (Rahul Dastidar, Carl H. Sondergeld, et al., 2007)	5.22	36.49	12.24	12.14
Current study	5.19	5.28	12.24	16.69

Table 4.5. Mean absolute percentage error (MAPE) of current study compared to five other approaches to estimating permeability.

Permeability model approach	Percentage error				MAPE (%)
	Sample A (%)	Sample B (%)	Sample C (%)	Sample D (%)	
Winland (S. Kolodzie, 1980)	56	2055	205	15	583
Swanson (B. Swanson, 1981)	40	1653	179	13	471
Wells-Amaefule Method (Wells & Amaefule, 1985)	89	127	62	84	90
Kamath Method (Jairam Kamath, 1992)	16	2389	319	72	699
OU Method (Rahul Dastidar, Carl H. Sondergeld, et al., 2007)	75	1044	19	66	301
Current study	75	66	19	53	53

CHAPTER V

CONCLUSION

In the first phase of this research, a novel stochastic pore-scale simulation approach was used to investigate the effect of stochastic pore connectivity on the permeability and hydraulic tortuosity of heterogeneous porous media, specifically carbonate rocks. The creation of multiple pore microstructures with pore connectivity as the only varying factor allows for an explicit analysis of the role of pore connectivity on flow without any other intervening factors. The study discovered that as heterogeneity increases in porous media, the permeability distribution shifts away from the normal distribution and toward the lognormal distribution. Similarly, but to a lesser extent, hydraulic tortuosity deviates from normal distribution. As a result, as heterogeneity increases, the relationship between permeability and hydraulic tortuosity weakens. As a result, deterministic equations such as the Kozeny-Carman equation, which establishes a relationship between permeability and hydraulic tortuosity, may be less reliable when applied to highly heterogeneous rocks.

The first phase of the study also demonstrated neural network models' ability to accurately predict permeability based on pore-throats and surface area while maintaining porosity and pore size distribution constant, effectively capturing the stochastic nature of pore connectivity. However, this method failed to predict hydraulic tortuosity accurately, indicating that pore-throats and surface area are not the primary controls for this property.

When dealing with highly heterogeneous rocks, feedforward neural network models provided better predictions for permeability and hydraulic tortuosity than models that rely solely on porosity and/or pore size distribution. The results show the benefit of using neural networks to account for the variability in permeability and hydraulic tortuosity that traditional models do not account for.

The stochastic pore-scale simulation approach was used in the second phase of the study to predict the permeability of nine core plugs obtained from both carbonate and siliciclastic sources. The stochastic pore-scale simulation approach was found to be more accurate in predicting permeability than five well-known deterministic model equations used in this study. The Gradient Boosting algorithm was used to reduce the computational cost of the stochastic pore-scale simulation approach. The number of simulations required to obtain the representative permeability of all nine core plugs was reduced from 4,400 to 28, significantly reducing the required computational resources and time.

In the final stage of the research, we combined X-ray micro-CT data with MICP data to generate high-resolution 3D pore-microstructures. The micro-CT and MICP data used in this study were obtained on a continuum scale and cover a wide range of pore-microstructural features. We validated our pore scale modeling approach by showing that the permeabilities obtained by upscaling our pore-scale simulations match measured results better than five established empirical models.

We contend that angular or irregular shaped pores, rather than spherical pores, are more effective at capturing essential concepts in multiphase flows. We are currently testing the use of generative-AI in reconstructing pore microstructures with realistic pore shapes to achieve this with minimal computational complexity. The workflows presented in this

dissertation can aid in the development of models that improve understanding of pore scale mechanisms and evaluations of their impact on fluid flow and reactive transport processes at the pore and continuum scales. This has far-reaching implications in fields such as geological carbon storage, resource exploration and production, subsurface environment management, environmental protection, and groundwater exploration.

REFRENCES

Adeleye, J. O., & Akanji, L. T. (2017). Pore-scale analyses of heterogeneity and representative elementary volume for unconventional shale rocks using statistical tools. *Journal of Petroleum Exploration and Production Technology*, *8*(3), 753-765. https://doi.org/10.1007/s13202-017-0377-4

Al Khalifah, H., Glover, P. W. J., & Lorinczi, P. (2020). Permeability prediction and diagenesis in tight carbonates using machine learning techniques. *Marine and Petroleum Geology*, *112*, 104096.

Algive, L., Békri, S., Nader, F. H., Lerat, O., & Vizika, O. (2012). Impact of Diagenetic Alterations on the Petrophysical and Multiphase Flow Properties of Carbonate Rocks Using a Reactive Pore Network Modeling Approach [10.2516/ogst/2011171]. *Oil Gas Sci. Technol. – Rev. IFP Energies nouvelles*, *67*(1), 147-160. https://doi.org/10.2516/ogst/2011171

Anovitz, L. M., & Cole, D. R. (2015). Characterization and analysis of porosity and pore structures. *Reviews in Mineralogy and geochemistry*, *80*(1), 61-164.

Apostolopoulou, M., Dusterhoft, R., Day, R., Stamatakis, M., Coppens, M.-O., & Striolo, A. (2019). Estimating permeability in shales and other heterogeneous porous media: Deterministic vs. stochastic investigations. *International Journal of Coal Geology*, *205*, 140-154. https://doi.org/https://doi.org/10.1016/j.coal.2019.02.009

Basan, P. B., Lowden, B. D., Whattler, P. R., & Attard, J. J. (1997). Pore-size data in petrophysics: a perspective on the measurement of pore geometry. *Geological Society, London, Special Publications*, *122*(1), 47-67.

Baychev, T. G., Jivkov, A. P., Rabbani, A., Raeini, A. Q., Xiong, Q., Lowe, T., & Withers, P. J. (2019). Reliability of Algorithms Interpreting Topological and Geometric Properties of Porous Media for Pore Network Modelling. *Transport in Porous Media*, *128*(1), 271-301. https://doi.org/10.1007/s11242-019-01244-8

Bazaikin, Y., Gurevich, B., Iglauer, S., Khachkova, T., Kolyukhin, D., Lebedev, M., Lisitsa, V., & Reshetova, G. (2017). Effect of CT image size and resolution on the accuracy of rock property estimates. *Journal of Geophysical Research: Solid Earth*, *122*(5), 3635-3647. https://doi.org/10.1002/2016jb013575

Bear, J. (1972). *Dynamics of Fluids in Porous Media*. Dover Publications.

Beisman, J. J., Maxwell, R. M., Navarre-Sitchler, A. K., Steefel, C. I., & Molins, S. (2015). ParCrunchFlow: an efficient, parallel reactive transport simulation tool for physically and chemically heterogeneous saturated subsurface environments. *Computational Geosciences*, *19*(2), 403-422. https://doi.org/10.1007/s10596-015-9475-x

Bernabé, Y., Li, M., & Maineult, A. (2010). Permeability and pore connectivity: A new model based on network simulations. *Journal of Geophysical Research*, *115*(B10). https://doi.org/10.1029/2010jb007444

Bhatti, A. A., Ismail, A., Raza, A., Gholami, R., Rezaee, R., Nagarajan, R., & Saffou, E. (2020). Permeability prediction using hydraulic flow units and electrofacies analysis. *Energy Geoscience*, *1*(1-2), 81-91. https://doi.org/10.1016/j.engeos.2020.04.003

Bijeljic, B., Mostaghimi, P., & Blunt, M. J. (2013). Insights into non-Fickian solute transport in carbonates. *Water Resour Res*, *49*(5), 2714-2728. https://doi.org/10.1002/wrcr.20238

Blunt, M. J., Bijeljic, B., Dong, H., Gharbi, O., Iglauer, S., Mostaghimi, P., Paluszny, A., & Pentland, C. (2013). Pore-scale imaging and modelling. *Advances in Water Resources*, *51*, 197-216. https://doi.org/10.1016/j.advwatres.2012.03.003

Cai, J., Zhang, Z., Wei, W., Guo, D., Li, S., & Zhao, P. (2019). The critical factors for permeability-formation factor relation in reservoir rocks: Pore-throat ratio, tortuosity and connectivity. *Energy*, *188*. https://doi.org/10.1016/j.energy.2019.116051

Cardwell, W. T., & Parsons, R. L. (1945). Average permeabilities of heterogeneous oil sands [Article]. *Trans. Am. Inst. Min. Metall. Pet. Eng.*, *160*(1), 34-42. https://www.scopus.com/inward/record.uri?eid=2-s2.0-0002430574&partnerID=40&md5=f32e84e043405ca0fa83ea80b58ff172

Carman, P. C. (1937). Fluid flow through a granular bed. *Trans. Inst. Chem. Eng. London*, *15*, 150-156.

Chen, S., & Doolen, G. D. (1998). LATTICE BOLTZMANN METHOD FOR FLUID FLOWS. *Annual Review of Fluid Mechanics*, *30*(1), 329-364. https://doi.org/10.1146/annurev.fluid.30.1.329

Chen, Y., Shen, C., Lu, P., & Huang, Y. (2015). Role of pore structure on liquid flow behaviors in porous media characterized by fractal geometry. *Chemical Engineering and Processing: Process Intensification*, *87*, 75-80.

Cheng, Z., Ning, Z., Wang, Q., Zeng, Y., Qi, R., Huang, L., & Zhang, W. (2019). The effect of pore structure on non-Darcy flow in porous media using the lattice Boltzmann method. *Journal of Petroleum Science and Engineering*, *172*, 391-400. https://doi.org/https://doi.org/10.1016/j.petrol.2018.09.066

Choquette, P. W., & Pray, L. C. (1970). Geologic nomenclature and classification of porosity in sedimentary carbonates. *AAPG Bulletin*, *54*(2), 207-250.

Chorin, A. J. (1968). Numerical solution of the navier-stokes equations [Article]. *Mathematics of Computation*, *22*(104), 745-762. https://doi.org/10.1090/S0025-5718-1968-0242392-2

Civan, F. (2002). Relating permeability to pore connectivity using a power-law flow unit equation. *Petrophysics*, *43*(06).

Clennell, M. B. (1997). Tortuosity: a guide through the maze. *Geological Society, London, Special Publications*, *122*(1), 299-344.

Coates, G., & Denoo, S. (1981). The producibility answer product. *The Technical Review*, *29*(2), 54-63.

Comisky, J. T., Newsham, K. E., Rushing, J. A., & Blasingame, T. A. (2007). *A Comparative Study of Capillary-Pressure-Based Empirical Models for Estimating Absolute Permeability in Tight Gas Sands*

Coskun, S. B., & Wardlaw, N. C. (1993). Estimation of permeability from image analysis of reservoir sandstones. *Journal of Petroleum Science and Engineering*, *10*(1), 1-16.

Darcy, H. (1856). *Les fontaines publiques de la ville de Dijon: Exposition et application des principes à suivre et des formules à employer dans les questions de distribution d'eau: Ouvrage terminé par un appendice relatif aux fournitures d'eau de plusieurs villes, au filtrage des eaux et à la fabrication des tuyaux de fonte, de plomb, de tôle et de bitume* (Vol. 2). V. Dalmont.

Dasgupta, T., & Mukherjee, S. (2020). *Sediment compaction and applications in petroleum geoscience.* Springer International Publishing.

Dastidar, R., Sondergeld, C. H., & Rai, C. S. (2007). An improved empirical permeability estimator from mercury injection for tight clastic rocks. *Petrophysics-The SPWLA Journal of Formation Evaluation and Reservoir Description*, *48*(03).

Dastidar, R., Sondergeld, C. H., & Rai, C. S. (2007). An improved empirical permeability estimator from mercury injection for tight clastic rocks. *Petrophysics (Houston, Tex.)*, *48*(3), 186-190.

Dastidar, R., Sondergeld, C. H., & Rai, C. S. (2007). An improved empirical permeability estimator from mercury injection for tight clastic rocks. *Petrophysics*, *48*(3), 186-190.
De Myttenaere, A., Golden, B., Le Grand, B., & Rossi, F. (2016). Mean absolute percentage error for regression models. *Neurocomputing*, *192*, 38-48.
Devarapalli, R. S., Islam, A., Faisal, T. F., Sassi, M., & Jouiad, M. (2017). Micro-CT and FIB–SEM imaging and pore structure characterization of dolomite rock at multiple scales. *Arabian Journal of Geosciences*, *10*(16). https://doi.org/10.1007/s12517-017-3120-z
Ding, B., Li, C., Zhang, M., Ji, F., & Dong, X. (2015). Effects of pore size distribution and coordination number on the prediction of filtration coefficients for straining from percolation theory. *Chemical Engineering Science*, *127*, 40-51. https://doi.org/https://doi.org/10.1016/j.ces.2015.01.012
Duda, A., Koza, Z., & Matyka, M. (2011). Hydraulic tortuosity in arbitrary porous media flow. *Physical Review E*, *84*(3), 036319. https://doi.org/10.1103/PhysRevE.84.036319
Dutton, S. P., & Loucks, R. G. (2010). Diagenetic controls on evolution of porosity and permeability in lower Tertiary Wilcox sandstones from shallow to ultradeep (200–6700 m) burial, Gulf of Mexico Basin, USA. *Marine and Petroleum Geology*, *27*(1), 69-81.
Ebrahimi, P., & Vilcáez, J. (2018a). Effect of brine salinity and guar gum on the transport of barium through dolomite rocks: Implications for unconventional oil and gas wastewater disposal. *Journal of environmental management*, *214*, 370-378. https://doi.org/10.1016/j.jenvman.2018.03.008
Ebrahimi, P., & Vilcáez, J. (2018b). Petroleum produced water disposal: Mobility and transport of barium in sandstone and dolomite rocks. *The Science of the total environment*, *634*, 1054-1063. https://doi.org/10.1016/j.scitotenv.2018.04.067
Ebrahimi, P., & Vilcáez, J. (2019). Transport of barium in fractured dolomite and sandstone saline aquifers. *The Science of the total environment*, *647*, 323-333. https://doi.org/10.1016/j.scitotenv.2018.08.008
Elmorsy, M., El-Dakhakhni, W., & Zhao, B. (2022). Generalizable Permeability Prediction of Digital Porous Media via a Novel Multi-Scale 3D Convolutional Neural Network. *Water Resources Research*, *58*(3). https://doi.org/10.1029/2021wr031454
England, W. A. (1994). Secondary Migration and Accumulation of Hydrocarbons: Chapter 12: Part III. Processes.
Erofeev, A., Orlov, D., Ryzhov, A., & Koroteev, D. (2019). Prediction of Porosity and Permeability Alteration Based on Machine Learning Algorithms. *Transport in Porous Media*, *128*(2), 677-700. https://doi.org/10.1007/s11242-019-01265-3
Farquharson, J. I., & Wadsworth, F. B. (2018). Upscaling permeability in anisotropic volcanic systems. *Journal of Volcanology and Geothermal Research*, *364*, 35-47.
Feng, R., Balling, N., Grana, D., Dramsch, J. S., & Hansen, T. M. (2021). Bayesian Convolutional Neural Networks for Seismic Facies Classification. *IEEE Transactions on Geoscience and Remote Sensing*, *59*(10), 8933-8940. https://doi.org/10.1109/TGRS.2020.3049012
Feng, R., Grana, D., & Balling, N. (2021). Variational inference in Bayesian neural network for well-log predictionBNN for well-log prediction. *Geophysics*, *86*(3), M91-M99.
Friedman, M. (1976, 1976). Porosity, permeability, and rock mechanics-a review.
Ghadami, N., Reza Rasaei, M., Hejri, S., Sajedian, A., & Afsari, K. (2015). Consistent porosity–permeability modeling, reservoir rock typing and hydraulic flow unitization in a giant carbonate reservoir. *Journal of Petroleum Science and Engineering*, *131*, 58-69. https://doi.org/10.1016/j.petrol.2015.04.017
Ghanbarian, B., Hunt, A. G., Ewing, R. P., & Sahimi, M. (2013). Tortuosity in Porous Media: A Critical Review. *Soil Science Society of America Journal*, *77*(5), 1461-1477. https://doi.org/10.2136/sssaj2012.0435

Gostick, J. T. (2017). Versatile and efficient pore network extraction method using marker-based watershed segmentation. *Phys Rev E*, *96*(2-1), 023307. https://doi.org/10.1103/PhysRevE.96.023307

Graczyk, K. M., & Matyka, M. (2020). Predicting porosity, permeability, and tortuosity of porous media from images by deep learning. *Sci Rep*, *10*(1), 21488. https://doi.org/10.1038/s41598-020-78415-x

Hajizadeh, A., Safekordi, A., & Farhadpour, F. A. (2011). A multiple-point statistics algorithm for 3D pore space reconstruction from 2D images. *Advances in Water Resources*, *34*(10), 1256-1267. https://doi.org/10.1016/j.advwatres.2011.06.003

Harbaugh, A. W. (2005). *MODFLOW-2005, the US Geological Survey modular ground-water model: the ground-water flow process* (Vol. 6). US Department of the Interior, US Geological Survey Reston, VA, USA.

He, L., Zhao, L., Li, J., Ma, J., Lui, R., Wang, S., & Zhao, W. (2014). Complex relationship between porosity and permeability of carbonate reservoirs and its controlling factors: A case study of platform facies in Pre-Caspian Basin. *Petroleum Exploration and Development*, *41*(2), 225-234. https://doi.org/10.1016/s1876-3804(14)60026-4

Hollis, C. (2011). Diagenetic controls on reservoir properties of carbonate successions within the Albian–Turonian of the Arabian Plate. *Petroleum Geoscience*, *17*(3), 223-241. https://doi.org/10.1144/1354-079310-032

Huang, J., Jin, T., Chai, Z., Barrufet, M., & Killough, J. (2019). Compositional simulation of fractured shale reservoir with distribution of nanopores using coupled multi-porosity and EDFM method. *Journal of Petroleum Science and Engineering*, *179*, 1078-1089.

Huang, X., Zhou, W., & Deng, D. (2020). Validation of pore network modeling for determination of two-phase transport in fibrous porous media [Article]. *Scientific Reports*, *10*(1), Article 20852. https://doi.org/10.1038/s41598-020-74581-0

Hulea, I. N., & Nicholls, C. A. (2012). Carbonate rock characterization and modeling: Capillary pressure and permeability in multimodal rocks—A look beyond sample specific heterogeneity. *AAPG Bulletin*, *96*(9), 1627-1642. https://doi.org/10.1306/02071211124

Ishola, O., Alexander, A., & Vilcáez, J. (2022). Statistical and neural network analysis of the relationship between the stochastic nature of pore connectivity and flow properties of heterogeneous rocks. *Journal of Natural Gas Science and Engineering*, *105*. https://doi.org/10.1016/j.jngse.2022.104719

Ishola, O., & Vilcáez, J. (2022). Machine learning modeling of permeability in 3D heterogeneous porous media using a novel stochastic pore-scale simulation approach. *Fuel*, *321*. https://doi.org/10.1016/j.fuel.2022.124044

Jiang, C., Zhang, D., & Chen, S. (2021). Lithology identification from well-log curves via neural networks with additional geologic constraintLithology identification from well logs. *Geophysics*, *86*(5), IM85-IM100.

Jivkov, A. P., Hollis, C., Etiese, F., McDonald, S. A., & Withers, P. J. (2013). A novel architecture for pore network modelling with applications to permeability of porous media. *Journal of Hydrology*, *486*, 246-258. https://doi.org/10.1016/j.jhydrol.2013.01.045

Jivkov, A. P., & Xiong, Q. (2014). A Network Model for Diffusion in Media with Partially Resolvable Pore Space Characteristics. *Transport in Porous Media*, *105*(1), 83-104. https://doi.org/10.1007/s11242-014-0360-1

Kamath, J. (1992). Evaluation of Accuracy of Estimating Air Permeability from Mercury Injection Data. *SPE Formation Evaluation*, *7*(4), 304-310. https://doi.org/https://doi.org/10.2118/18181-PA

Kamath, J. (1992). Evaluation of accuracy of estimating air permeability from mercury-injection data. *SPE Formation evaluation*, *7*(04), 304-310.

Kenyon, W., Day, P., Straley, C., & Willemsen, J. (1988). A three-part study of NMR longitudinal relaxation properties of water-saturated sandstones. *SPE Formation evaluation*, *3*(03), 622-636.
Kenyon, W. E. (1992). Nuclear magnetic resonance as a petrophysical measurement [Article]. *Nuclear Geophysics*, *6*(2), 153-171. https://www.scopus.com/inward/record.uri?eid=2-s2.0-0027007457&partnerID=40&md5=6fbbff9b984eabd941969c58614308cc
Kimura, M. (2018). Prediction of tortuosity, permeability, and pore radius of water-saturated unconsolidated glass beads and sands. *The Journal of the Acoustical Society of America*, *143*(5), 3154-3168. https://doi.org/10.1121/1.5039520
Kingma, D. P., & Ba, J. (2014). Adam: A method for stochastic optimization. *arXiv preprint arXiv:1412.6980*.
Klobes, P., Riesemeier, H., Meyer, K., Goebbels, J., & Hellmuth, K. H. (1997). Rock porosity determination by combination of X-ray computerized tomography with mercury porosimetry [Article]. *Fresenius' Journal of Analytical Chemistry*, *357*(5), 543-547. https://doi.org/10.1007/s002160050210
Knackstedt, M., Arns, C., Ghous, A., Sakellariou, A., Senden, T., Sheppard, A., Sok, R., Nguyen, V. H., & Pinczewski, W. V. (2006). *3D imaging and characterization of the pore space of carbonate core; implications to single and two phase flow properties* SPWLA 47th Annual Logging Symposium, Veracruz, Mexico.
Kohanpur, A. H., Chen, Y., & Valocchi, A. J. (2022). Using direct numerical simulation of pore-level events to improve pore-network models for prediction of residual trapping of CO2. *Frontiers in Water*, *3*, 710160.
Kolodzie, S. (1980). Analysis of pore throat size and use of the Waxman-Smits equation to determine OOIP in Spindle Field, Colorado. SPE annual technical conference and exhibition,
Kolodzie, S., Jr. (1980). Analysis of Pore Throat Size and Use of The Waxman-Smits Equation To Determine Ooip In Spindle Field, Colorado. *SPE Annual Technical Conference and Exhibition: Dallas, Texas, Society of Petroleum Engineers*, 10.
Konangi, S., Palakurthi, N. K., Karadimitriou, N. K., Comer, K., & Ghia, U. (2021). Comparison of pore-scale capillary pressure to macroscale capillary pressure using direct numerical simulations of drainage under dynamic and quasi-static conditions. *Advances in Water Resources*, *147*, 103792.
Kozeny, J. (1927). Uber kapillare Leitung des Wassers im Boden-Aufstieg, Versickerung und Anwendung auf die Bewasserung, Sitzungsberichte der Akademie der Wissenschaften Wien. *Mathematisch Naturwissenschaftliche Abteilung*, *136*, 271-306.
Lala, A. M. S. (2020). A novel model for reservoir rock tortuosity estimation. *Journal of Petroleum Science and Engineering*, *192*. https://doi.org/10.1016/j.petrol.2020.107321
Li, C.-X., Liu, M., & Guo, B.-C. (2019). Classification of tight sandstone reservoirs based on NMR logging. *Applied Geophysics*, *16*(4), 549-558.
Li, X., Kang, Y., & Haghighi, M. (2018). Investigation of pore size distributions of coals with different structures by nuclear magnetic resonance (NMR) and mercury intrusion porosimetry (MIP). *Measurement*, *116*, 122-128.
Liu, K., Ostadhassan, M., Sun, L., Zou, J., Yuan, Y., Gentzis, T., Zhang, Y., Carvajal-Ortiz, H., & Rezaee, R. (2019). A comprehensive pore structure study of the Bakken Shale with SANS, N2 adsorption and mercury intrusion. *Fuel*, *245*, 274-285.
Male, F., Jensen, J. L., & Lake, L. W. (2020). Comparison of permeability predictions on cemented sandstones with physics-based and machine learning approaches. *Journal of Natural Gas Science and Engineering*, *77*, 103244.
Malin, P. E., Leary, P. C., Cathles, L. M., & Barton, C. C. (2020). Observational and Critical State Physics Descriptions of Long-Range Flow Structures. *Geosciences*, *10*(2). https://doi.org/10.3390/geosciences10020050

Manwart, C., Torquato, S., & Hilfer, R. (2000). Stochastic reconstruction of sandstones [Article]. *Physical Review E - Statistical Physics, Plasmas, Fluids, and Related Interdisciplinary Topics*, *62*(1 B), 893-899. https://doi.org/10.1103/PhysRevE.62.893

Mees, F., Swennen, R., Van Geet, M., & Jacobs, P. (2003). Applications of X-ray computed tomography in the geosciences. *Geological Society, London, Special Publications*, *215*(1), 1-6.

Mehmani, A., & Prodanović, M. (2014). The effect of microporosity on transport properties in porous media. *Advances in Water Resources*, *63*, 104-119. https://doi.org/10.1016/j.advwatres.2013.10.009

Mendes, R., Cortez, P., Rocha, M., & Neves, J. (2002, 2002). Particle swarms for feedforward neural network training.

Mohamad, I. B., & Usman, D. (2013). Standardization and its effects on K-means clustering algorithm. *Research Journal of Applied Sciences, Engineering and Technology*, *6*(17), 3299-3303.

Mohebbi, A., & Kaydani, H. (2015). Permeability Estimation in Petroleum Reservoir by Meta-heuristics: An Overview. In C. Cranganu, H. Luchian, & M. E. Breaban (Eds.), *Artificial Intelligent Approaches in Petroleum Geosciences* (pp. 269-285). Springer International Publishing. https://doi.org/10.1007/978-3-319-16531-8_10

Morad, S., Al-Ramadan, K., Ketzer, J. M., & De Ros, L. F. (2010). The impact of diagenesis on the heterogeneity of sandstone reservoirs: A review of the role of depositional facies and sequence stratigraphy. *AAPG Bulletin*, *94*(8), 1267-1309. https://doi.org/10.1306/04211009178

Mostaghimi, P., Blunt, M. J., & Bijeljic, B. (2013). Computations of absolute permeability on micro-CT images. *Mathematical Geosciences*, *45*, 103-125.

Munawar, M. J., Vega, S., Lin, C., Alsuwaidi, M., Ahsan, N., & Bhakta, R. R. (2021). Upscaling reservoir rock porosity by fractal dimension using three-dimensional micro-computed tomography and two-dimensional scanning electron microscope images. *Journal of Energy Resources Technology*, *143*(1).

Naraghi, M. E., & Javadpour, F. (2015). A stochastic permeability model for the shale-gas systems [Article]. *International Journal of Coal Geology*, *140*, 111-124. https://doi.org/10.1016/j.coal.2015.02.004

Niu, Q., & Zhang, C. (2018). Joint inversion of NMR and SIP data to estimate pore size distribution of geomaterials. *Geophysical Journal International*, *212*(3), 1791-1805. https://doi.org/10.1093/gji/ggx501

Okabe, H., & Blunt, M. J. (2004). Prediction of permeability for porous media reconstructed using multiple-point statistics. *Phys Rev E Stat Nonlin Soft Matter Phys*, *70*(6 Pt 2), 066135. https://doi.org/10.1103/PhysRevE.70.066135

Oostrom, M., Mehmani, Y., Romero-Gomez, P., Tang, Y., Liu, H., Yoon, H., Kang, Q., Joekar-Niasar, V., Balhoff, M. T., Dewers, T., Tartakovsky, G. D., Leist, E. A., Hess, N. J., Perkins, W. A., Rakowski, C. L., Richmond, M. C., Serkowski, J. A., Werth, C. J., Valocchi, A. J., . . . Zhang, C. (2014). Pore-scale and continuum simulations of solute transport micromodel benchmark experiments. *Computational Geosciences*, *20*(4), 857-879. https://doi.org/10.1007/s10596-014-9424-0

Ozgumus, T., Mobedi, M., & Ozkol, U. (2014). Determination of Kozeny Constant Based on Porosity and Pore to Throat Size Ratio in Porous Medium with Rectangular Rods. *Engineering Applications of Computational Fluid Mechanics*, *8*(2), 308-318. https://doi.org/10.1080/19942060.2014.11015516

Pedregosa, F., Varoquaux, G., Gramfort, A., Michel, V., Thirion, B., Grisel, O., Blondel, M., Prettenhofer, P., Weiss, R., & Dubourg, V. (2011). Scikit-learn: Machine learning in Python. *the Journal of machine Learning research*, *12*, 2825-2830.

Peng, S., Hassan, A., & Loucks, R. G. (2016). Permeability estimation based on thin-section image analysis and 2D flow modeling in grain-dominated carbonates. *Marine and Petroleum Geology*, *77*, 763-775. https://doi.org/10.1016/j.marpetgeo.2016.07.024

Peng, S., Hu, Q., Dultz, S., & Zhang, M. (2012). Using X-ray computed tomography in pore structure characterization for a Berea sandstone: Resolution effect [Article]. *Journal of Hydrology*, *472-473*, 254-261. https://doi.org/10.1016/j.jhydrol.2012.09.034

Pittman, E. D. (1992). Relationship of porosity and permeability to various parameters derived from mercury injection-capillary pressure curves for sandstone. *AAPG Bulletin*, *76*(2), 191-198.

Purcell, W. R. (1949). Capillary pressures-their measurement using mercury and the calculation of permeability therefrom. *Journal of Petroleum Technology*, *1*(02), 39-48.

Rashid, F., Glover, P. W. J., Lorinczi, P., Hussein, D., & Lawrence, J. A. (2017). Microstructural controls on reservoir quality in tight oil carbonate reservoir rocks. *Journal of Petroleum Science and Engineering*, *156*, 814-826. https://doi.org/10.1016/j.petrol.2017.06.056

Regnet, J. B., David, C., Robion, P., & Menéndez, B. (2019). Microstructures and physical properties in carbonate rocks: A comprehensive review. *Marine and Petroleum Geology*, *103*, 366-376. https://doi.org/10.1016/j.marpetgeo.2019.02.022

Sahin, A., Ali, A. Z., Saner, S., & Menouar, H. (2007). Permeability Anisotropy Distributions in an Upper Jurassic Carbonate Reservoir, Eastern Saudi Arabia. *Journal of Petroleum Geology*, *30*(2), 147-158. https://doi.org/10.1111/j.1747-5457.2007.00147.x

Saraji, S., & Piri, M. (2015). The representative sample size in shale oil rocks and nano-scale characterization of transport properties. *International Journal of Coal Geology*, *146*, 42-54. https://doi.org/10.1016/j.coal.2015.04.005

Saxena, N., Hows, A., Hofmann, R., Alpak, F. O., Dietderich, J., Appel, M., Freeman, J., & De Jong, H. (2019). Rock properties from micro-CT images: Digital rock transforms for resolution, pore volume, and field of view. *Advances in Water Resources*, *134*. https://doi.org/10.1016/j.advwatres.2019.103419

Saxena, N., Hows, A., Hofmann, R., O. Alpak, F., Freeman, J., Hunter, S., & Appel, M. (2018). Imaging and computational considerations for image computed permeability: Operating envelope of Digital Rock Physics. *Advances in Water Resources*, *116*, 127-144. https://doi.org/10.1016/j.advwatres.2018.04.001

Schmitt, M., Fernandes, C. P., da Cunha Neto, J. A. B., Wolf, F. G., & dos Santos, V. S. S. (2013). Characterization of pore systems in seal rocks using nitrogen gas adsorption combined with mercury injection capillary pressure techniques. *Marine and Petroleum Geology*, *39*(1), 138-149.

Shabani, B., Pashin, J., & Vilcáez, J. (2020). TOUGHREACT-CO2Bio – A new module to simulate geological carbon storage under biotic conditions (Part 2): The bio-geochemical reactive transport of CO2-CH4-H2-H2S gas mixtures. *Journal of Natural Gas Science and Engineering*, *76*, 103190. https://doi.org/10.1016/j.jngse.2020.103190

Shabani, B., & Vilcaez, J. (2019). TOUGHREACT-CO2Bio -- A new module to simulate geological carbon storage under biotic conditions : The multiphase flow of CO.sub.2-CH.sub.4-H.sub.2-H.sub.2S gas mixtures. *Journal of Natural Gas Science and Engineering*, *63*, 85. https://doi.org/10.1016/j.jngse.2019.01.013

Shabani, B., & Vilcáez, J. (2017). Prediction of CO2-CH4-H2S-N2 gas mixtures solubility in brine using a non-iterative fugacity-activity model relevant to CO2-MEOR. *Journal of petroleum science & engineering*, *150*, 162-179. https://doi.org/10.1016/j.petrol.2016.12.012

Shabani, B., & Vilcáez, J. (2019). TOUGHREACT-CO2Bio – A new module to simulate geological carbon storage under biotic conditions (Part 1): The multiphase flow of CO2-CH4-H2-H2S gas mixtures. *Journal of Natural Gas Science and Engineering*, *63*, 85-94. https://doi.org/10.1016/j.jngse.2019.01.013

Shen, R., Zhang, X., Ke, Y., Xiong, W., Guo, H., Liu, G., Zhou, H., & Yang, H. (2021). An integrated pore size distribution measurement method of small angle neutron scattering and mercury intrusion capillary pressure. *Scientific Reports*, *11*(1), 17458.

Soete, J., Claes, S., Claes, H., Janssens, N., Cnudde, V., Huysmans, M., & Swennen, R. (2017). Lattice boltzmann simulations of fluid flow in continental carbonate reservoir rocks and in upscaled rock models generated with multiple-point geostatistics [Article]. *Geofluids*, *2017*, Article 7240524. https://doi.org/10.1155/2017/7240524

Song, S., Hou, J., Dou, L., Song, Z., & Sun, S. (2020). Geologist-level wireline log shape identification with recurrent neural networks. *Computers & Geosciences*, *134*, 104313.

Starnoni, M., Pokrajac, D., & Neilson, J. E. (2017). Computation of fluid flow and pore-space properties estimation on micro-CT images of rock samples. *Computers & Geosciences*, *106*, 118-129. https://doi.org/10.1016/j.cageo.2017.06.009

Sun, H., Vega, S., & Tao, G. (2017). Analysis of heterogeneity and permeability anisotropy in carbonate rock samples using digital rock physics. *Journal of Petroleum Science and Engineering*, *156*, 419-429. https://doi.org/10.1016/j.petrol.2017.06.002

Sun, J., Dong, H., Arif, M., Yu, L., Zhang, Y., Golsanami, N., & Yan, W. (2021). Influence of pore structural properties on gas hydrate saturation and permeability: A coupled pore-scale modelling and X-ray computed tomography method. *Journal of Natural Gas Science and Engineering*, *88*. https://doi.org/10.1016/j.jngse.2021.103805

Sutera, S. P., & Skalak, R. (1993). The History of Poiseuille's Law. *Annual Review of Fluid Mechanics*, *25*(1), 1-20. https://doi.org/10.1146/annurev.fl.25.010193.000245

Swanson, B. (1981). A simple correlation between permeabilities and mercury capillary pressures. *Journal of Petroleum Technology*, *33*(12), 2498-2504.

Swanson, B. F. (1981). A Simple Correlation between Permeability and Mercury Capillary Pressures. *Journal of Petroleum Technology*, *33*(12), 2498-2504.

Tahmasebi, P., Kamrava, S., Bai, T., & Sahimi, M. (2020). Machine learning in geo- and environmental sciences: From small to large scale. *Advances in Water Resources*, *142*. https://doi.org/10.1016/j.advwatres.2020.103619

Tembely, M., AlSumaiti, A. M., & Alameri, W. (2020). A deep learning perspective on predicting permeability in porous media from network modeling to direct simulation. *Computational Geosciences*, *24*(4), 1541-1556. https://doi.org/10.1007/s10596-020-09963-4

Tembely, M., AlSumaiti, A. M., & Alameri, W. S. (2021). Machine and deep learning for estimating the permeability of complex carbonate rock from X-ray micro-computed tomography. *Energy Reports*, *7*, 1460-1472.

Timur, A. (1968). An investigation of permeability, porosity, and residual water saturation relationships. SPWLA 9th annual logging symposium,

Uchic, M. D., Holzer, L., Inkson, B. J., Principe, E. L., & Munroe, P. (2007). Three-Dimensional Microstructural Characterization Using Focused Ion Beam Tomography. *MRS bulletin*,, *32*(5), 408-416.

van der Land, C., Wood, R., Wu, K., van Dijke, M. I. J., Jiang, Z., Corbett, P. W. M., & Couples, G. (2013). Modelling the permeability evolution of carbonate rocks. *Marine and Petroleum Geology*, *48*, 1-7. https://doi.org/https://doi.org/10.1016/j.marpetgeo.2013.07.006

Verdhan, V. (2020). Supervised learning with python. *Apress, Springer, Berkeley, CA*.

Vilcáez, J. (2020). Reactive transport modeling of produced water disposal into dolomite saline aquifers: Controls of barium transport [Article]. *Journal of Contaminant Hydrology*, *233*, Article 103600. https://doi.org/10.1016/j.jconhyd.2020.103600

Vilcáez, J., Morad, S., & Shikazono, N. (2017). Pore-scale simulation of transport properties of carbonate rocks using FIB-SEM 3D microstructure: Implications for field scale solute

transport simulations. *Journal of Natural Gas Science and Engineering*, *42*, 13-22. https://doi.org/10.1016/j.jngse.2017.02.044

Walls, J. D., & Amaefule, J. O. (1985). Capillary Pressure and Permeability Relationships in Tight Gas Sands *SPE/DOE Low Permeability Gas Reservoirs Symposium*. https://doi.org/https://doi.org/10.2118/13879-MS

Wang, F., Yang, K., You, J., & Lei, X. (2019). Analysis of pore size distribution and fractal dimension in tight sandstone with mercury intrusion porosimetry. *Results in Physics*, *13*, 102283.

Wang, G., Chang, X., Yin, W., Li, Y., & Song, T. (2017). Impact of diagenesis on reservoir quality and heterogeneity of the Upper Triassic Chang 8 tight oil sandstones in the Zhenjing area, Ordos Basin, China. *Marine and Petroleum Geology*, *83*, 84-96. https://doi.org/10.1016/j.marpetgeo.2017.03.008

Wang, Y., & Miller, J. D. (2020). Current developments and applications of micro-CT for the 3D analysis of multiphase mineral systems in geometallurgy. *Earth-Science Reviews*, *211*. https://doi.org/10.1016/j.earscirev.2020.103406

Warren, J. G., & Price, H. S. (1961). Flow in Heterogeneous Porous Media [Article]. *Soc Petrol Eng J*, *1*(03), 153-169. https://www.scopus.com/inward/record.uri?eid=2-s2.0-84944861054&partnerID=40&md5=bb20d7224345cb1ee528ff9a2db6530f

Wells, J., & Amaefule, J. (1985). Capillary pressure and permeability relationships in tight gas sands. SPE/DOE Low Permeability Gas Reservoirs Symposium,

Westphal, H., Surholt, I., Kiesl, C., Thern, H. F., & Kruspe, T. (2005). NMR Measurements in Carbonate Rocks: Problems and an Approach to a Solution. *pure and applied geophysics PAGEOPH*, *162*(3), 549-570. https://doi.org/10.1007/s00024-004-2621-3

Whitten, E. H. T. (1977). Stochastic Models in Geology. *The Journal of Geology*, *85*(3), 321-330. https://doi.org/10.1086/628302

Willson, C. S., Lu, N., & Likos, W. J. (2012). Quantification of Grain, Pore, and Fluid Microstructure of Unsaturated Sand from X-Ray Computed Tomography Images. *Geotechnical Testing Journal*, *35*(6). https://doi.org/10.1520/gtj20120075

Wu, J., Yin, X., & Xiao, H. (2018). Seeing permeability from images: fast prediction with convolutional neural networks. *Science bulletin*, *63*(18), 1215-1222.

Wu, T., Li, X., Zhao, J., & Zhang, D. (2017). Multiscale pore structure and its effect on gas transport in organic-rich shale [Article]. *Water Resources Research*, *53*(7), 5438-5450. https://doi.org/10.1002/2017WR020780

Wu, Y., Lin, C., Ren, L., Yan, W., An, S., Chen, B., Wang, Y., Zhang, X., You, C., & Zhang, Y. (2018). Reconstruction of 3D porous media using multiple-point statistics based on a 3D training image. *Journal of Natural Gas Science and Engineering*, *51*, 129-140. https://doi.org/10.1016/j.jngse.2017.12.032

Xiong, Q., Baychev, T. G., & Jivkov, A. P. (2016). Review of pore network modelling of porous media: Experimental characterisations, network constructions and applications to reactive transport. *J Contam Hydrol*, *192*, 101-117. https://doi.org/10.1016/j.jconhyd.2016.07.002

Xu, T., Sonnenthal, E., Spycher, N., & Pruess, K. (2006). TOUGHREACT—a simulation program for non-isothermal multiphase reactive geochemical transport in variably saturated geologic media: applications to geothermal injectivity and CO2 geological sequestration. *Computers & Geosciences*, *32*(2), 145-165.

Yang, L., Ai, L., Xue, K., Ling, Z., & Li, Y. (2018). Analyzing the effects of inhomogeneity on the permeability of porous media containing methane hydrates through pore network models combined with CT observation. *Energy*, *163*, 27-37.

Yang, X., Mehmani, Y., Perkins, W. A., Pasquali, A., Schönherr, M., Kim, K., Perego, M., Parks, M. L., Trask, N., Balhoff, M. T., Richmond, M. C., Geier, M., Krafczyk, M., Luo, L.-S., Tartakovsky, A. M., & Scheibe, T. D. (2016). Intercomparison of 3D pore-scale

flow and solute transport simulation methods. *Advances in Water Resources*, *95*, 176-189. https://doi.org/10.1016/j.advwatres.2015.09.015

Yang, X., Scheibe, T. D., Richmond, M. C., Perkins, W. A., Vogt, S. J., Codd, S. L., Seymour, J. D., & McKinley, M. I. (2013). Direct numerical simulation of pore-scale flow in a bead pack: Comparison with magnetic resonance imaging observations. *Advances in Water Resources*, *54*, 228-241. https://doi.org/10.1016/j.advwatres.2013.01.009

Yang, Y., & Aplin, A. C. (2010). A permeability–porosity relationship for mudstones. *Marine and Petroleum Geology*, *27*(8), 1692-1697. https://doi.org/10.1016/j.marpetgeo.2009.07.001

Yao, Y., & Liu, D. (2012). Comparison of low-field NMR and mercury intrusion porosimetry in characterizing pore size distributions of coals. *Fuel*, *95*, 152-158.

Zhang, H., Yu, H., Yuan, X., Xu, H., Micheal, M., Zhang, J., Shu, H., Wang, G., & Wu, H. (2022). Permeability prediction of low-resolution porous media images using autoencoder-based convolutional neural network. *Journal of Petroleum Science and Engineering*, *208*. https://doi.org/10.1016/j.petrol.2021.109589

Zhang, K., Wang, S., Wang, L., Cheng, Y., Li, W., Han, X., Liu, C., & Su, H. (2022). 3D visualization of tectonic coal microstructure and quantitative characterization on topological connectivity of pore-fracture networks by Micro-CT. *Journal of Petroleum Science and Engineering*, *208*. https://doi.org/10.1016/j.petrol.2021.109675

Zhang, L. (2013). Aspects of rock permeability. *Frontiers of Structural and Civil Engineering*, *7*(2), 102-116. https://doi.org/10.1007/s11709-013-0201-2

Zhang, P., Lee, Y. I., & Zhang, J. (2019). A review of high-resolution X-ray computed tomography applied to petroleum geology and a case study. *Micron*, *124*, 102702. https://doi.org/10.1016/j.micron.2019.102702

Zhang, S., Lu, P., Cantrell, D., Zaretskiy, Y., Jobe, D., & Agar, S. M. (2017). Improved quantification of the porosity–permeability relationship of limestones using petrographical texture. *Petroleum Geoscience*, *24*(4), 440-448. https://doi.org/10.1144/petgeo2017-052

Zhang, Z., & Cai, Z. (2021). Permeability Prediction of Carbonate Rocks Based on Digital Image Analysis and Rock Typing Using Random Forest Algorithm. *Energy & Fuels*, *35*(14), 11271-11284. https://doi.org/10.1021/acs.energyfuels.1c01331

Zhao, J., Sun, M., Pan, Z., Liu, B., Ostadhassan, M., & Hu, Q. (2022). Effects of pore connectivity and water saturation on matrix permeability of deep gas shale. *Advances in Geo-Energy Research*, *6*(1), 54-68. https://doi.org/10.46690/ager.2022.01.05

Zheng, H., Yang, F., Guo, Q., Pan, S., Jiang, S., & Wang, H. (2022). Multi-scale pore structure, pore network and pore connectivity of tight shale oil reservoir from Triassic Yanchang Formation, Ordos Basin. *Journal of Petroleum Science and Engineering*, *212*, 110283. https://doi.org/https://doi.org/10.1016/j.petrol.2022.110283

VITA

Olubukola Adedotun Ishola

Candidate for the Degree of

Doctor of Philosophy

Dissertation: A NEW STOCHASTIC PORE-SCALE SIMULATION AND MACHINE LEARNING APPROACH TO PREDICTING PERMEABILITY AND TORTUOSITY OF HETEROGENEOUS POROUS MEDIA

Major Field: Geology

Biographical:

Education:

Completed the requirements for the Doctor of Philosophy in Geology at Oklahoma State University, Stillwater, Oklahoma in May 2023.

Completed the requirements for the Master of Science in Petroleum Geosciences at University College Dublin, Dublin, Republic of Ireland in 2018.

Completed the requirements for the Bachelor of Science (Honours) in Geophysics Adekunle Ajasin University, Ondo, Nigeria in 2013.

Experience:

Graduate Research and Teaching Associate, Oklahoma State University, Stillwater, OK (08/2019 - 05/2023).
Earth AI Resident, X, the moonshot factory [Google X], Mountain view, CA (06/2022 - 08/2022).
Graduate Intern, Oak Ridge National Laboratory (ORNL), Oak Ridge, TN (06/2021 - 08/2021).

Professional Memberships:

American Association of Petroleum Geologists, American Geophysical Union, Geological Society of America, National Association of Black Geoscientists, Society of Petroleum Engineers, Society of Exploration Geophysicists, Society of Petrophysicists and Well Log Analysts, European Association of Geoscientists and Engineers.